UNIVERSIDADE DE LISBOA
FACULDADE DE CIÊNCIAS
DEPARTAMENTO DE ENGENHARIA GEOGRÁFICA, GEOFÍSICA E ENERGIA

Novel separators and electrodes for the Li-S system

Paulo Filipe Serobaba Soares Luís

Mestrado Integrado em Engenharia da Energia e do Ambiente

Dissertação orientada por:
Professor Doutor Killian Lobato (FCUL)
Doutor Engenheiro Markus Hagen (Fraunhofer ICT)

2017

Abstract

As one of the prospective energy storage systems, rechargeable lithium-sulfur (Li-S) batteries offer possibilities of low-cost and high energy density since sulfur offers a high theoretical capacity of 1675 mAh g^{-1} and a high specific energy of 2600 Wh kg^{-1}. However, commercialization of the current liquid type Li-S batteries is still hindered by insufficient cycle life with rapid capacity fades and low practical energy densities. Much work has been reported to address the aforementioned obstacles, but to gear the Li-S battery research towards practical applications, new approaches should be adopted.

In this dissertation, binder-free ultra-thin carbon films were deposited on a standard separator, exploiting a variant of the Langmuir-Blodgett technique (LB), termed as Langmuir-Blodgett Scooping (LBS). The developed methodology was obtained through adjustment of the parameters that compromised the stability and homogeneity of the film upon the formation at the air-water interface and further transfer to the substrate. Subsequently, the functionalized separators comprised of 1, 5 and 10 layers of Ketjenblack (KB), Super C (SC) and multiwalled carbon nanotubes (MWCNT), were systematically studied for their ability to improve cycling behavior, polysulfide retention and reduction potential in Li-S cells. As result, cells based on carbon coated separators yield superior capacity and retention rates, compared with pristine separator. Nevertheless, carbon-coatings of MWCNT, followed by SC, evidenced higher active material utilizations, while cells employing separators coated with KB showed no improvements. Further galvanostatic studies were conducted on cells employing carbon-coated separators of MWCNT, but in the absence of the additive lithium nitrate ($LiNO_3$), in order to investigate the trapping of soluble polysulfides. From the results, it was demonstrated that even with the best-performing carbon coating, the polysulfide shuttling was not inhibited. However, a retention of capacity was observed on following cycles, evidencing that lithium polysulfides could be trapped on the carbon film and remained electrochemically accessible. To prove this statement, additional SEM investigations were performed on cycled anodes retrieved from cells employing carbon-coated separators of MWCNT. The SEM examinations showed pronounced surface deterioration. However, unaffected areas were also detected, demonstrating that certain zones of the carbon film efficiently blocked the polysulfides.

Additionally, solvent-free lithium sulfide (Li_2S) cathodes were produced through a heat-press technique. The cathodes formulations comprised pristine and core-shelled Li_2S, KB, and as binders polyvinylpyrrolidone (PVP) and polyethylene oxide (PEO). Regarding the manufacturing method, and the cathode compositions adopted, it was found that the core-shell structure greatly enhanced the mechanical integrity of the cathodes, serving as an interparticle binding agent. Moreover, enhancements on the rate capabilities and cycling performances of cathodes employing core-shelled Li_2S particles was observed. On the other hand, cathodes containing pristine Li_2S particles demonstrated poor structural integrity, which resulted in major losses of material. Furthermore, lower discharge capacities were reported from cells employing cathodes with pristine Li_2S particles.

Keywords: Li-S battery, binder-free ultra-thin carbon coatings, solvent-free Li_2S cathodes.

Resumo

Como um dos potenciais sistemas de armazenamento de energia, as baterias de lítio-enxofre (Li-S) apresentam baixo custo e elevada densidade energética, dado que o enxofre possui uma elevada capacidade e densidade energética teóricas, 1675 mAh g^{-1} e 2600 Wh kg^{-1}, respetivamente. No entanto, a comercialização de baterias de Li-S, que utilizam eletrólitos líquidos, encontra-se paralisada devido ao curto tempo de vida das baterias, perda rápida de capacidade e baixas densidades energéticas praticáveis. Esforços têm sido realizados por parte da comunidade científica para resolver os obstáculos anteriormente mencionados, no entanto para alcançar níveis de utilização praticáveis, novas abordagens devem ser adotadas.

Nesta dissertação foi utilizada uma variante da técnica de Langmuir-Blodgett (LB), denominada como Langmuir-Blodgett *Scooping* (LBS), para revestir separadores com filmes de carbono ultrafinos. A metodologia desenvolvida foi obtida através do ajuste dos parâmetros que comprometeram a estabilidade e homogeneidade do filme durante o processo de formação na interface ar-água, e posterior transferência para o substrato. Posteriormente, os separadores revestidos com 1, 5 e 10 camadas de Ketjenblack (KB), Super C (SC) e nanotubos de carbono com paredes múltiplas, foram analisados pela sua habilidade em melhorar a ciclicidade, a retenção de polisulfetos de lítio e no potencial de redução em células de Li-S. Como resultado, células com separadores revestidos com carbono apresentaram capacidades e taxas de retenção de capacidade superiores, em comparação com células sem estes componentes. No entanto, células que apresentaram separadores revestidos com MWCNT, seguidos por SC, evidenciaram maior utilização de material ativo, enquanto que células com separadores revestidos com KB não demonstraram quaisquer melhorias. Estudos adicionais foram realizados a células com separadores revestidos com MWCNT, mas na ausência do aditivo nitrato de lítio ($LiNO_3$), a fim de investigar o efeito de retenção de polisulfetos de lítio. A partir dos resultados observou-se que o revestimento que apresentou o melhor desempenho não permitiu a inibição do fluxo de polisulfetos de lítio entre os elétrodos. No entanto, foi observada uma retenção de capacidade, demonstrando que uma parte dos polisulfetos de lítio ficaram retidos no revestimento de carbono e encontravam-se electroquimicamente acessíveis. Para provar esta afirmação, investigações adicionais foram realizadas em ânodos de lítio provenientes de células com separadores revestidos com MWCNT, através de microscopia eletrónica de varrimento (MEV), anteriormente submetidos a ciclos de descarregamento e carregamento. As imagens mostraram uma certa degradação na superfície do ânodo de lítio, no entanto certas zonas não apresentaram qualquer deterioração, demonstrando que partes do revestimento de carbono bloquearam eficientemente os polisulfetos de lítio.

Cátodos de sulfeto de lítio (Li_2S) foram produzidos na ausência de solvente, utilizando prensagem térmica. Os cátodos apresentavam na sua constituição partículas de Li_2S e partículas de Li_2S em estrutura núcleo-concha, KB, e como aglutinantes polivinilpirrolidona (PVP) e óxido de polietileno (PEO). Quanto ao método de produção, e às composições adotadas para os cátodos, verificou-se que a estrutura núcleo-concha promoveu uma maior integridade mecânica do cátodo, desempenhando o papel de agente ligante entre os vários componentes. Além disso, observou-se melhoria no desempenho de células com cátodos de Li_2S em estrutura núcleo-concha na sua composição. Por outro lado, cátodos com partículas de Li_2S demonstraram pouca integridade estrutural, o que resultou em grandes perdas de material. Adicionalmente, foram obtidas capacidades de descarregamento inferiores em células que utilizaram estes cátodos.

Palavras-chave: Baterias de Li-S, revestimentos de carbono ultrafino, cátodos de Li_2S.

Table of Contents

List of Figures

List of Tables

Acknowlegdments

First and foremost, I would like to express my sincere gratitude to Faculdade de Ciências da Universidade de Lisboa and Frauhofer Institute of Chemical Technology, for providing the means and opportunity to exert this dissertation.

I would like to express my deep gratitude to Dr. –Ing. Markus Hagen. His support and instructions throughout the research, and readiness to give his time so generously which has been very much appreciated. Moreover, I would also like to express my very great appreciation to Prof. Dr. Killian Lobato, for his valuable and constructive suggestions during the writing of the dissertation.

I am also grateful for M. Sc. Philipp Schüdel and Dr. Katharina Ahlbrecht, for their ideas, suggestions and instructions.

I would also like to extend my thanks to the laboratory technicians of the Fraunhofer ICT Applied Electrochemistry Department: Hubert Weyrauch and Ramona Speck for their support with the SEM investigations and confocal microscopy, Dominik Müller and Patrick Fanz for their instructions to operate the syringe pump and the PEEK foil welding machine, respectively.

I would also like to thank Oliver Witzgall for providing water-based Li-S cathodes, used in galvanostatic cycling investigations.

I would like to acknowledge the support provided by my family through all these years, in special to my parents, brother and grandparents.

Last but not least, I thank my friends.

List of Symbols

γ	Surface tension (mN m^{-1})
Δt	Discharge/charge period (h)
η_{CE}	Coulombic efficiency
Π	Surface pressure (mN m^{-1})
C	C-rate (h^{-1})
i	Current imposed (mA)
m	Mass of sulfur/Li_2S (g)
Q_H	Upper plateau discharge capacity (mAh g^{-1})
$Q_{H,contribution}$	Upper plateau contribution (%)
Q_L	Lower plateau discharge capacity (mAh g^{-1})
$Q_{L,contribution}$	Lower plateau contribution (%)
Q_{th}	Theoretical capacity (mAh)
$Q_{th,m}$	Theoretical specific capacity (mAh g^{-1})
$Q_{th,m\ sulfur}$	Theoretical specific capacity of sulfur (mAh g^{-1})
Q_{tot}	Specific discharge/charge capacity (mAh g^{-1})
$S\%$	Sulfur utilization (%)
V	Voltage (V)

List of Chemical Formulas

H_2S	Hydrogen sulfide
Li^+	Lithium-ion
Li_2CO_2	Lithium carbonite
Li_2O	Lithium oxide
Li_2S	Lithium sulfide
Li_2S_2	Lithium dissulfide
Li_2S_n	Lithium polysulfides
$LiBF_4$	Lithium tetrafluoroborate
LiOH	Lithium hydroxide
$LiPF_6$	Lithium hexafluorophosphate
Li_xNO_y	Lithium nitrates
Li_xSO_y	Lithium sulfates
S_8	Sulfur

List of Abbreviations

BSE	Backscattered electrons
CMC	Carboxymethyl cellulose
CNF	Carbon nanofibers
CNT	Carbon nanotubes
DME	1,2-Dimethoxyethane
DOL	1,3-Dioxolane
EDS	Energy dispersive X-ray spectroscopy
KB	Ketjenblack
LB	Langmuir-Blodgett
Li-S	Lithium-Sulfur
LiTF	Lithium trifluoromethanesulfonate
LiTFSI	Lithium-bistrifluoromethanesulfonamide
MWCNT	Multi-walled carbon nanotubes
PEEK	Polyether ether ketone
PEO	Poly(ethylene oxide)
PVDF	Polyvinylidene difluoride
PVP	Poly(vinylpyrrolidone)
SBR	Styrene butadiene rubber
SC	Super C65
SEI	Solid Electrolyte Interface
SEM	Scanning Electron Microscopy

Chapter 1 – Introduction

This chapter intends to set the theme and objectives that the dissertation aims to achieve. Firstly, the context in which the theme is inserted will be presented and described. Finally, the structure of the dissertation will be presented.

1.1. Contextualization

The access of energy at reasonable cost without damaging the environment is one of the major challenges of this century. The growing consumption of fossil fuels, and their limited availability, along with the environmental impacts, has stimulated the development of alternative, sustainable and clean energy technologies. Renewable energy sources such as solar, wind and tidal are attractive in this scope, but the effective utilization of these non-controllable energy sources requires efficient and economical reliable electrical energy storage (EES) systems [1]. Rechargeable batteries have been widely used in stationary and mobile applications, and among the different rechargeable battery systems, Li-ion batteries offer the highest energy density among the other systems. However, even when fully developed, the highest energy storage that Li-ion can deliver is too low to meet the demands of key markets, such as transportation and smart grids [2], hence, appealing the investigation of new chemistries and materials.

1.2. Scope and objectives

As a candidate for next generation of EES, the veteran system lithium-sulfur (Li-S), first proposed in the '60s [3], has once again received much attention due to its high theoretical specific energy, 2500 Wh kg^{-1}, equivalent to 2800 Wh l^{-1}. Sulfur has a high theoretical specific capacity of 1675 mAh g^{-1} (*vs* Li/Li^+), is abundant in nature, extremely cheap and environmental friendly [4, 5]. Figure 1 shows a comparison between the different EES technologies commercially available today, where it is clearly shown that the existent Li-S technology already surpasses the majority of EES technologies, in terms of energy stored per unit volume or weight. Moreover, it is expected that this technology will achieve energy densities comparable to Li-ion, and specific energies 2-4 times higher. For this reason, is considered as a great candidate as future energy storage technology.

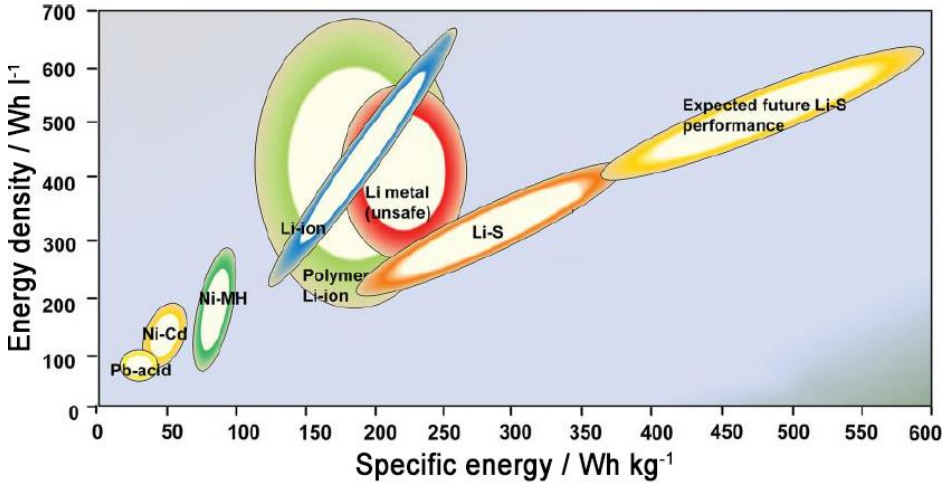

Figure 1 – Comparison of energy density and specific energy of current SEE technologies. Pb-acid stands for lead-acid, Ni-Cd for nickel-cadmium and Ni-MH for nickel-metal hydride. Figure adapted from Hagen *et al.* [6].

Despite the considerable advantages offered by Li-S storage technology, commercial development of a practical Li-S rechargeable battery has been limited due to its inherent problems, including the

insulating nature of sulfur, large volume expansion and its soluble intermediates, which leads to a low utilization of active material, poor coulombic efficiency and great degradation of capacity after a few cycles. Some of the troublesome issues aforementioned can be solved by innovative Li-S battery configurations, through the synergetic introduction of novel cathode structures, binders, functionalized separators, novel electrolytes and anodes.

Functionalized separators aim to stabilize Li-S electrochemistry by shielding the diffusion of soluble intermediates through the cell, reactivate sulfur-containing species and inhibit the dendritic growth in the lithium metal surface. Carbons, polymers, and oxides have been coated on separators to enhance the batteries performance [7]. Several groups investigated the improvements on Li-S by coating carbons on the separator, achieving excellent cycling performances [8, 9, 10, 11, 12, 13]. Since carbon coatings add passive weight to the cell, they should be thin and low weight. To overcome this issue, alternative coating methods are required. Langmuir-Blodgett method allows one to produce thin ordered films by repeated transfer of a molecular-size layer, preformed on a water surface, onto a solid substrate. This technique has been widely used in numerous fields of science and technology due to its ability to precisely control the thickness of coatings, for the versatility of substrates that can be coated, and for its scalability. In this dissertation an alternative coating method using Langmuir-Blodgett approach, by applying multiple thin carbon layers on commercial polypropylene separator will be investigated. Additionally, several studies were conducted to determine the improvements on Li-S cells employing different carbon coatings with different thicknesses.

Lithium sulfide (Li_2S), the end discharge product of Li-S batteries, has a theoretical specific capacity of 1166 mAh g^{-1}, and it is more desirable as the cathode material than sulfur because it allows the use of lithium-free anodes, such as silicon, tin, or metal oxides. However, Li_2S presents technical challenges: low electronic and ionic conductivities, difficult activation of Li_2S, and sensitivity to moisture and oxygen [14]. To overcome the first two issues, similar approaches applied on sulfur should be used, such as mixing Li_2S with conductive carbon additives and binders. A typical approach to activate Li_2S particles is based on increasing the higher cut-off voltage in the first charge cycle. However this could result in the electrolyte depletion and decline of the cell lifetime [15]. Several studies will be shown on this dissertation regarding different Li_2S cathode compositions, to understand which improvements could be adopted to enhance the electrochemical performance.

1.3. Structure of the document

A brief introduction about battery fundamentals is provided in the beginning of Chapter 2 followed by an overview of Li rechargeable battery technologies. Subsequently, the reaction mechanism of Li-S technology and its inherent issues are presented. Still in Chapter 2, a description of the main components of a Li-S cell is given. The description of the experimental work, as well as the results and discussion are presented in Chapter 3 and Chapter 4, respectively. In Chapter 3 are defined the followed experimental protocols, in regards to the production of binder-free ultra-thin carbon-coated separators and solvent-free Li_2S cathodes. Furthermore, the composition of the electrolytes and characterization techniques, used through the course of the thesis, are presented. Chapter 4 covers the discussion and interpretation of the obtained results. The chapter starts with a detailed description of the various steps required to achieve the method adopted to coat the separators, followed by the discussion of the electrochemical performance of Li-S cells with the produced carbon-coated separators. Afterwards, is discussed the shuttle effect's inhibition of Li-S cells with functionalized separators, followed by *ex-situ* imaging analysis of the cell components. Last but not least, the cycling performance of Li_2S cathodes are presented and discussed. To conclude, the summary of this thesis with the conclusions and suggestions for future work are described in Chapter 5.

Chapter 2 – Theory and Background

This section starts with a brief explanation of battery fundamentals, followed by currently used battery chemistries, focusing in Li systems. Furthermore, the reaction mechanism of Li-S batteries, the current technical challenges associated with the electrochemistry and solutions for the different issues, will be presented. Moreover, it will be explained the process responsible for the formation of Langmuir-Blodgett films.

2.1. Batteries

A battery consists of several rechargeable cells which can be coupled in series and/or parallel, depending on the voltage and capacity required. A cell is the basic electrochemical unit that converts the chemical energy contained in its active materials directly into electric energy by means of an electrochemical oxidation-reduction reaction. The energy is stored in the materials used within the battery. The main components of a cell consist of two electrodes, the anode and cathode, each attached to its specific current collector, physically isolated by a separator to prevent internal short-circuiting, immersed in an electrolyte solution, containing dissociated salts, which enables ion transfer between the two electrodes. In Figure 2 is schematized the different components of a cell. If the electrodes are connected via an external circuit, the chemical reactions take place at both electrodes, thereby delivering electrons and enabling the current to be utilized. Upon discharge, electrons are released at the anode from the electrochemically active material, which is oxidized. At the same time, the cathode is reduced by receiving electrons. During charging, an externally applied electrical energy forces a reversal of the electrochemical process; as a consequence, the reactants are restored to their original form, and the stored electrochemical energy can be used once again. The electrical energy that can be supplied by a battery, is referred either per unit of weight (Wh kg^{-1}) or per unit of volume (Wh l^{-1}) of the battery, termed as specific energy or energy density, respectively. These parameters are a function of the cell voltage (V) and the capacity (Ah kg^{-1}), which are dependent on the cell chemistry [16, 17].

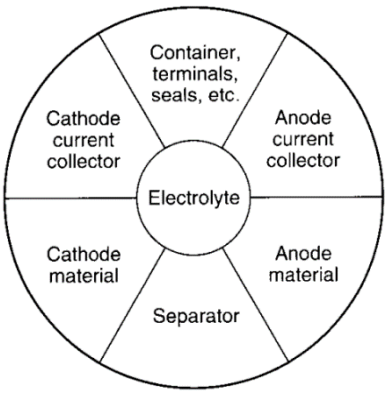

Figure 2 – Components of a cell [17].

2.1.1. Cell components

Anode and cathode

The anode, or negative electrode, gives up electrons to the external circuit and is oxidized during the electrochemical reaction. On the other hand, the cathode, or positive electrode, accepts electrons from the external circuit and is reduced during the electrochemical reaction. In practice, the anode is selected regarding its efficiency as a reducing agent, high specific capacity, good conductivity, stability, easy of fabrication, and low cost. As for the cathode, it must be an efficient oxidizing agent, stable upon contact with the electrolyte, and have a useful working voltage. A highly desirable

combination of anode and cathodes materials are those that would minimize the weight and give a high cell voltage and capacity [17].

Electrolyte

The electrolyte provides the medium for transfer of charge inside the cell between the anode and cathode. Regarding the nature of the electrode couple, an appropriate selection of compatible electrolytes is vital to maximize the electrochemical performance. Typically used electrolytes can be aqueous, nonaqueous, ionic liquids, solid polymer and ceramic/glassy, with dissolved salts, acids, or alkalis to impart ionic conductivity. The criteria to choose a proper electrolyte are its chemical stability upon contact with battery components, electrochemical stability for the applied potential range, proper activity in a wide range of temperatures, moderate viscosity, high ionic conductivity, non-toxic and inexpensive [18].

Separator

The separator, the distance-keeping component between the electrodes, does not participate directly in the electrochemical process of electric energy storage, being considered as a passive component of the electrochemical cell. Its main function is to prevent electrical short circuits between the electrodes, while allowing efficient transport of ionic charge carriers. Other factors must be considered when selecting the best separator for a particular battery chemistry, such as the mechanical stability, chemical resistance to degradation by electrolyte, impurities, electrode reactants and products [19, 20].

2.1.2. Basic concepts of electrochemistry

Capacity

The capacity is the measure of the removable charge from a cell or a battery. The capacity is strongly dependent on the temperature and the discharge current, but above all, on the active material used and its loading on the electrode. The theoretical capacity, in mAh, is calculated as follows:

$$Q_{th} = \frac{m_A}{M_A} \cdot n_e \cdot F \tag{1}$$

where m_A is the mass of active material, M_A is the molar mass of the active material, n_e is the quantity of electrons released, and F is the Faraday constant.

Another important characteristic in battery technology is the specific capacity, in mAh g^{-1}, which is related to the mass of active material.

$$Q_{th,m} = \frac{n_e \cdot F}{M_A} \tag{2}$$

The C-rate is particularly important when specifying charging and discharging currents. It represents the amount of charge or discharge current, in amperes, as a multiple of the rated capacity in ampere-hours. As example, considering a fully charged battery with a capacity of 5 Ah, and discharging at 0.5 A, the battery is discharged at the 0.2C or C/5 rate, thus operating for 5 hours. The C-rate is expressed as

$$C = \frac{i}{Q_{th} \cdot m_A} \tag{3}$$

where i is the induced current, and Q_{th} the theoretical capacity of the battery, and m_A is the mass of active material.

The coulombic efficiency η_{CE} sets the amount of charge consumed $Q_{discharge}$ in relation to the stored charge Q_{charge} and is calculated according to the equation.

$$\eta_{CE} = \frac{Q_{discharge}}{Q_{charge}} \cdot 100\% \quad (4)$$

It measures the reversibility of the electrochemical, translated by side reactions occurring in the cell [21].

Losses

Electrochemical devices convert chemical energy into electrical energy by redox reactions. However, losses due to polarization occur when a current passes through the electrodes, accompanying the electrochemical reactions. These losses include the activation polarization, concentration polarization and ohmic polarization. The activation polarization is the energy consumed to drive the electrochemical reaction at the electrode surface. The concentration polarization arises from the concentration differences of the reactants and the products at the electrode surface and in the bulk, as result of mass transfer. The ohmic polarization, also mentioned as IR drop, results from the internal impedance of the cell. This type of loss causes a voltage drop during operation, and consumes part of the useful energy as waste heat. Since the voltage drop is proportional to the current drawn from the system, it strongly affects the rate capability [22].

2.2. Lithium-metal batteries

The motivation for using metallic lithium as anode relies on the fact this element is the most electropositive (-3.04 V *vs.* H/H^+), as well as the lightest metal, thus facilitating the design of storage systems with high energy density. Owing to its high specific capacity (3860 mAh g^{-1}), this technology rapidly found applications as power sources. However, the system was not viable. It soon encountered the short-coming of Li-metal/non-aqueous electrolyte combination – uneven growth of dendrites and mossy structures [23], due to heterogeneous lithium deposition and dissolution during charge and discharge of the lithium metal anode. Additionally, due to the low potential, the electrolytes used are thermodynamically not stable against lithium. Their reductive decomposition and the parallel corrosion of the Li electrode lead to the formation of a solid electrolyte interphase (SEI). On one hand, the formation consumes the anode and electrolyte, leading to low efficiencies. On the other hand, the SEI prevents the physical contact between the Li anode and the electrolyte. However, the continuous growth of lithium-related structures leads to the formation of new SEI, thus consuming more electrolyte [24]. Below are schematized the stages that encompass the interfacial reactions at the lithium surface.

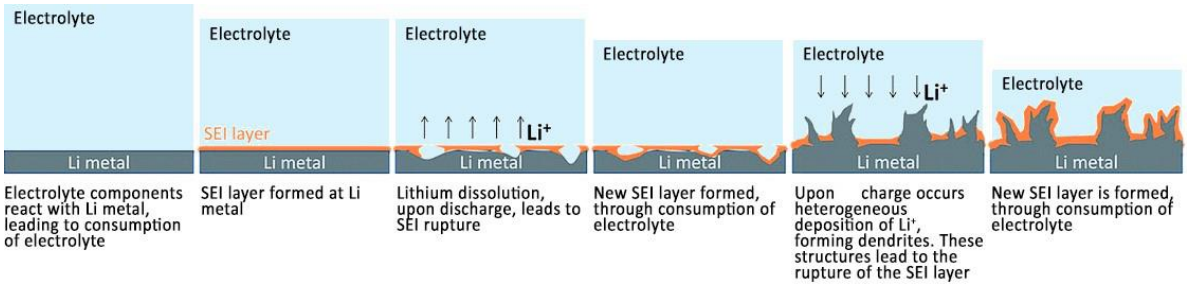

Figure 3 – Reaction mechanism of SEI and lithium dendrites at lithium interphase. Figure adapted from Peng *et al.* [25].

Such structures can be seen in the SEM micrographs in Figure 4. Prior to cycling, the metallic lithium anode shows no deformities, however, after the 1st cycle, needle-like structures of lithium, known as dendrites, were promptly formed. At the 14th cycle, mossy structures of lithium build up. These structures lead to disconnection and electrical isolation of active material, resulting in loss of capacity and dangerous electrical shorting between the electrodes, causing explosion hazards [23]. Thus, to minimize detrimental reactions associated with the electrode-electrolyte interface, several alternative approaches were pursued in which either the electrolyte or the negative electrode was modified [26].

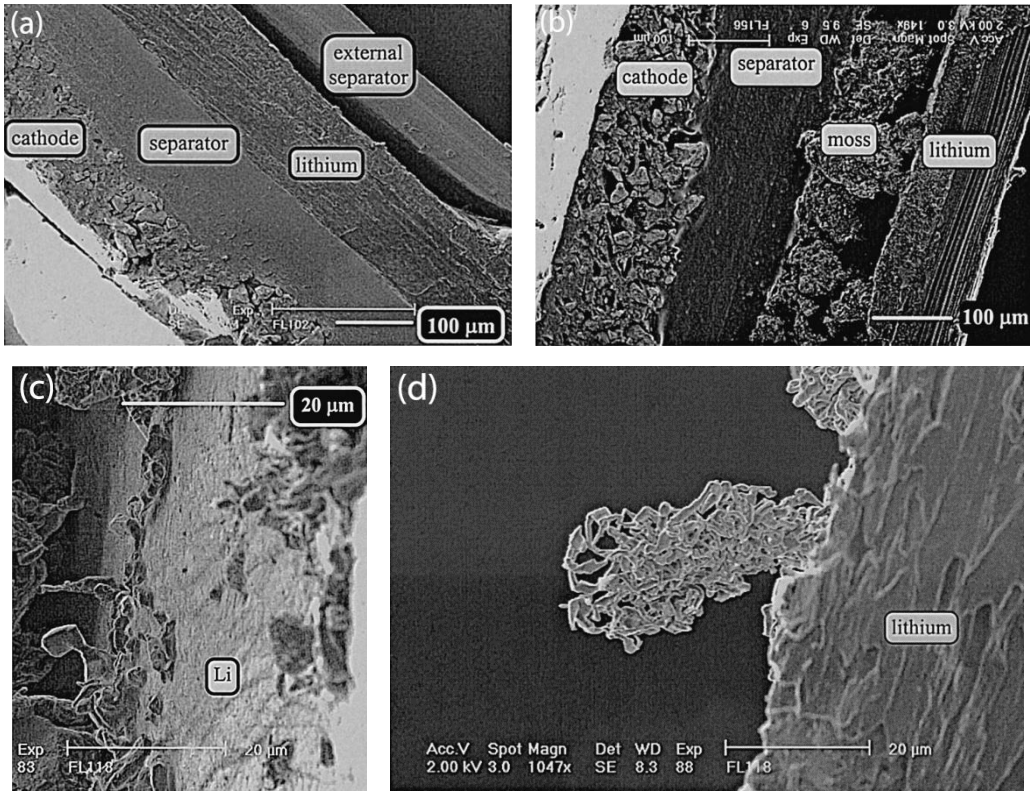

Figure 4 – SEM micrographs of cross-sectioned lithium cell (a) Before cycling, (b) After 14th charge, (c) Surface of the Li-anode after one charge, (d) Dendrite formed after one charge. Figure adapted from Orsini *et al.* [27].

2.3. Lithium-ion batteries

Attempts to develop rechargeable battery technologies based in lithium came with appealing changes on the very structure of the electrodes. The first approach involved the substitution of metallic lithium with carbon negative electrodes. By inserting lithium ions (Li^+) into the carbon matrix, the formation of dendrites was strongly mitigated. As outcomes, the cell would achieve high cyclability, and risks of explosion greatly inhibited. The second approach involved the introduction of intercalation cathode compounds, such as layered-type transition-metal oxides (Li_xMO_2, M=Co, Ni, Mn). In this process, Li^+ are reversibly removed or inserted into a host, a process also referred as "Rocking-chair" [23]. The electrochemical process in a Li-ion cell is illustrated in Figure 5.

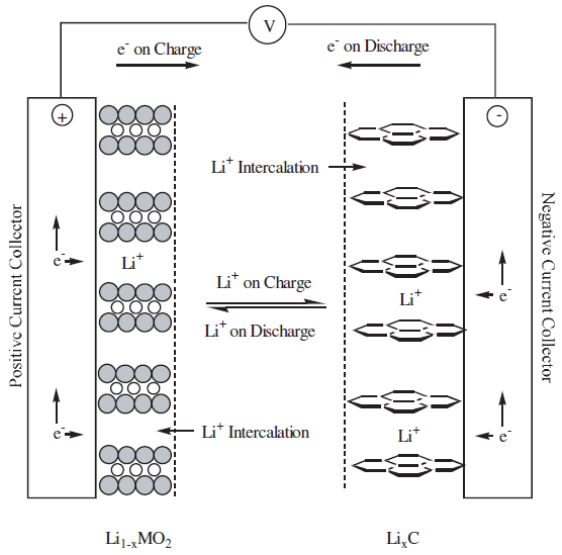

Figure 5 - Schematic of the electrochemical process in a Li-ion cell [28].

The combination of these two approaches resulted in the formulation of the notorious lithium-ion technology. In addition to layered-type transition-metal oxides, other materials can also be utilized, such as spinel oxides, olivine structures, and silicates [29]. First commercialized by Sony in 1991, this technology has rapidly become the standard power source in a broad array of markets, and increasingly diverse range of applications. Compared to other rechargeable technologies, the high specific energy and energy density made them attractive. Moreover, they offer a low self-discharge rate, long cycle life, and broad temperature range of operation [28]. However, despite the advantages brought by this technology, even when fully developed, the highest energy storage that Li-ion battery systems can deliver is too low to satisfy the demands of new key markets, such as transportation and grid applications [2]. The reasons facing the further development of this technology account with the low energy density of the available cathode materials [30], loss of reversible capacity, safety issues, which decrease the reliability of these systems, and limited availability of cathode active materials, which causes it to have a high price. Li-ion batteries often suffer from deterioration in their microstructure due to volume expansion or contraction, and morphology changes of the cathode during intercalation/de-intercalation, worsening at high current densities, and depth of discharge [31, 32, 33]. In addition, thermal runaway, caused by exothermic reactions between the electrodes and electrolyte, result in irreversible increase of temperature, leading to safety issues [34].

2.4. Lithium-Sulfur Batteries

The growing demand of novel electrochemistries triggered the research of new systems, which include the Li-S batteries. The electrochemical redox reactions of Li-S are based on the interaction of sulfur with lithium to form lithium sulfide (Li_2S), as final product of the discharge reaction[1]. The overall reaction is given by

$$S_8 + 16Li \rightleftharpoons 8Li_2S \tag{5}$$

A typical voltage profile of Li-S is plotted in Figure 6.

[1] Li-S system operates by electrochemical conversion of sulfur through a multi-step redox and disproportionation reactions through the recombination of lithium polysulfides. Several authors proposed mechanistic understandings for Li-S electrochemistry in agreement with experimental analytical studies and physical models [117], although a simplistic model will be presented in this thesis which is acknowledged in several articles and is in accordance with the scientific aspects of this work.

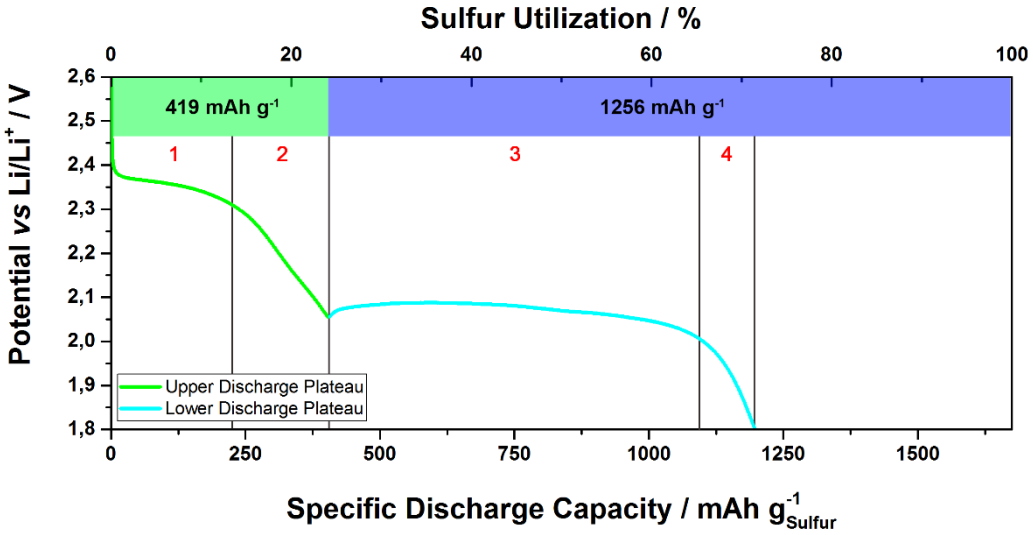

Figure 6 – Typical discharge profile of Li-S cell showing an upper (green) and lower (blue) plateau, with corresponding theoretical specific discharge capacities of each plateau on top.

Since elemental sulfur lies in a charged state, the cathodic reaction takes place, and can be divided in four phases [35, 36]:

Phase 1: Lithium metal gets oxidized forming Li^+, which migrate to the cathode and react with sulfur. Sulfur is reduced and forms soluble high-order polysulfides, Li_2S_8. This stage corresponds to a solid-liquid reduction. This reaction occurs at the upper voltage plateau and ranges between 2.4 and 2.3 V.

$$S_8 + 2Li^+ + 2e^- \rightarrow 2Li_2S_8 \quad (6)$$

Phase 2: As discharge continues, the dissolved Li_2S_8 are reduced to polysulfides of lower orders (with a $4 \leq n < 7$ in Li_2S_n). This stage, along with the previous, corresponds to the first discharge plateau, with a theoretical capacity of 419 mAh g^{-1}, represented in Figure 6, in green. At the end of the first discharge region, the solutions viscosity reaches its maximum.

$$Li_2S_8 + 2Li^+ + 2e^- \rightarrow Li_2S_{8-n} + Li_2S_n \quad (7)$$

Phase 3: Soluble polysulfides are reduced into insoluble lithium polysulfides, lithium disulfide (Li_2S_2) and Li_2S. This stage, known as the lower voltage plateau, contributes to the major capacity of the Li-S battery, and ranges between 2.1-2.0 V.

$$2Li_2S_n + (2n-4)Li^+ + (2n-4)e^- \rightarrow nLi_2S_2 \quad (8)$$

$$Li_2S_n + (2n-2)Li^+ + (2n-2)e^- \rightarrow nLi_2S \quad (9)$$

Phase 4: The final discharging step relates to a solid-solid reduction from the insoluble species Li_2S_2 to Li_2S. Due to the low solubility and slow kinetics of Li_2S_2 in the electrolyte, the full reduction to Li_2S may not be complete, as shown in Figure 6. This stage, along with the previous, corresponds to the second discharge plateau, with a theoretical capacity of 1256 mAh g^{-1}.

$$Li_2S_2 + 2Li^+ + 2e^- \rightarrow 2Li_2S \quad (10)$$

Even though Li-S shows extraordinary high theoretical capacity values, current practical values are 65% lower [4]. Several problems associated with the decline of capacity and coulombic efficiency will be further discussed.

2.4.1. Technical Challenges

Li-S battery uses liquid electrolytes that have a high solubility for polysulfides to maximize the sulfur utilization, thus improving the rate capability [37]. However, due to the solubility of the polysulfides in organic solvents, a concentration gradient between the anode and cathode is generated, resulting in the diffusion and loss of soluble active material through the separator to the anode and concurrently side reactions take place simultaneously. The soluble species may react with the lithium anode and form insoluble Li_2S_2 and Li_2S, as shown in Eq. 11 and Eq. 12, which easily precipitate onto the lithium anode surface [38].

$$2Li + Li_2S_n \rightarrow Li_2S + Li_2S_{n-1} \quad (11)$$

$$2Li + Li_2S_n \rightarrow Li_2S_2 + Li_2S_{n-2} \quad (12)$$

Moreover, these nonconductive species can continue to react with the soluble species deposited on the anode's surface and form more low-order polysulfides, as shown in Eq. 13 and Eq. 14.

$$Li_2S + Li_2S_n \rightarrow Li_2S_m + Li_2S_{n-m+1} \quad (13)$$

$$Li_2S + Li_2S_n \rightarrow Li_2S_m + Li_2S_{n-m+2} \quad (14)$$

When the Li anode side becomes concentrated with low-order polysulfides, they diffuse back to the cathode and are re-oxidized to higher-order polysulfides. The polysulfide shuttle causes self-discharge and produces current, which does not contribute to charging of the battery. If prior to cycling preventive measures are not taken, such as limiting the charging time, the recharging period could be infinite, and intensifies at low charging current densities [39, 40, 41]. Such corrosion reactions cause the loss of active material, leads to low coulombic efficiencies and rapid capacity fading. These chemical reactions always exist in liquid-type Li-S systems, and are particularly severe in the charging upper plateau.

Lithium polysulfides are strong oxidizers and react actively with metallic lithium. As demonstrated in Eq. 11 and Eq. 12, when lithium polysulfides react with the anode, the reduction of polysulfides and the precipitation of Li_2S occurs. Continuous precipitation of electrochemically inactive Li_2S forms a solid passivating film, leading not only to capacity loss but also polarization of the anode and therefore increase of cell resistance. Remarkably, the dissolution of polysulfides and shuttling in the electrolyte provides an intrinsic mechanism for passivating dendrite tips by reaction with the polysulfides in the electrolyte, providing also a high intrinsic overcharge tolerance for Li-S cells [5]. Nevertheless, this should be avoided, since it degrades the electrochemical performance of the cell, as discussed before.

At the end of discharge, Li_2S and Li_2S_2 are formed and are regarded as electric and ionic insulators. At this stage, these species form a thick solid passivating layer on the cathode, predominantly at the surface, which gets thicker at high current densities. This layer decreases the diffusion of Li^+ into the bulk of the cathode, leading to decrease of capacity output. Moreover, with further cycling, accumulation of electrochemical inactive Li_2S/Li_2S_2 on the surface of the cathode was reported, and is considered as irreversible loss of active material and electrochemical surface [42, 43, 44, 45].

Another challenge concerns the severe self-discharge rates in Li-S batteries. Since the dissolution of polysulfides is inevitable, the high-order polysulfides and sulfur slowly dissolve in the electrolyte, even in resting state, reacting with the Li anode, as described in Eq. 11 and Eq. 12. With longer storage periods, a decrease of capacity followed with an increase of overpotential was reported [46].

A further issue is associated with the volumetric variation during cycling. Due to the difference of specific densities of elemental sulfur and Li_2S, 2.03 g cm^{-3} and 1.67 g cm^{-3}, respectively, the cathode experiences a volume expansion of 80%. Volume contraction and expansion can result in mechanical failure of the cathode, which deteriorates the reversibility of the cell. Moreover, volume expansion

upon Li^+ uptake, makes Li_2S pulverize and lose their electrical contact with the conductive substrate or the current collector.

Much work has been reported to address the aforementioned obstacles, but to gear the Li-S battery research towards practical applications, new approaches should be adopted to integrate with the currently developed systems. It has been demonstrated that the cycling properties of sulfur can be significantly improved by introducing sulfur into nanostructured carbon matrixes [47], performing modifications at the separators surface [7], and applying novel electrolytes [48].

2.4.2. Cathodes

Sulfur is regarded as an insulating material (5×10^{-30} S cm^{-1} at 25°C). For this reason, mixing sulfur with conductive additives is required. Moreover, the high solubility of lithium polysulfides in liquid electrolytes, and the volume variation upon cycling, are issues that need to be mitigated. In this regard employing porous carbon-composites with binders showed to be an effective way to improve the cathodes performance [49].

Active material

During the conceiving of a Li-S battery, there are some approaches to build the battery in respect to the desired charged state. A charged or discharged cell can be produced depending on whether sulfur or lithium sulfide (Li_2S) are used as active material, respectively.

Lithium sulfide, a lithiated counterpart of sulfur, has recently received attention in view of its compatibility with safer high-capacity metallic lithium-free anodes, such as silicon [50], silicon oxide composites [51], tin [52] and graphite [53], preventing safety concerns and low coulombic efficiency of lithium metal in Li-S batteries [54, 55]. Moreover, since it lies in discharge state, the risk of self-discharge during storage is excluded. Furthermore, compared with easily sublimating sulfur, Li_2S has a much higher melting point of 938 ºC and is in the maximum volume state, providing the possibility of high-temperature modification of Li_2S materials and ensuring a more stable structure [56]. Given the high theoretical capacity, 1166 mAh g^{-1}, and comparatively low price, Li_2S represents quite a promising candidate for use as cathode material in high-energy rechargeable systems.

Even thought, some challenges remain. Similar to sulfur, Li_2S suffers from low electronic and ionic conductivity [57] and upon cycling, serious dissolution of lithium polysulfides is observed into the electrolyte, which results in loss of active material, thus poor cycling performance. Therefore, to improve its utilization, it requires an intimate contact with carbon additives. Moreover, Li_2S has a large initial potential barrier inherent to its intrinsic characteristics: slow transfer kinetics described by phase nucleation of Li_2S into polysulfides during the first charge [58], and presence of insulating oxidized surface structures, such as Li_2SO_x, Li_2CO_2 and Li_2O [59]. To overcome the potential barrier, the cutoff voltage should be set higher than the potential barrier during the first charge, up to 4.0 V *vs* Li/Li^+. However, by setting a higher voltage, currently employed electrolyte solutions in Li-S batteries are known to deteriorate. In this regard, several strategies were proposed to overcome this issue, such as adding redox mediators to the standard electrolyte solution [15], and controlling the surface characteristics of the Li_2S nanoparticles [59], which allowed to recover most of the theoretical capacity in the activation cycle at lower potentials. Another approach to minimize the drawbacks from the potential barrier is based on the introduction of polysulfides in the electrolyte, which act as charge transfer mediators [58, 60]. Another hindrance from using Li_2S is its reaction with air moisture, which leads to the formation of LiOH and H_2S gas release. Therefore, the electrode preparation must be performed under inert atmosphere.

Carbon additives

To increase the conductivity of the electrodes, two strategies have been widely adopted – doping and coating of conductive phases to improve the intrinsic conductivity of the active material, and the

incorporation of conductive additives into the electrodes to form conductive networks around the active material. Among a variety of carbonaceous materials, porous carbons are highly desired due to their high electrical conductivities and morphological characteristics. Porous carbon materials possess unique characteristics according to their pore size and morphology. Micropore carbons, with a pore size inferior to 2 nm, have been demonstrated an ideal container for confining the polysulfides, due to strong adsorption of these species by the narrow micropores. Mesopore carbons, with pore sizes in the range of 2-50 nm, can enhance sulfur encapsulation as the designed pore is small, promote lithium-ion transport at the cathode region because they offer abundant channels for the electrolyte, as well as raise the tolerance toward high sulfur loading and volume variation as the pore size and volume is large. Macropore carbons, with pore sizes higher than 50 nm, are able to ensure excellent electrolyte immersion and suppress polysulfide migration due to its high electrolyte absorbability [61]. Via delicate synthesis procedures, engineered hierarchical porous carbons [62, 63], hollow carbon spheres [64], coalescent carbon nanotubes (CNT) or carbon nanofibers (CNF) networks decorated with various porous carbons [65] were produced to improve the stability, capacity and conductivity of the active material.

Binder

Among the components in a sulfur cathode, the binder plays an important role in improving the cell performance, especially in regards to cycle life. Mechanical modification of the composite electrode due to volume changes during cycling, results into structural modifications of the cathode. In this regard, binders are employed to maintain the integrity and stability of the cathodes structure. A binder should have high adhesion between the electrode materials and the current collector. Furthermore, it should form a good electric network between the active material and conductive carbon, to facilitate the electron transport as well as the diffusion of the Li^+ [66]. Moreover, regarding the binder utilized, each should possess strong affinities to the species encountered in the cathode. Sulfur forms covalent bonds and is non-polar, whereas Li_2S shows ionic bonds and is polar. Due to these differences, some binders may be suitable for sulfur cathodes but not for Li_2S cathodes. According to Seh *et al.*, binders rich in carbonyl and halogen groups are desired in Li_2S cathodes since they show strong binding interactions with Li_2S [67].

Sulfur cathodes with polyvinylpyrrolidone (PVP) as binder showed high initial capacities and high capacity retentions after long term cycling. These results are due to the high number of carbonyl groups characteristic of this binder, which effectively retain soluble polysulfides. Moreover, after cycling at various current densities, high capacity retentions were obtained, indicating high robustness and stability of the cathode composite [67]. Sulfur cathodes with polyethylene oxide (PEO) demonstrated to suppress the deposition of Li_2S on the surface of the cathode. In contact with ether-based electroytes, typically used in Li-S systems, PEO and related polymers tend to swell or dissolve, modifying the solvent system at the cathodes surface. This interphase has shown to improve the solubility of polysulfides near the cathodes surface, delaying the precipitation of the insoluble discharge products, thus suppressing the formation of Li_2S agglomerates at the surface, affording an improvement in specific capacity [68]. Other binders have been proposed in the literature, such as polyvinylidene difluoride (PVDF) [69], carboxymethyl cellulose (CMC), styrene butadiene rubber (SBR) [68] and polytetrafluoroethylene (PTFE) [69], although Li_2S cathodes employing PVP and PEO will be investigated in this thesis

2.4.3. Electrolytes

Requirements for the electrolytes in Li-S systems include high ionic conductivity, optimally targeted at achieving superior Li^+ conductivities over the temperature range of operation, low electronic conductivity, moderate polysulfide solubility, low viscosity and surface tension, wide electrochemical window and good chemical stability against lithium. However, electrolyte solvents used in Li-ion batteries, such as carbonates and phosphates, cannot satisfy the requirements since they react irreversibly with the polysulfides [70]. The binary solvent mixture of 1,2-dimethoxyethane (DME) and 1,3-dioxolane (DOL) have been considered as the most suitable solvent mixture for Li-

S systems [70]. DME offers high polysulfide solubility and fast reaction kinetics, but is more reactive with Li metal. On the other hand, DOL has slower reaction kinetics, lower polysulfide solubility but forms a stable solid electrolyte interface (SEI) on the lithium metal [71]. The combination of the solvents generates synergetic effects on the capacity retention as compared with the solvent alone [72]. Although these solvents have been widely used in Li-S batteries, safety issues arise for operations at high temperatures due to the low boiling point and flash points [48].

As for the salt, the chemical compatibility with polysulfides is the highest priority. Conventional salts used in Li-ion batteries such as lithium hexafluorophosphate ($LiPF_6$) and lithium tetrafluoroborate ($LiBF_4$), cannot be used in Li-S batteries due to the irreversible reactions with the polysulfides. In addition, these salts cannot be used with DOL due to their Lewis acid property that initiates DOL molecules ring-opening polymerization [38]. So far, lithium trifluoromethanesulfonate (LiTF, $LiSO_3CF_3$) and lithium bistrifluoromethanesulfonamide (LiTFSI, $LiN(SO_2CF_3)_2$), have been considered as the suitable salts for liquid Li-S batteries [73]. However, the later has higher ionic conductivity [74, 75], and when combined with DOL and DME, a relatively stable and flexible SEI is formed on the lithium anode, reducing the shuttle effect.

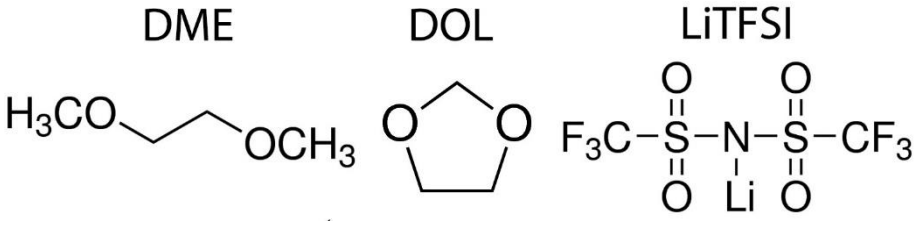

Figure 7 – Structural formulae of the chemical components present in the electrolyte, typically employed in Li-S cells.

Electrolyte additives are also employed in Li-S systems to improve the batteries performance by protecting the lithium anode. Lithium nitrate ($LiNO_3$) has been widely used as an additive in Li-S cells due to its effect on suppressing efficiently the polysulfides shuttle effect. This additive forms a SEI on the lithium surface, which consists of Li_xNO_y and Li_xSO_y species which come from direct reduction of $LiNO_3$, and oxidation of sulfur species by $LiNO_3$, and thus prevents the electron transfer from the lithium anode to polysulfides, ceasing the shuttle effect [37]. However, the beneficial lithium passivation is also accompanied with irreversible reduction of $LiNO_3$ at the carbon surface in the cathode, when discharging to potentials below 1,6 V, affecting the reversibility process of sulfur. Its beneficial effects may also decay during prolonged cycling due to the additive consumption [76].

2.4.4. Separators

Polyethylene and polypropylene separators fulfill the requirements for lithium based nonaqueous batteries – good chemical stability and mechanical strength, highly porous which facilitate ionic charge transfer, submicrometer pore size to prevent dendritic lithium penetration, and low cost. However, these polyolefin separators also have inherent drawbacks, such as insufficient wettability toward the electrolyte, leading to the increase of the batteries polarization and consequent low capacity and rate capability, and poor thermal stability, resulting in potential safety concerns [77, 20, 19]. Nevertheless, these separators provide a margin of protection against thermal runway, caused by the increase of impedance at about 130 °C, close to the melting temperature of the polymer, that effectively ceases the ionic transport between the electrodes. This mechanism results from the pores collapse, turning the separator into a nonporous insulating layer between the electrodes [19].

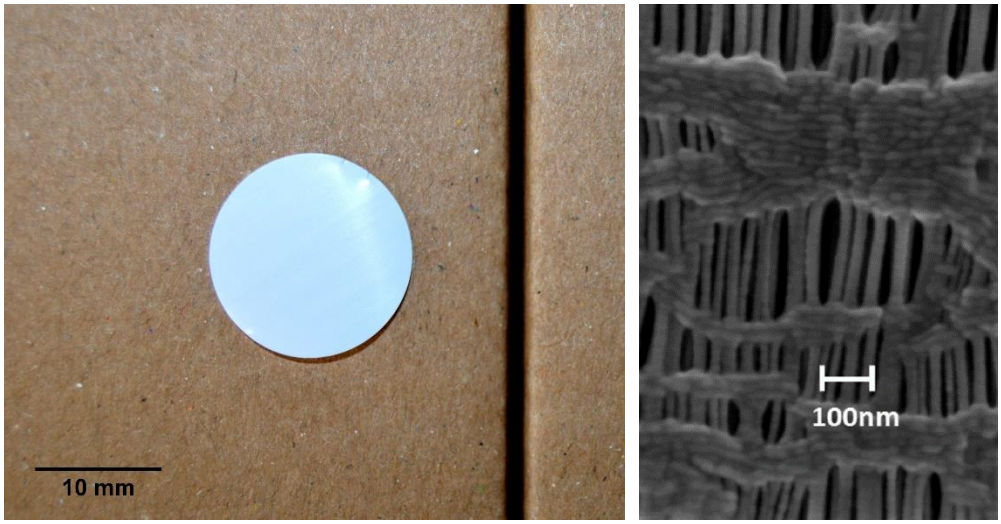

Figure 8 – Top (left) and high magnification (right) images of a polypropylene separator Celgard 2400 [78].

Polyolefin based separators are also widely employed in liquid Li-S batteries. However, the separator is unable to trap the soluble polysulfides due to its pore size, 43 nm [79], which is greater than the polysulfides dimension, 1.0-1.8 nm [8]. Moreover, Yao *et al.* found that the separator is able to accommodate a large amount of polysulfides inside, due to its high porosity, contributing to decrease of active material utilization [80]. Regarding these issues, tailoring the physical and chemical properties of the separator was demonstrated as a viable way to improve the performance of Li-S batteries.

2.4.5. Carbon-coated separators

The separator is one perfect platform for modification that can introduce novel cell configurations for Li-S batteries. Although intensive research in Li-S technology has been focused in the development of electrodes and novel electrolytes, the influence of the separator on the cell performance has rarely been studied.

Before the emergence of functionalized separators, free-standing interlayers were first developed from the necessity to address some of the obstacles inherent to Li-S chemistry – limit the diffusion of polysulfides, reactivate sulfur species at the cathodes surface, and buffer the volume variation. Free-standing carbon interlayers fully exploit the physicochemical attributes of carbonaceous materials - high electrical conductivities, tunable pore structures and surface properties. As a result, the integration of interlayers has been shown to provide Li-S cells with high electrochemical utilizations and excellent cycling stability. It was demonstrated that carbon interlayers function as an upper-current collector, which can improve the electron conduction by its high electric conductivity and fast ion transport through its abundant nanospace. Moreover, its nanospace further plays a significant role as the polysulfide-trapping site, which can suppress the migration of dissolved polysulfides, and the high pore volume serves as a cushion to volume variations between cycles [81].

Su *et al.* reported the fabrication of a multiwalled carbon nanotube (MWCNT) interlayer using a relatively simple procedure, by ultrasonic dispersion of the MWCNT in isopropanol, followed by vacuum filtration without the addition of binders [82]. Afterwards, the interlayer was introduced between the cathode and the separator, and the cells were cycled at C/5. The introduction of the interlayer provided an outstanding first discharge capacity of 1466 mAh g^{-1}, and after 50 cycles the cell reported a reversible capacity of 962 mAh g^{-1}. On the other hand, the same cell, but without the interlayer, showed a lower first discharge capacity of 671 mAh g^{-1}, and after 50 cycles had a reversible capacity of 350 mAh g^{-1}. Regarding these findings, the introduction of the MWCNT interlayer demonstrated an exceptional increase of active material utilization, compared to the cell cycled without the interlayer.

An interlayer of carbonized polyacrilonitrile nanofibers, manufactured through electrospinning, by Singhal *et al*., also demonstrated significant cycling performances [83]. The cell with the interlayer showed an initial capacity of 1519 mAh g^{-1}, and after 100 cycles at C/5, the cell demonstrated a discharge capacity of 1215 mAh g^{-1}, corresponding to a loss of reversible capacity of only 18%. The control cell, without the interlayer component, also reported a high initial capacity, 1226 mAh g^{-1}, although, after 100 cycles a wide decrease of capacity was observed, 200 mAh g^{-1}, corresponding to a loss of 61% of capacity.

As evidenced, the introduction of the interlayer provided enhancements in the cycling performance of Li-S cells. Although great increase of performance was achieved, their weight and thickness turns out to be an issue, which decreases the overall cells specific energy. The weights of the two reported interlayers are 0.8 and 4.48 mg cm^{-2}, and a thickness of 50 and 214 µm.

Attempts to reduce the interlayers weight to minimize the impact in the energy density, lead to a decrease in the mechanical strength and reduced polysulfide-trapping capability [81]. To overcome these problems, the concept of surface-coated separator was developed. While maintaining the electrodes apart and allowing the flow of Li^+, the separator functions as a highly robust substrate to support the coating layer, providing the necessary flexibility and mechanical strength.

A lightweight Super P carbon-coated separator was proposed for Li-S cells, fabricated by slurry-coating on one side of the separator [10]. The casting process only included isopropyl alcohol solvent, and the related fabrication process is facile and adaptable for scaling up. As a result, the carbon loading and thickness obtained were 0.20 mg cm^{-2} and 20 µm, respectively. Cells employing the carbon-coated separator reported a first discharge capacity of 1112 mAh g^{-1}, and at the 50^{th} cycle, the capacity decreased to 810 mAh g^{-1}. The control cell, utilizing a pristine separator, reported an initial capacity of 1015 mAh g^{-1}, and after 50 cycles at C/5, a wide decrease of capacity was evidenced, 500 mAh g^{-1}.

The functionalization of polypropylene separators with Ketjenblack were proposed by Zhao *et al*. [9]. A facile and effective approach to prepare a Ketjenblack-coated layer on the surface of separator was performed via tape-casting of a slurry, which included, in minor proportions, Super P and polyvinylidene fluoride, a binder material. The resulting carbon layer had a loading of 0.18 mg cm^{-2}, and a thickness of 10 µm. Superior cycling performances were demonstrated from cells employing the functionalized separator. The capacities reported by both cells with carbon-coated separator and pristine separator, cycled at C/10, at the first cycle were 1318 and 1100 mAh g^{-1}, respectively. However, a significant decrease was observed for the control cell at the 100^{th} cycle, 435 mAh g^{-1}, while the cell employing the carbon coating was able to sustain a capacity of approximately 815 mAh g^{-1}.

A MWCNT modified separator was also reported by Chung *et al.* [12]. The MWCNT consisted of interconnected bundles of nanotubes deposited as a dense filter on one side of the separator, with a carbon loading of 0.17 mg cm^{-2}. The structure contributed with several enhancements to the Li-S system – efficient blocking of soluble polysulfide species, effective reutilization of the active material, and stabilization of the cathodes surface. As a result, cells employing the functionalized separators, cycled at C/5, reported a high capacity of 1324 mAh g^{-1} in the first cycle, and after 100 cycles the cells reported a capacity of approximately 1000 mAh g^{-1}. The control cell showed a lower first discharge capacity, 794 mAh g^{-1}, and after 100 cycles, the capacity decreased to 118 mAh g^{-1}. These results clearly demonstrate the significant enhancements provided through the integration of carbon-coatings in Li-S batteries.

The decrease of thickness and coating density obtained from using carbon-coated separators instead of interlayers, while maintaining high electrochemical performances, makes the utilization of these components highly desirable in Li-S systems. However, in order to minimize the impact of the carbon's layer weight and thickness on the overall specific energy of the cell, the layer should be as thin and low in weight as possible. In this regard, other coating techniques should be adopted in order to achieve such requirements.

2.5. From Self-Assembly to Langmuir-Blodgett Films

Self-assembly is a powerful tool in modern science. The ability to carefully design building blocks to spontaneously assemble into complex nanostructures supports the developments of a wide range of technologies [84]. Self-assembly is defined as a process in which components spontaneously form aggregates. The interactions are generally weak and non-covalent in a self-assembled system. The self-assembly can be carried out at interfaces, such as liquid-liquid, solid-liquid and liquid-gas, essentially through thermodynamic driving forces inherent to the system [85]. Within the different media, the air-water interface is considered as a platform for the self-assembly which provides the necessary routes for the fabrication of two-dimensional nanostructures [86]. In this sense, nanostructuring nanomaterials at the air-water interface through Langmuir monolayers, following by transfer onto solid substrates forming Langmuir-Blodgett (LB) films, has been effectively used to achieve well-controlled surface morphologies. A LB film is a set of monolayers deposited on a solid substrate, up to a molecular scale. The LB technique is a well-established and sophisticated method to control interfacial molecular orientation and packing. First introduced by Irving Langmuir and applied extensively by Katherine Blodgett [87], the method has found its application in a wide range of fields of science and technology, such as electronics, optics and medicine [88]. The ability to precisely control the thickness of coatings to molecular dimensions, the versatility of substrates that can be coated, and its scalability, have fueled a variety of applications. On the following sections the fundamentals and procedures to produce Langmuir-Blodgett films will be described.

2.5.1. Self-Assembly

Traditionally, self-assembly has been defined as the spontaneous association of building units into defined three-dimensional geometry under a defined condition. Thus, it refers to a thermodynamics process where the molecules and the self-assembled aggregates are in equilibrium. The self-assembly process can encompass a wide range of particles, according to their size or system where it occurs. Self-assembly is the force balance process between three classes of forces: attractive, the driving force, repulsive, the opposition force, and the directional force, which can be considered also as the functional force in the sense it is also responsible for the functionality. When the first two classes of forces interact, the process is random, however, when the third class is involved, the process is directional.

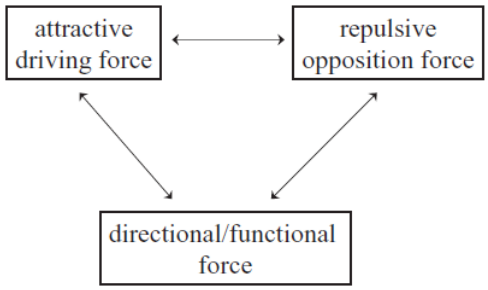

Figure 9 - Self-assembly is defined as the cooperative interaction and balance between three classes of distinctive forces [89].

2.5.2. Langmuir-Blodgett film deposition principles

Langmuir-Blodgett films are obtained through a two-step process: self-assembly on a liquid surface as a Langmuir monolayer by an external mechanic force, and then deposition on solid surfaces by dip-coating (see Figure 10) [90].

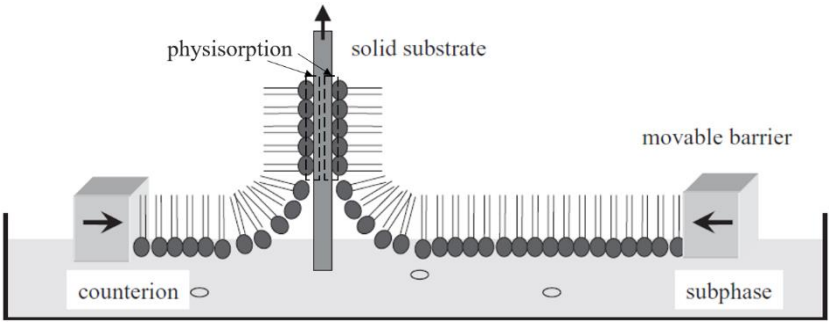

Figure 10 - Schematic representation of the preparation of Langmuir-Blodgett film. Adapted from Yoon [90].

The molecules of most monolayer-forming materials are mainly amphiphiles, although, non-amphiphilic molecules, such as nanoparticles, colloidal particles and polymers, can also form monolayers as well [90]. An amphiphilic molecule has two distinct regions: a hydrophilic, which is easily soluble in water, and hydrophobic, which exerts repulsion with water (see Figure 12) [91]. Moreover, the surface tension exerted from a liquid is important since it will dictate the film forming characteristics. Due to the difference in environment between the surface molecules and those in the bulk, the surface of a liquid always has excess free energy. In a pure liquid, each molecule in the bulk is pulled equally in every direction by neighboring liquid molecules, resulting in a net force of zero. However, the molecules exposed at the surface do not have neighboring molecules in all directions to provide a balanced net force. Instead, they are pulled inward by the neighboring molecules, creating an internal pressure, as illustrated in Figure 11. As a result, the liquid voluntarily contracts its surface area to maintain the lowest surface free energy. This intermolecular force to contract the surface is called the surface tension [92].

Figure 11 - Surface tension on a liquid drop, caused by the unbalanced forces of liquid molecules at the surface [92].

The surface tension γ exerted from a liquid, is defined by the partial differential:

$$\gamma = \left(\frac{\partial G}{\partial A}\right)_{T,P,n} \tag{15}$$

where G is the Gibbs free energy of the system, A is the surface area, and the temperature T, pressure P, and composition n, are held constant [91, 93]. At this point, the monolayer forming mechanism will be described, using stearic acid, an amphiphile, as example. In this technique, a small quantity of the material is dissolved in a volatile organic solvent, and applied dropwise onto the aqueous subphase, spreading on the surface. The spreading will continue until the surface pressure has risen to an equilibrium value. Water is commonly used as the subphase for Langmuir film formation due to its high surface tension, although other solvents can be used. As the solvent evaporates or dissolves into the subphase, a monolayer is formed. Compression of the monolayer, at constant temperature, on the liquid subphase, leads to a reduction of the area (A) available per molecule, thus causing an increase in surface pressure (Π) [91]. By monitoring the monolayer compression, a number of distinct regions are apparent on examining the Π-A isotherm, which are called phases, and are identified by discontinuities in the isotherm. Through the surface pressure isotherm, given by the relationship:

$$\Pi = \gamma_0 - \gamma \tag{16}$$

where γ_0 is the surface tension of the liquid subphase, and γ is the surface tension of the film-covered surface, one is able to identify the molecular packing within the monolayer, the monolayer stability, the occurrence of phase transitions, and the compressibility of the different phases [86, 93, 91]. In Figure 12 is schematized a stearic acid molecule, and a Π-A isotherm of stearic acid monolayer formed at the water surface, with the several phases.

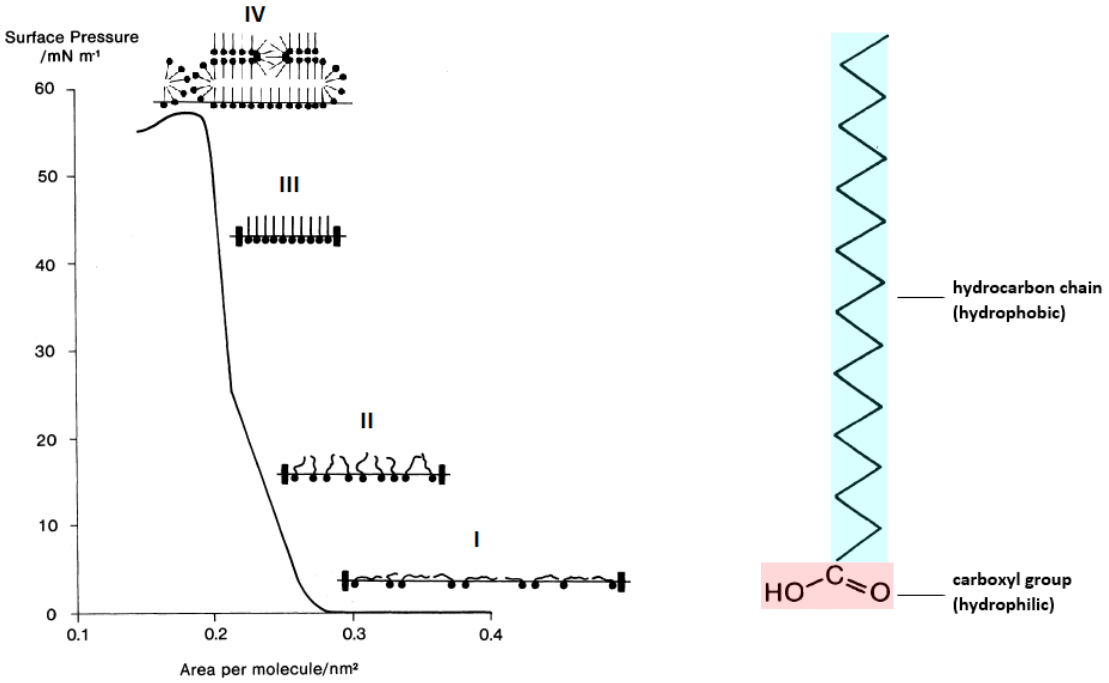

Figure 12 - Surface pressure/area isotherm of stearic acid on an water subphase with the phase sequence; (I) molecules are far apart and do not exert any force on each other – gaseous phase; (II) upon compression, the molecules condense to a low density liquid state – liquid expanded phase; (III) on further compression, the molecules exhibit a defined orientational and positional order – solid phase. Additional pressure results in the (IV) collapse of the monolayer, indicated by a decrease in surface pressure. At this phase, the collapse is dictated by the disordered multilayer formation and the overlapping of monolayers. Figure adapted from Hann [91].

When the targeted surface tension is achieved, a non-reactive substrate is immersed and emersed through the interface, transferring the monolayer, as illustrated in Figure 13. At this stage, a constant surface pressure is maintained by lowering the surface area at a constant rate, to preserve the molecular packing. After the desired number of coatings is achieved, the dip-coating process ends.

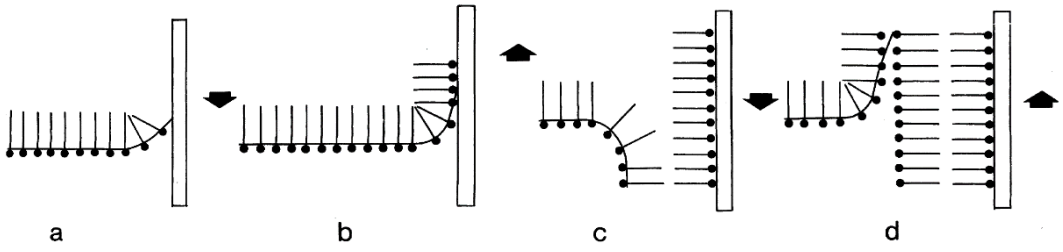

Figure 13 – Deposition of multilayers by Langmuir-Blodgett technique: (a) first immersion, (b) first withdrawal, (c) second immersion, (d) second withdrawal [91].

2.5.3. Experimental techniques

Meticulous attention to experimental detail is required for all monolayer and LB film work. When depositing monomolecular layers in the fashion described above, one of the primary experimental constrains has to be that of cleanliness. Considering that in most monolayer-forming experiments the quantity of material that is used is in the μg range, is then obvious that low levels of dust, residual impurities in the volatile solute, and impurities in the water or on the substrate could readily contaminate the monolayer to a high level. Therefore, a frequent cleaning procedure for all equipment, particularly before a new monolayer material is of the utmost importance. In this regard, freshly double-distilled water should be used [94]. The requirements of a containment for film deposition are relatively straightforward: the material should be inert, it should be hydrophobic to enable easy cleaning, and it should withstand organic solvents as well as inorganic acids. Commonly containment materials are Teflon-made [86] but glass or quartz can also be used [94]. Another important experimental variable is the film transfer speed at which the substrate is moved through the monolayer/air interface. At high dipping speeds the adhesion between the substrate and the monolayer may be insufficient for the monolayer to be attached. Therefore, it is necessary to investigate the optimal speed of transfer prior to successive deposition. The characteristics of the spreading solvent are also important. The necessary properties for such a solvent are the dissolution ability of the monolayer material, nonpolar nature, chemical stability and fast evaporation. Solvents which are commonly used for monolayer spreading include n-hexane, benzene, chloroform and ethyl ether. Regarding the substrate used in a LB experiment, it should be hydrophilic to ensure the proper force setting for the adhesion of the monolayer. Although, if a hydrophobic substrate is being coated, and if the monolayer materials shows poor adhesion to the substrate, then the monolayer will peel off the slide and respread on the water surface. In these cases the solid substrate should be hydrophobitized to ensure a proper interaction with the monolayer [90].

Chapter 3 – Experimental Procedure

The following sections describe the experimental protocols and measurement techniques adopted.

3.1. Binder-free ultra-thin carbon coatings on separator by alternative Langmuir-Blodgett approach

Several suspensions of carbons were produced, with a carbon content in the range of 0.1-0.35% wt., in pure ethanol (Chemsolute®, 99.9%), as shown in Table 1:

Table 1 – Carbon content in the suspensions

Carbon	wt. %
Ketjenblack EC-600 JD (Akzonobel)	0.1
Super C65 (Imerys Graphite & Carbon)	0.35
Nanocyl NC 7000 (Nanocyl)	0.1

The suspension was immersed in an ultrasonic bath (Bandelin Sonorex) for 15 minutes, 35 KHz, at approximately 0 °C, to maximize the dispersion of the particles. After sonication, high shear force was applied to disintegrate existent clusters, using an Ultra-Turrax (T 10 basic Ultra-Turrax), at a speed of 3×10^4 rpm, for 30 seconds (Figure 14).

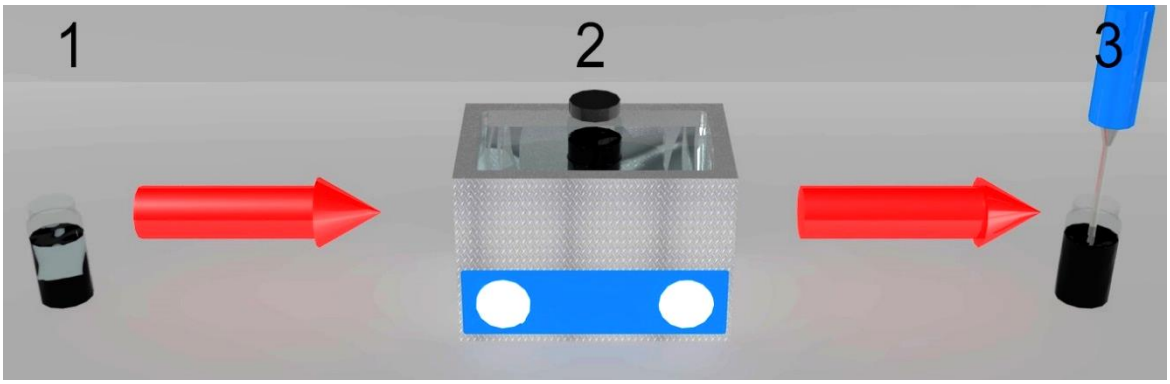

Figure 14 – (1) Preparation of the carbon nanoparticle suspension, starting with the mixing of the carbon nanoparticles with the spreading solvent, then the (2) dispersion of the particles by ultrasonication and finally, (3) dissaglomeration of clusters through high-shear mixing.

The used substrate was a commercial polypropylene Celgard 2400 separator, cut to a piece of 5.0×7.5 cm^2. The separator was placed in a glass plate and the ends taped with Kapton tape to fix it. The substrate was washed with deionized water to flush impurities from the surface. Then isopropanol was rinsed on the separator to wet uniformly, and once again washed with deionized water to take the excess of isopropanol. Finally, the substrate was immersed in a glass container with ultra-pure deionized water (5.5 μS m^{-1}). The injection of the suspension on the water's surface was performed with a syringe pump (Duratec, Nano Pump-Mini), with a pre-defined flow rate of 1000 μl min^{-1}. When the water surface was saturated with the nanomaterial, the substrate was subsequently raised up to transfer the film. Then, the coated substrate was dried on a hot plate, for 1 minute at 70 °C. This process was repeated until the desirable number of carbon layers was achieved (Figure 15).

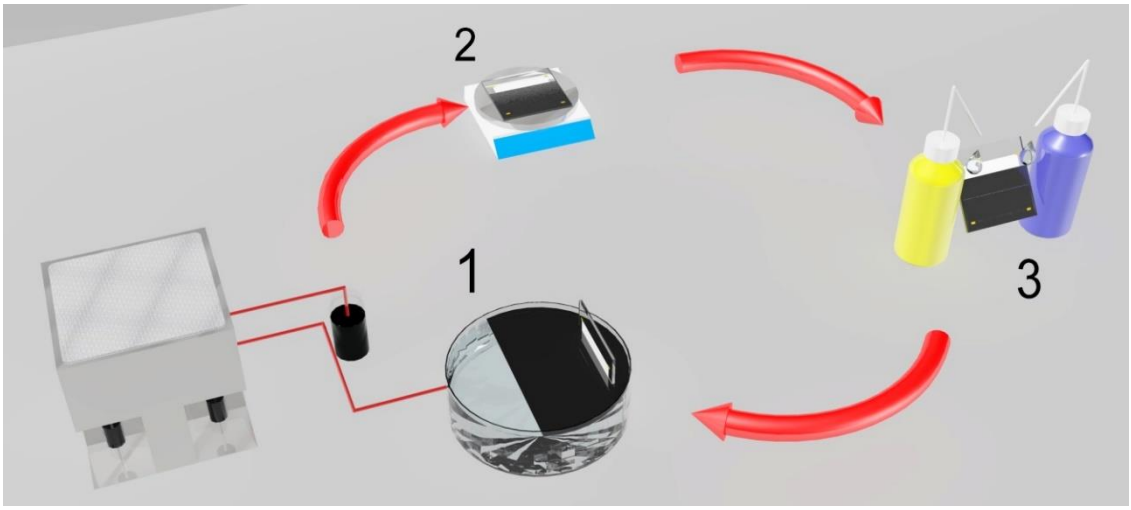

Figure 15 – Layer-by-layer carbon coating process: (1) LB film assembling, (2) drying step and (3) wetting of carbon-coated separator.

To analyze the effects of the carbon coatings on the electrochemical performance, a standard water-based sulfur cathode was used [95]. The composition of the cathode is shown in Table 2.

Table 2 – Composition of the standard water-based sulfur cathode

	wt. %
Sulfur (Sigma Aldrich)	60
Ketjenblack EC-600 JD (Akzonobel)	10
Porocarb HD3 (Hereaus)	10
Porocarb HG3 (Hereaus)	10
PSBR100 Binder (Targray)	10

The cathodes used in the cells had a thickness in the range of 138-159 μm and an average sulfur loading of 4.25 mg cm^{-2}.

3.2. Preparation of solvent-free Li_2S cathodes

The cathodes were produced following a heat-pressing process reported in [96, 97]. This process includes two steps: mixing of Li_2S/carbon/binder composites and hot-pressing.

Several mixtures, containing Li_2S, KB and binder, were ground with a mortar and pestle for 10 minutes, inside an argon filled glove box (MBraun) with monitored moisture level of < 0.1 ppm, and oxygen value of < 0.1 ppm. Two different Li_2S powders were used, carbon-coated (Chemetall Gmbh) and pristine (Albermale, 99.9%), Ketjenblack EC-600JD (Akzonobel) was used as the carbon additive, and two different binders, PVP (Sigma-Aldrich) and PEO (Sigma-Aldrich), with different weight percentages. In total 4 mixtures were created, as followed in Table 3.

Table 3 – Composition of different mixtures used in the production of Li_2S cathodes.

Mixture	Pristine Li_2S / %	Ketjen black / %	PVP / %	PEO / %
1	60	30	10	-
2	60	30	-	10

Mixture	Carbon-coated Li_2S / %	Ketjen black / %	PVP / %	PEO / %
3	60	30	10	-
4	60	30	-	10

After preparing the cathode composite, 150 mg of the powder were smoothly distributed on top of a layer of heat-resistant polymer, previously placed inside a stainless steel template. Afterwards, a layer of carbon-coated aluminum, with the carbon-coated side facing the cathode powder, was placed on top. Since Li_2S is water-, oxygen-sensitive, the template had to be sealed in a PEEK-foil pocket, to cease any contact with the outside environment. Then the template was heat-pressed for 15 minutes, at a temperature and pressure of 155 °C and 2 kbar, respectively. Then, the template was transported inside the argon filled box to retrieve and store the fresh cathode.

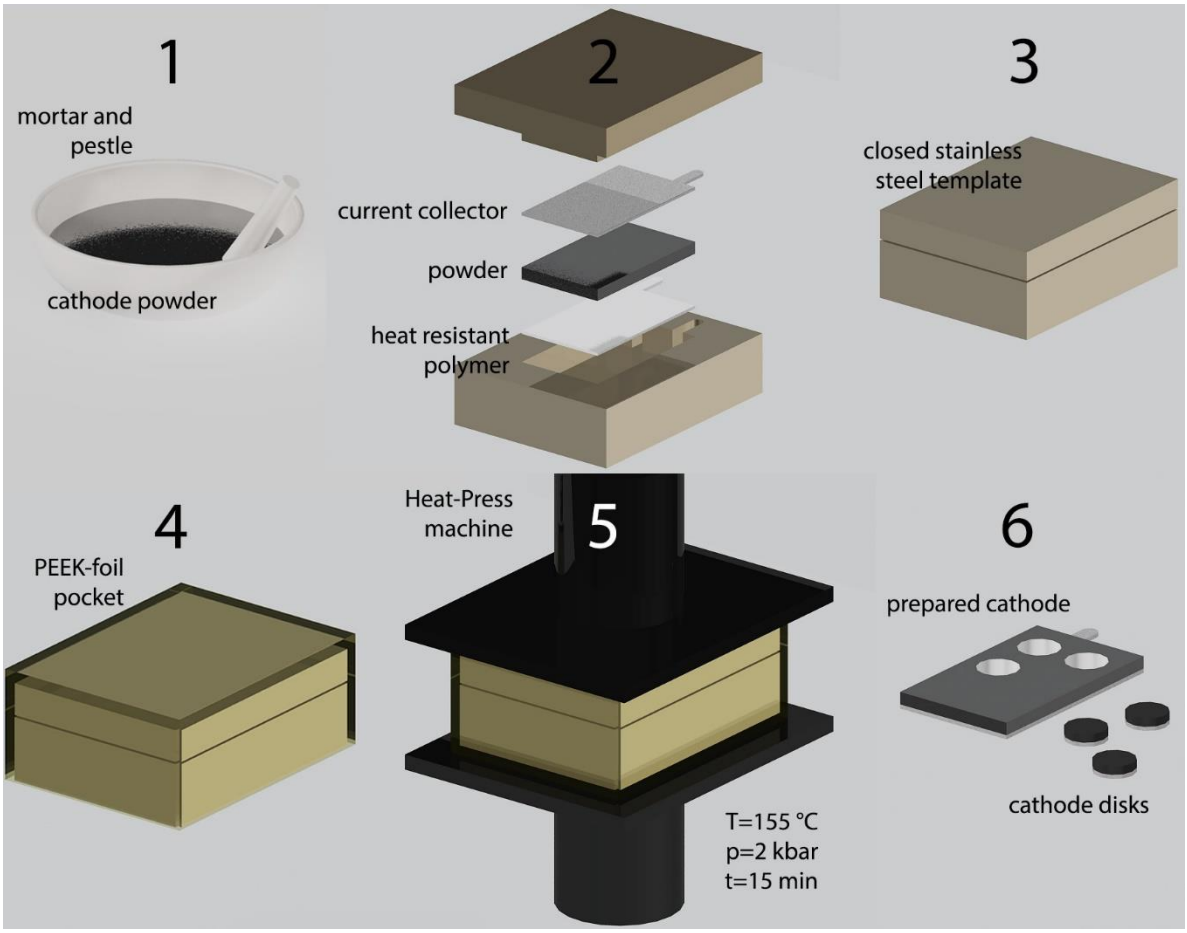

Figure 16 – Solvent-free Li_2S cathodes procedure: (1) powder mixing and grounding with a mortar and pestle; (2) cathode assembly; (3) closed template; (4) template sealed in a PEEL-foil pocket; (5) Heat-pressing of the template; (6) retrieve and puching of the cathode.

3.3. Electrolyte

Two electrolytes were used in the studies. E1, which contains 0,7 M LiTFSI and 0,25 M $LiNO_3$ salts in 1,2-dimethoxyethane (DME) and 1,3-dioxolane (DOL) (2:1 volume ratio). E2 has the same composition as E1, except no $LiNO_3$ salt was employed. The first electrolyte was used in all the studies, while E2 was employed in cells with carbon coatings to investigate their effectiveness in trapping the polysulfides.

3.4. Standard cell

Electrochemical cycling data from the different studies was obtained by assembling cells, in an argon filled glove box (< 0.1 ppm H_2O, < 0.1 ppm O_2). The arrangement of the cell is shown in Figure 17.

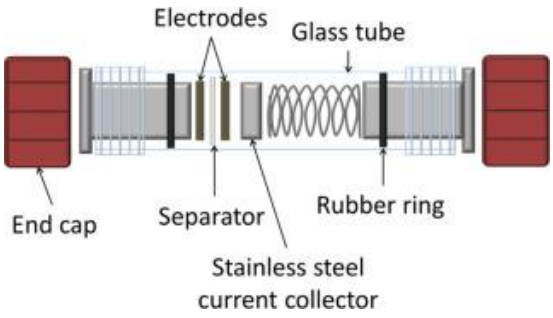

Figure 17 – Standard battery cell [98].

First, a lithium circular disk with 10 mm diameter was pressed into a stainless steel disc and placed on top of the rubber ring end of a steel end plug. Two separators (Celgard 2400), or one separator and one carbon coated separator facing the cathode, with 16 mm diameter each, were placed on top of the anode and then a glass tube was inserted. The plugged end of the glass tube was then closed with an end cap and 40 µl of electrolyte was pipetted onto the separators in the glass tube. A cathode, with 10 mm diameter, was inserted face down onto the separator and an additional stainless steel disc was placed on top of the cathode followed by a steel spring. Finally, the top end of the glass tube was plugged and capped off.

3.5. Galvanostatic cycling

3.5.1. Fundamentals

In a Li-S system, the contribution of the discharge capacities of the two main plateaus, and their decrease with cycling under certain experimental conditions, provides information about the reaction mechanism taking place. Through galvanostatic voltammetry, also known as cyclic chronopotentiometry, it is possible to quantify and identify the various plateaus and their capacity contributions. This electroanalytical technique involves the study of voltage transients at an electrode upon which is imposed a constant current [99]. Figure 18 shows the cycling performance of a Li-S cell obtained from galvanostatic cycling. From this analysis, it is possible to gather important information regarding electrochemical process occurring upon charging and discharging, translated by the capacity variation. The calculation methods are reported in Appendices I.

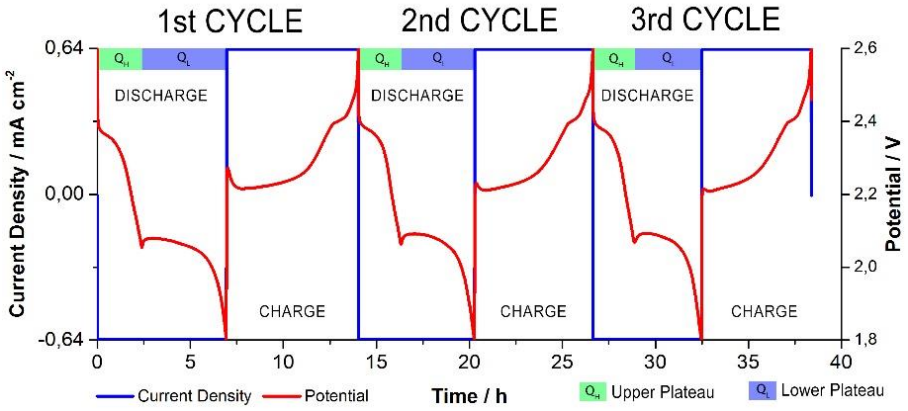

Figure 18 - Schematic illustration of recorded potential response derived from applying a constant current, in a Li-S cell. The blue and red lines are the imposed current density and potential variation, respectively. On top of each curve are illustrated the upper and lower discharge capacities, in green and purple, respectively

3.5.2. Protocols

After assembling the cells, they were submitted to galvanostatic tests using a BaSyTec CTS-LAB system. Cells with carbon-coated separators were cycled within a voltage range of 1.8-2.6 V, starting with discharge, at current densities 0.64 mA cm^{-2} (0.5 mA), followed by 1.27 (1.0 mA), 2.55 (2.0 mA) and 3.82 (3.0 mA), and ending with 0.64 mA cm^{-2}, with electrolyte E1.

To study the effect of the best performing carbon-coating on preventing the shuttle effect, cells with pristine separator and carbon-coated separator were galvanostatically cycled 5 times at a current density of 0.64 mA cm^{-2} within a voltage range of 1.8-2.6 V, with electrolyte E2.

For SEM investigations, cells with pristine separator and the best performing carbon-coated separator, were cycled 5 times at a current density of 0.64 mA cm^{-2}, with electrolyte E2. Then the cells were disassembled inside an argon filled box and the cycled anodes were carefully retrieved and placed in a vacuum-tight transfer chamber, and transferred to a scanning electron device.

Cells cycling with Li_2S cathodes started with charge, and a first upper cut-off voltage was defined to 3.8 V, while the subsequent discharge and charge was performed at a voltage range of 1.8-2.6 V, at current densities 0.64 mA cm^{-2}, followed by 1.27, 2.55 and 3.82, and ending with 0.64 mA cm^{-2}, with electrolyte E1.

3.5.3. Data representation

In order to have the most accurate and reproducible results possible, it is important to have well defined and repeatable experimental procedures and measurement techniques. Since the manufacturing process of the carbon-coated separators, electrodes, and further cell assembly was done almost entirely by manual work, the results can be influenced. In order to be as precise as possible, three cells were built for each experiment. The systematic errors were eliminated as much as possible by means of calibrated measuring devices and instructions into the working methodology. The accidental errors can, however, not be avoided through precise operation and can lead to errors [100].

In Figure 19 is shown the discharge capacity of the three cells as an arithmetic mean value with the standard deviation expressed by error bars.

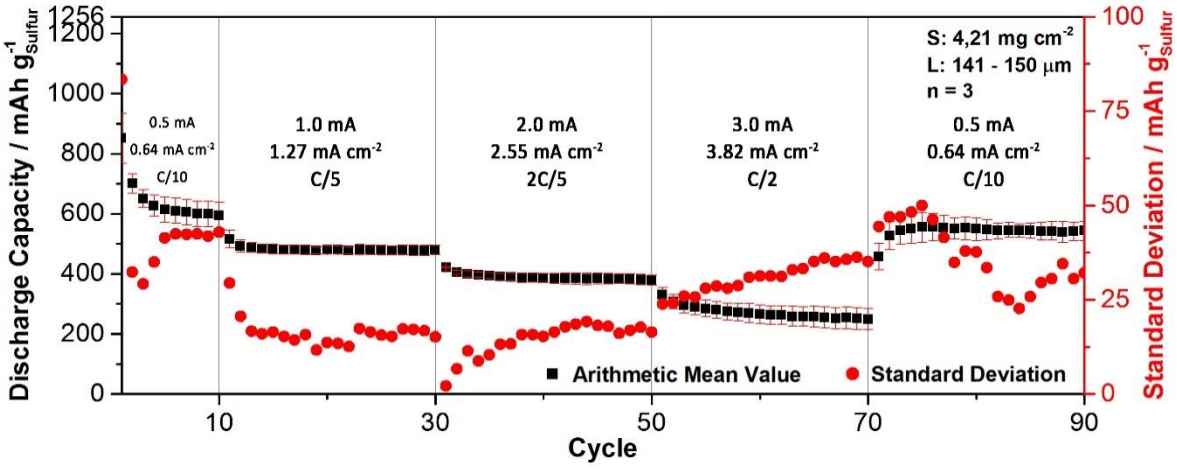

Figure 19 - Representation of the error through the standard deviation for comparison of the discharge capacity of three cells. The arithmetic mean value corresponds to (■) and the standard deviation (●). The left axis represents the discharge capacity with respect to the mass of sulfur, and right axis represents the standard deviation. Above are represented the cycle number. On the top left corner are listed the average sulfur loadings (S), the thickness range (L) of the cathodes analyzed, and the number of samples (n) used for the data representation. Inside are mentioned the current applied, in mA, current density applied, in mA cm^{-2}, and the C-rates.

The arithmetic mean value $\bar{z}$ is calculated with the actual measured z_i value, with n the number of samples. The arithmetic mean value $\bar{z}$ was calculated with Eq. 17. The standard deviation or mean error of the measurement is calculated according to Eq. 18.

$$\bar{z} = \frac{1}{n}\sum_{i=1}^{n} z_i \tag{17}$$

$$\sigma_{\bar{z}} = \sqrt{\frac{1}{n-1}\sum_{i=1}^{n}(z_i - \bar{z})^2} \tag{18}$$

Nevertheless, in some cases, the representation of the results was done with respect to the best-performing sample of the three, for the sake of brevity.

3.6. Scanning electron microscopy

Scanning electron microscopy (SEM) permits the observation and characterization of materials by detecting several types of imaging signals, such as secondary electrons (SE), backscattered electrons (BSE) and characteristic x-rays (EDX), each produced from the interaction of the electron beam with the sample.

SE are produced by inelastic interactions of beam electrons with valence electrons of atoms in the sample, which cause the expulsion of the electrons from the atoms. The detection of these electrons allows to investigate the surface topology of the sample. On the other hand, BSE are produced by the elastic interaction of beam electrons with atoms in the sample. Therefore, BSE detection provides direct information on compositional heterogeneity through the mechanism of atomic number contrast. Higher intensities, correlated with brighter intensity, are obtained in targets of high atomic number, and targets of low atomic number, correlated with dark colors, are obtained in targets of low atomic number.

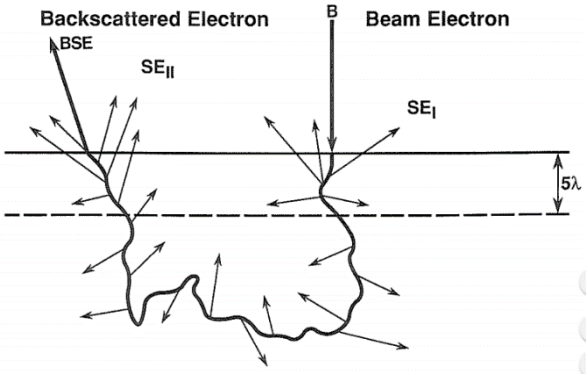

Figure 20 - Schematic illustration of the origin of SE_1 and BSE. Incident beam electrons (B) generate secondary electrons (SE) upon entering the sample. Backscattered electrons (BSE) are electrons which escaped the specimen due to deviations generated from the multiple elastic scatterings when interacting with the atoms [101].

Characteristic x-ray photons provide a semi-quantitative analysis of the elements in the sample. The interaction of the beam electrons with the specimen atoms, ejects electrons from the atom, leaving the atom in an excited state. After the atom relaxes to a state of lower energy, a characteristic x-ray photon is emitted, through the transition of an electron from the outer shell to the inner shell, as illustrated in Figure 21.

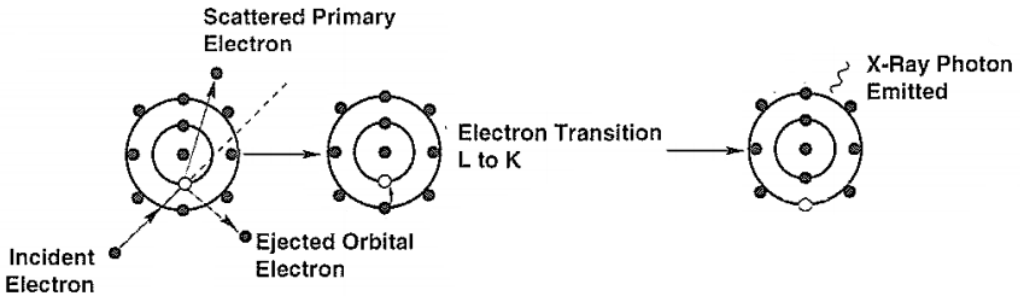

Figure 21 – Inner shell electron ejected from the atom and subsequent de-excitaton by electron transitions. Figure adapted from Goldstein *et al*. [102].

3.6. Characterization methods

Ex-situ imaging techniques, such as secondary electron (SE), back-scattered electron detection (BSE) and energy dispersive X-ray spectroscopy (EDX) were performed to investigate the morphologic changes and elemental signals on the anodes, with a scanning electron microscope Zeiss, EVO MA 10. Thickness and topology inspections of the carbon-coated separators were performed with a confocal microscope NanoFocus, μsurf, and micrometer. The mass of the cathodes and the carbon-coated separators was performed with a digital analytical balance.

Chapter 4 – Results and Discussion

To demonstrate the efficacy of the carbon coated separators on the cycling performance of Li-S cells, several studies were conducted. First, a detailed discussion of the coating method used in this work was performed, appointing the several improvements adopted. Next, SEM investigations were carried on the carbon-coated separators, to determine the coating range of the adopted method. Then, the results of galvanostatic cycled cells employing the produced carbon-coatings were discussed and compared with other authors. Further studies were conducted on the best-performing carbon-coatings regarding the trapping capability of polysulfides, by analyzing the cycling performance using an electrolyte without the $LiNO_3$ additive. Finally, morphological, structural and elemental studies were conducted through SEM, on pristine metallic lithium and cycled metallic lithium anodes, from cells employing pristine separator and the best-performing carbon-coating, to understand the corrosion extent in the metallic lithium. Additionally, the results regarding the cycling performances of solvent-free Li_2S cathodes with different compositions are presented and discussed.

4.1. Optimization of alternative Langmuir-Blodgett coating method

In this thesis, an alternative way of coating polyolefin separators employed in Li-S batteries was used. This technique, named as Langmuir-Blodgett Scooping (LBS) by Kim *et al.*, allows the efficient creation of multifunctional, layer-by-layer coatings of carbons, metal-oxides, polymers and the combination of these materials on a non-reactive substrate, without any device typically used in the production of LB films. Unlike the conventional LB method, which uses external mechanical force to a disordered material at the air-water interface to create well-ordered assemblies of particles, the LBS uses self-assembly to create ordered coatings that can be transferred to a substrate. This difference allows the fast creation of highly packed layers, with a precise control over the film thickness and structure [103]. Moreover, the method introduced by Kim *et al.* was further optimized in this project by understanding which parameters could be improved to obtain high-quality LB coatings of carbon nanoparticles.

The LBS coating process has two distinct stages, a film formation regime upstream and a coating regime downstream, as shown in Figure 22.

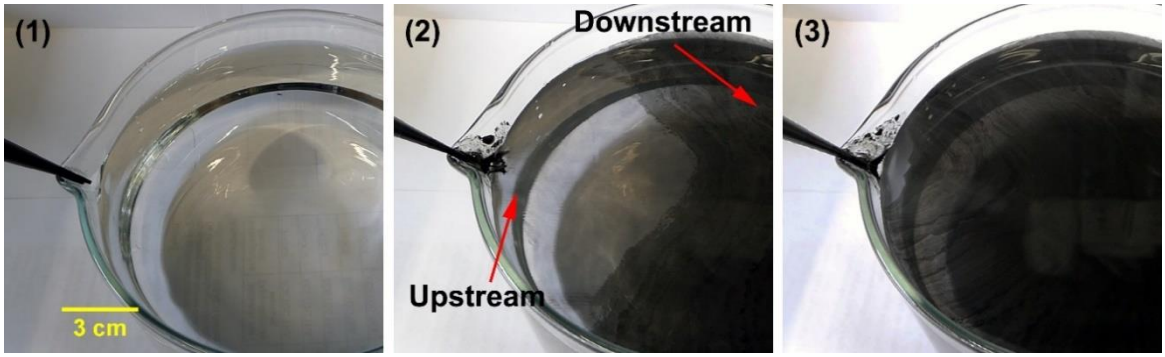

Figure 22 – Langmuir film forming process. (1) Before the injection of suspension onto the water surface; (2) Continuous injection of suspension, resulting in the formation of a Langmuir film. At the upstream region, occurs the self-assembling process. (3) Fully covered water surface with nanomaterial.

The film formation region is where the particles are assembled in a thin film at the air-liquid interface aided by the stress imparted by the flow of the suspension. Instead of the relatively stagnant regime found in a Langmuir-Blodgett experiment, the suspension continuously advects the particles downstream while spreading out the film. The coating and deposition occurs at the end of the containment, where the film contacts the substrate. Nevertheless, the ideal mode of this deposition is complex and depends of several conditions, which will be discussed below.

The production of the carbon-coated separators was possible by conceiving a 3-stage protocol, summarized in Figure 23. The developed methodology was obtained through continued

experimentation and further adjustment of the parameters that compromised the stability and homogeneity of the layer upon the formation at the air-water interface and further transfer to the substrate.

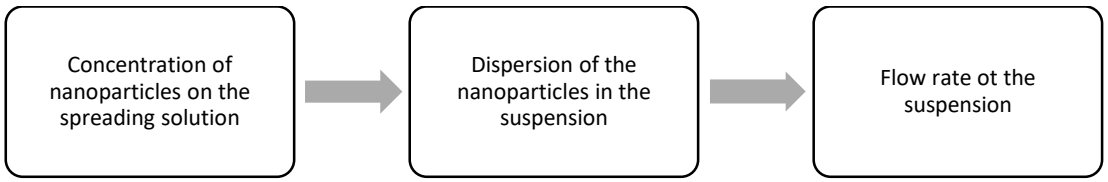

Figure 23 - Interdependence of parameters required to obtain high quality LB coatings.

The three main parameters that influence the quality of the film are the concentration and level of dispersion of the carbon nanoparticles on the spreading solution, and the flow rate of the suspension upon the formation of the film on the air-water interface. Nevertheless, other factors were taken into account. It was observed that a poorly washed containment destabilized the formation of the film. As shown in Figure 24, the spread nanomaterial could not fill completely the water surface due to repulsive forces originated from traces of residues on the walls. On the other hand, a fully covered water surface with nanomaterial was achieved in the cleaned container. In this regard, a cleaning protocol of the equipment through the course of the LBS experiment is mandatory.

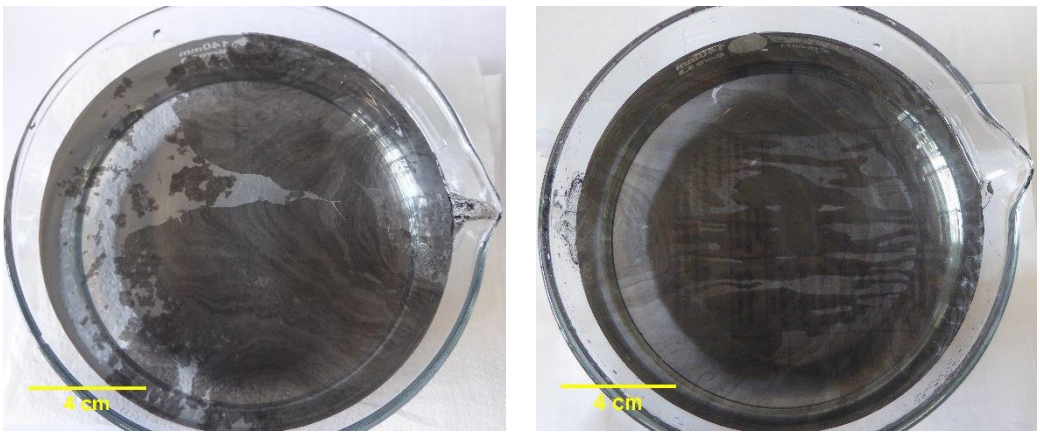

Figure 24 - Langmuir films in a poorly washed containment (left) and in a clean containment (right).

The concentration of the nanoparticles in the spreading solvent determined the existence of clusters in the films, which is demonstrated by the negative influence these have on the homogeneity and stability of the layer, as shown in Figure 25. As observed in the close-up picture, the borders of the clusters repel the nearer particles, forming open spaces. Therefore, it was necessary to find the ideal concentration of the suspensions to minimize the existence of the clusters.

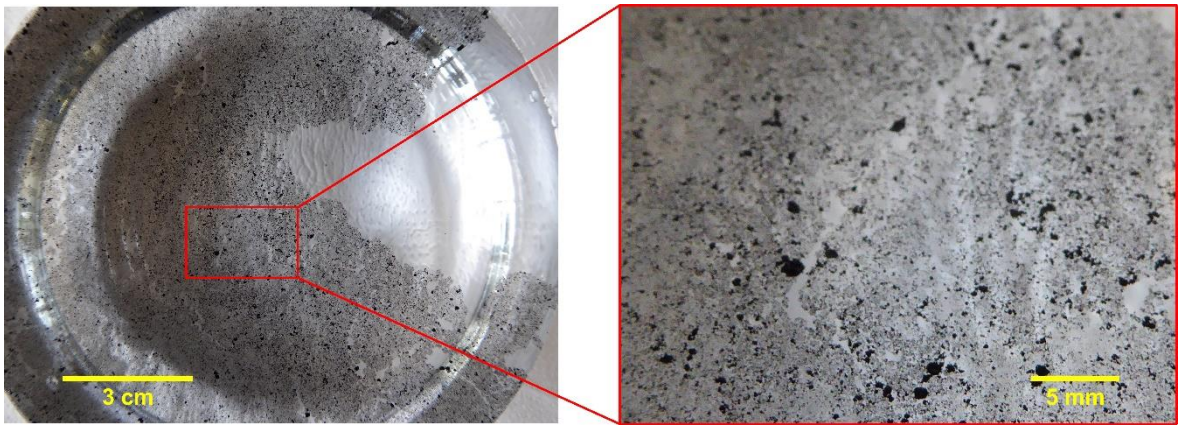

Figure 25 - Langmuir film of MWCNT with a suspension concentration of 7.970 mg ml^{-1} (1.0 wt. %).

The investigation was taken by preparing several sonicated and shear-mixed solutions with nanomaterial concentrations between 0.790 (0.1 wt. %) and 7.970 mg ml^{-1} (1.0 wt. %), and tested by producing films at the surface of the water. It was found that KB and SC carbons formed uniform LB layers, with no agglomerates visible to the naked eye, at concentrations 0.790 (0.1 wt. %) and 2.771 mg ml^{-1} (0.35 wt. %), respectively. A similar approach was performed with MWCNT, but even at the lowest concentration adopted, 0.790 mg ml^{-1} (0.1 wt. %), agglomerates were found in the LB film, as shown in Figure 26. Therefore, different approaches should be conducted to minimize the presence of agglomerates, especially when using MWCNT to produce LB films.

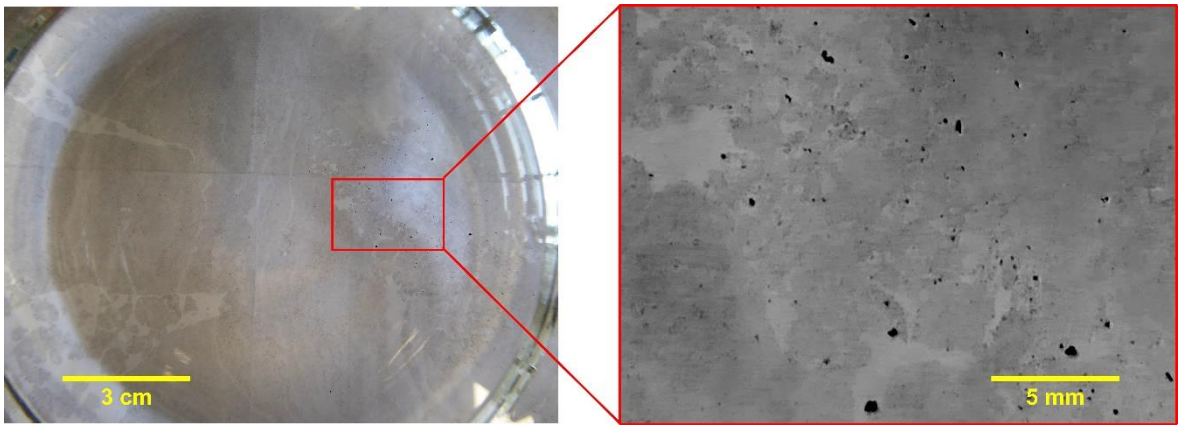

Figure 26 - Langmuir film of MWCNT with a suspension concentration of 0.790 mg ml^{-1} (0,. wt. %).

Further improvement in the dispersibility of the carbon nanoparticles in the solution was obtained by mechanical dispersive techniques – sonication and high-shearing blending -, common techniques applied for dispersing carbon nanoparticles in solvents. Dispersion through sonication results from cavitation, where the nanoparticles are continuously dispersed in the liquid medium by bubble nucleation and consecutive collapse, leading to jets of liquid at high velocity. Two approaches for delivering the ultrasonic energy into the suspensions could be attempted: ultrasonic bath or ultrasonic horn. Ultrasonic bath was chosen since the energy is more uniformly dispersed through the liquid phase [104], contrary to ultrasonic horn which produces inhomogeneous energy dispersion and damages the walls of the MWCNT [105]. Nevertheless, it has been found [105] that for long periods of sonication, the bath temperature increased, and affected the level of aggregation of the carbon nanoparticles. The temperatures rise is due to the production of cavitation bubbles which undergo short and violent collapse within the fluid generating localized hotspots of high energy, resulting in the increase of the baths temperature. To stabilize the increase of temperature, ice was constantly added to the oscillating tank. Furthermore, Hilding *et al.* [106] reported that the exposure time of sonication has a negative impact on the MWCNT tube length. A significant decrease of length was observed in the first minutes, stabilizing gradually with longer exposure periods. Regarding this finding, it was stablished a nominal exposure time for sonication of 15 minutes, half of the exposure time used by Kim *et al.* [103], to preserve as much as possible the original characteristics of the nanotubes.

To pull agglomerates apart, a high-shearing blending route was applied, which induces high shear mixing, through a high-speed disperser. Due to the high-rotation speed of the rotor, the mixture is drawn axially into the dispersing head and then forced radially through the slots in the rotor/stator arrangements. The high acceleration acting on the material produces extremely strong shear forces, managing to decrease the size of the agglomerates [107], as shown in Figure 27. Although this dispersing method showed good results in terms of dissagglomeration in every type of carbon, it can also induce fractures, especially on MWCNT [108]. To minimize the damage, it was established an exposure time of 30 seconds at 3×10^4 rpm.

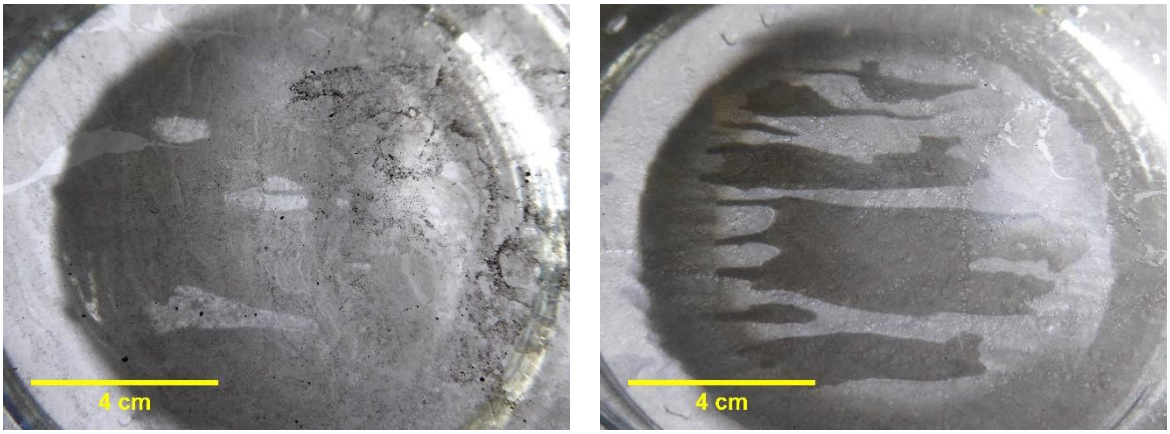

Figure 27 – Effect of high-shear mixing on dissagglomeration of MWCNT (0.1 wt%); on the right is shown a film produced with an ultrasonicated suspension and on the left is a films produced with a ultrasonicated and high-shear mixed suspension.

Upon removal of the external shear stress, the MWCNTs in low viscosity solvents would reconfigure themselves to a new equilibrium state of low energy, through re-aggregation. By adding a surfactant to provide static charge repulsion, e.g. sodium dodecyl sulfate (SDS) or Triton X-100, it is possible to cease the re-aggregation process [109], although the characteristics of the suspension would not be appropriate to produce afterwards a LB film. Thus, after finishing the dispersion and de-agglomeration steps, the suspension was used right after, while being kept in a recipient with ice.

Another important factor that determines the quality of the coating is the flow rate of the suspension. When the injection is performed manually, with Pasteur pipette or micrometric pipette, one is not able to control with precision the injection of suspension, leading to defective LB layers and loss of nanomaterial into the subphase (Figure 28). These defects account the varied packing densities and collapse of the layer, which resulted from the formation of faults or discontinuities (Figure 29). In order to maintain a constant injection, a syringe pump was used to produce stable and homogeneous LB films. To investigate the optimal injection speed, several LB films were produced varying the flow rate, until stability and homogeneity of the film was observed. It was found that for the given conditions, concentration and dispersion of nanomaterial in the spreading solvent, the optimal flow rate was 1000 µl min^{-1}.

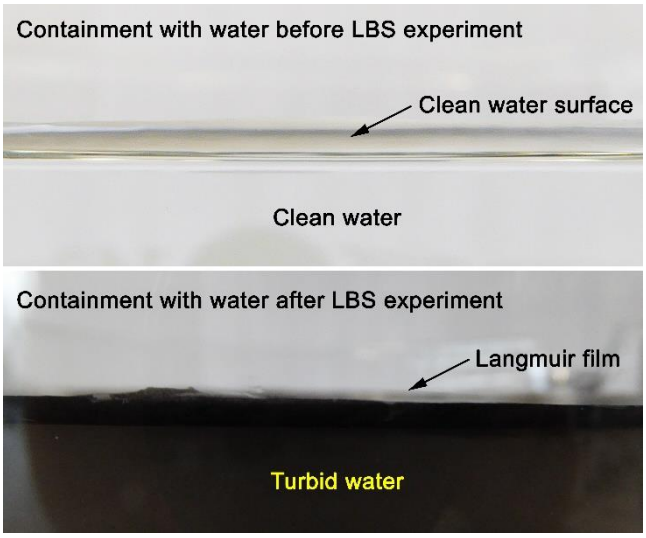

Figure 28 - Loss of nanomaterial in the subphase, using Pasteur pipette as injection equipment.

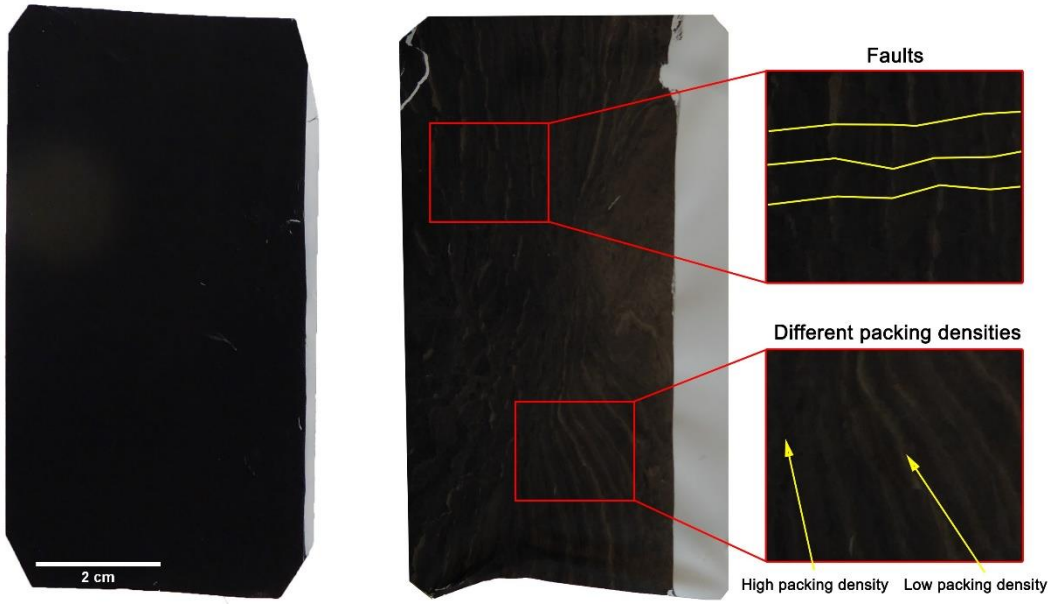

Figure 29 – SC (0.35 wt. %) coatings on separator using a syringe pump (left) and Pasteur pipette (right); the defects are illustrated at the right side: on top, the faults are marked with lines, and on the bottom, the packing densities are evidenced by the variable optical clarity: whiter parts are denominated as low packing density zones, and the darker as high packing density zones.

In sum, by tuning the three parameters, it was possible to produce multi-layered carbon coatings on a separator. In Figure 30 are shown images of a separator coated with 10 layers of SC, using the optimized LBS method, and a punched carbon-coated separator, seen from the front side, back side and folded. The front side of the separator, with the multi-layered carbon-coating, faces the cathode surface, while the back side will be in direct contact with the anode surface. Here, it is evident that with the adopted coating technique only one side of the separator was coated, while the other remained unaltered. Moreover, with this technique, it was possible to coat a wide surface area of the separator, enabling the further use in pouch cells.

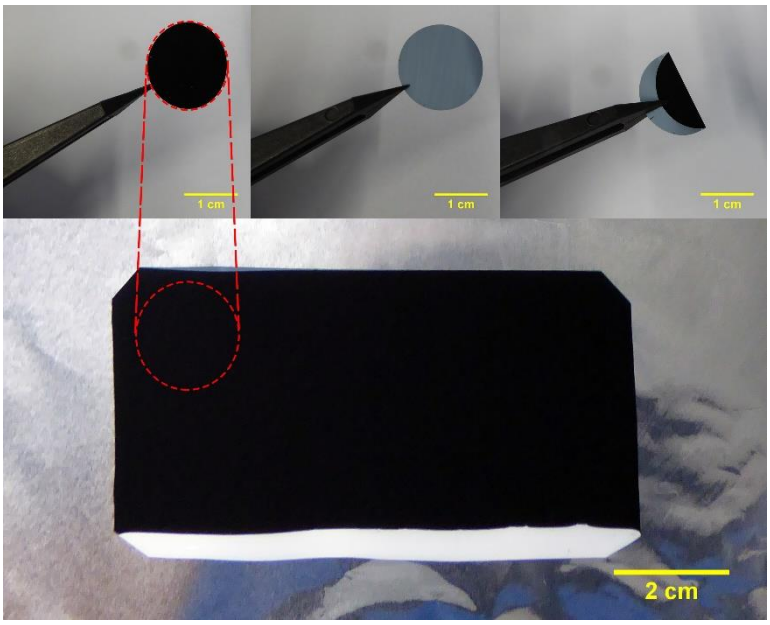

Figure 30 – Coated separator with 10 layers of SC and punched separator for further use in cells. On top are shown images of the pouched separator, seen from front side (left) and the back side (center), which faces the cathode surface and the anode, respectively, and folded (right).

After producing the multi-layered carbon coatings, the average carbon loading and thickness were investigated, and the results shown in Figure 31.

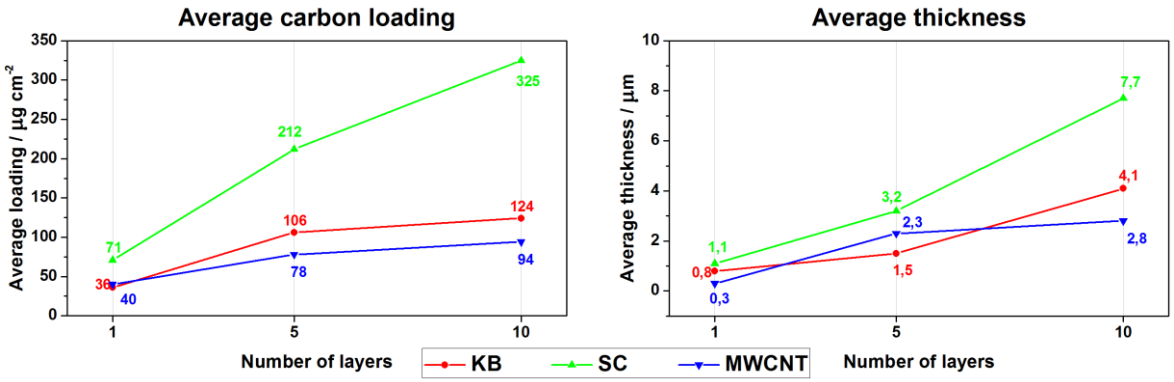

Figure 31 – Average loading of carbon nanoparticles on separator (left) and thickness of carbon coating (right) in function of number of layers.

It is clear that the increase of thickness and carbon loading follows the number of deposited layers on the separator. Carbon coatings of MWCNT show the lowest values of loading and thickness, followed by KB and SC. Moreover, it is worth mentioning that the separator's weight is 1.3 mg cm^{-2}, four times heavier than the heaviest carbon-coating produced, 10 layers of SC. Thus, the introduction of a carbon-coated separator would not influence the specific energy of a cell.

4.2. Coating range of the alternative Langmuir-Blodgett coating method

After the production of the carbon-coated separators, the morphology and structure of the coatings were analyzed to understand the coating range of the alternative Langmuir-Blodgett coating method. Figure 33 and Figure 34 show plane view SEM images of the carbon-coated separators at a magnitude of 100 × and 20.00k ×, respectively. As a term of comparison, an additional SEM of a separator was added, which can be seen in Figure 32.

The SEM image of the separator at a magnification of 100 × shows a smooth surface with a defined pattern of parallel lines. When increasing the magnification to 20.00k ×, it exhibits an evenly distributed submicrometer pore structure. Such structure, consisting of multiple pores with an average pore size of 43 nm [79], is incapable of confining the soluble polysulfides, which have dimensions ranging between 1.0 and 1.8 nm [8], thus allowing the diffusion of these species through the cell. Therefore, a severe decrease of capacity on cells harboring pristine separators is expected.

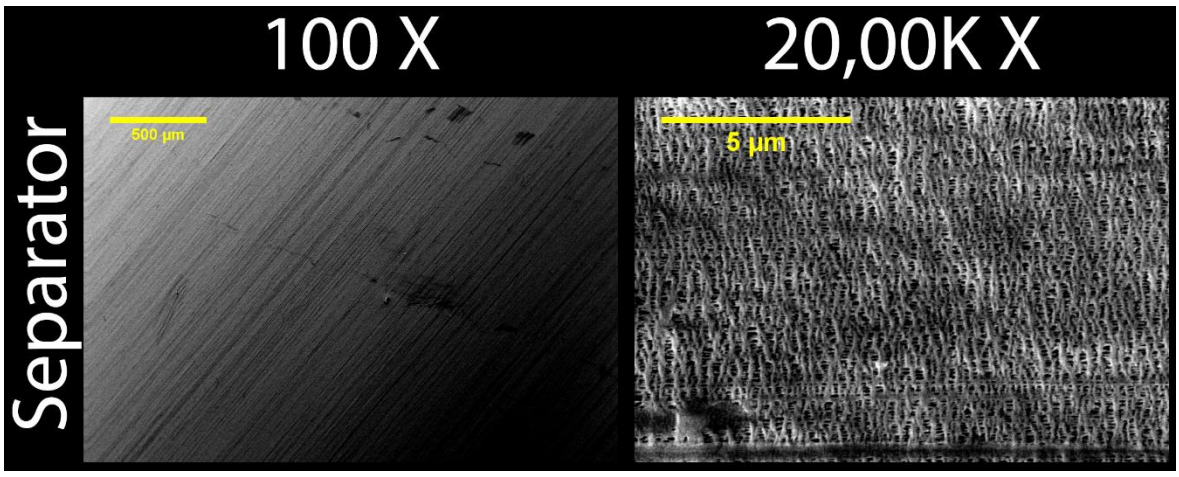

Figure 32 - SEM micrographs of pristine separator, at a magnification of 100 × and 20,00k ×.

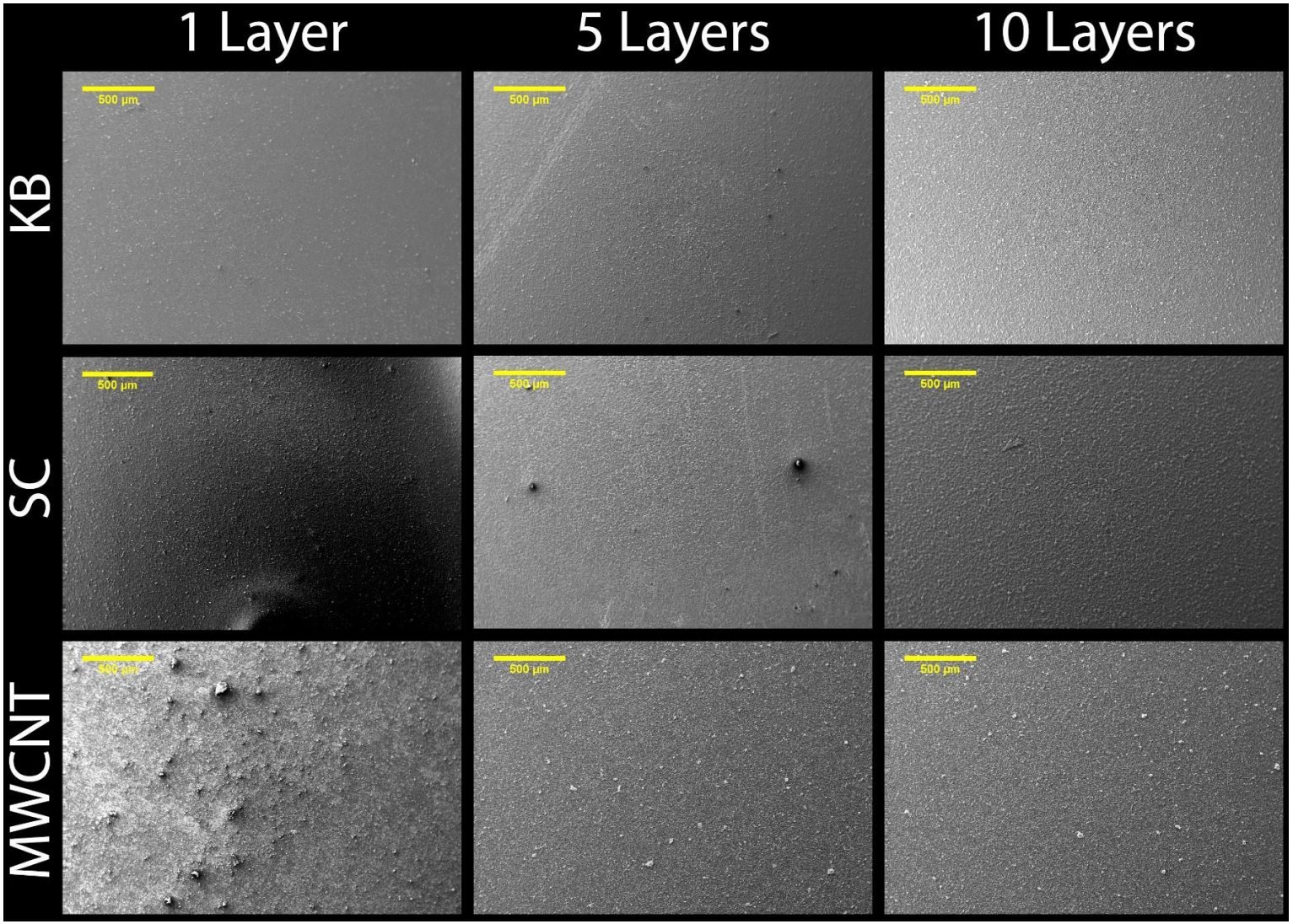

Figure 33 – SEM micrographs of separators coated with KB, SC and MWCNT, with 1, 5 and 10 layers, at a magnification of 100 ×.

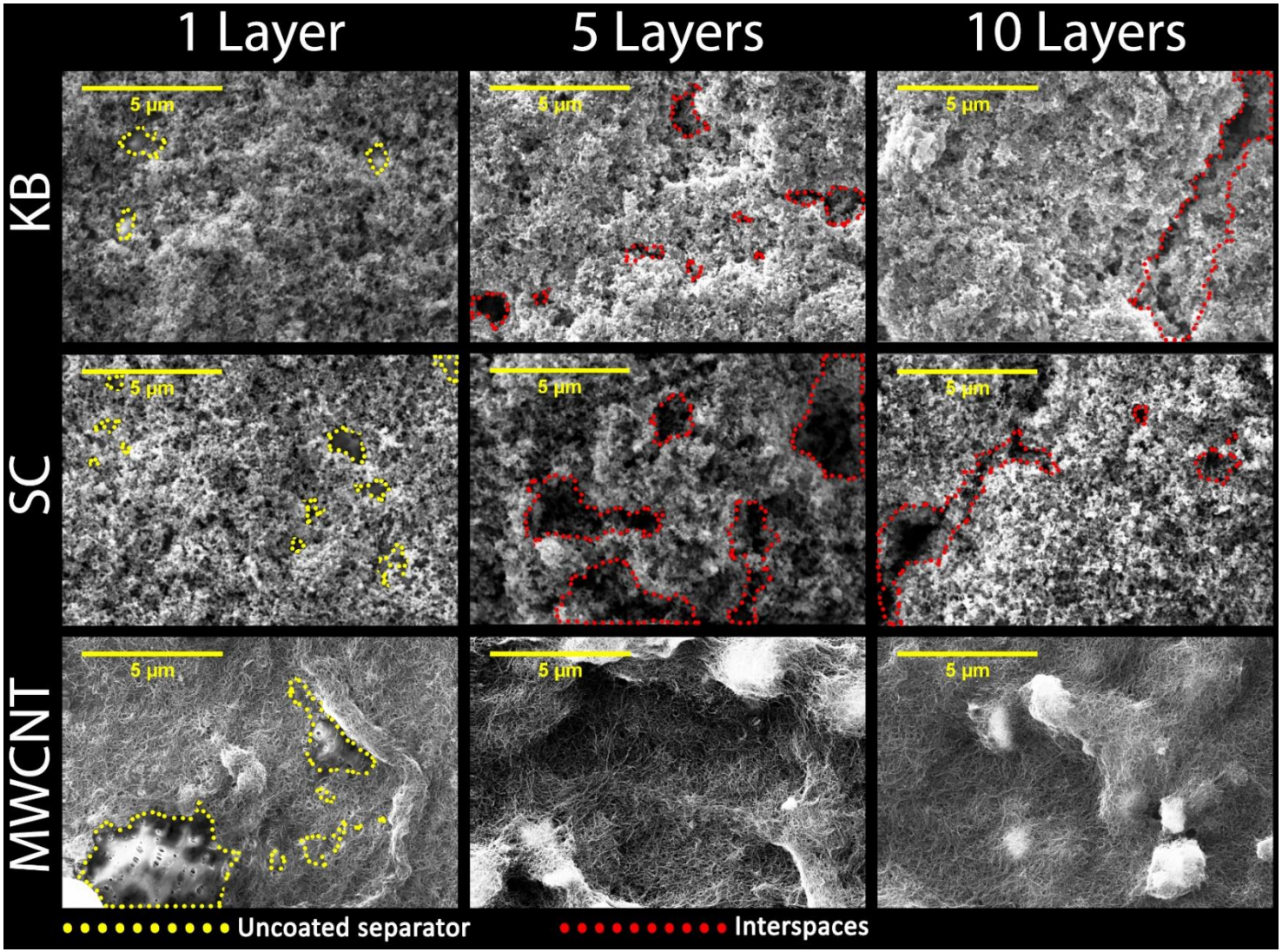

Figure 34 - SEM micrographs of separators coated with KB, SC and MWCNT, with 1, 5 and 10 layers, at a magnification of 20.00k ×. Uncoated areas of the separators and interspaces between the carbon nanoparticle clusters are identified by yellow and red doted outlines, respectively.

In Figure 33 are shown plane view SEM images of the produced carbon-coated separators, at a magnification of 100 ×. As noticed, the defined pattern of parallel lines identified in Figure 32 disappeared, evidencing that the coating technique provided a high coverage of the separators surface. Regarding the presence of clusters on the coatings, these are present in all analyzed samples, although some are more easily identified than others. As discussed in section 4.1, the creation of ideally homogeneous coatings of MWCNT was not possible due to the characteristics of the nanotubes, therefore, even at the naked eye, clusters of MWCNT were found on the coatings. In the SEM observations, the clusters can also be identified as randomly dispersed agglomerates, and are more pronounced in separators coated with MWCNT. Nevertheless, minor sized clusters can also be found in other carbon-coated separators.

Figure 34 shows SEM images of the carbon-coated separators at a magnification of 20.00K ×. KB and SC coatings consist of highly porous stacked nanoparticle clusters, while MWCNT-coatings consist of crisscrossed entangled nanotubes. These structures can serve as physical barriers to prevent the diffusion of polysulfides, while maintaining the electrochemical utilization of the species. Moreover, the carbon networks could improve the reactivation of sulfur deposits at the cathodes surface, formed with long cycling, due to the superior electric conductivity of the carbons, and alleviate the volume variations due to the high porosity evidenced. Analyzing the images of the coated separators with one layer of carbon, all show spots where the porous structure of the separator is observed (yellow dotted outlines). In this view, it is possible to state that the method applied to coat the separators was not able to fully cover the separator's surface. In this regard, it is expectable that cells employing separators coated with one layer of carbon material will not achieve significant results in terms of performance enhancement, since the separator was not fully covered, thus soluble species could migrate through the separator. With increased number of layers, these spots vanish. Nevertheless, separators coated with KB and SC show interspaces (red dotted outlines) between the carbon clusters, while separators coated with MWCNT show no interspaces. These interspaces could negatively affect the Li-S cells, since polysulfides can move freely in these areas, and, at the worst case, migrate through the separator.

4.3. Electrochemical performance of cells with carbon coated separators

In this section are shown the rate cyclability examinations of cells with carbon-coated separators, employing electrolyte E1, which contains $LiNO_3$ additive, known for its effect on suppressing efficiently the polysulfides shuttling. As a term of comparison, electrochemical data of cells with a pristine separator were added to understand the effects of the carbon coatings on the overall capacity. Moreover, to comprehend the electrochemical characteristics of the carbon coatings, the investigation of the upper plateau (Q_H) and lower plateau (Q_L) discharge capacities were used as a quantitative evaluation for the polysulfide retention level and redox ability, respectively [12, 10]. As described in section 2.4.1, the upper plateau is related to the solid-liquid reaction from sulfur to high-order polysulfides, thus, this step involves the formation, dissolution and migration of soluble polysulfides, giving rise to the degradation of the capacity. The lower plateau, on the other hand, corresponds to the sluggish reaction of soluble polysulfides to solid Li_2S_2/Li_2S that involves low reaction kinetics. By analyzing the variation of the upper plateau discharge capacity, it is possible to demonstrate the polysulfide trapping capability of the carbon-coated separators. The analysis of the lower plateau discharge capacity variation gives information regarding the effect of the carbon-coated separators on the reduction of the intercepted soluble polysulfides. In addition, the sulfur utilizations were added in the following charts, and is the ratio between the practical and theoretical specific capacities. Its quantification allows to understand how much sulfur is electrochemically active, thus contributing to the electrochemical process. The same methodology was used to calculate the upper and lower plateau contributions. Understanding the magnitude of each plateau contribution provides the necessary information to determine the effect of the carbon-coating on the trapping and utilization of soluble polysulfides (upper plateau), and efficient reduction of polysulfides to Li_2S_2/Li_2S (lower plateau).

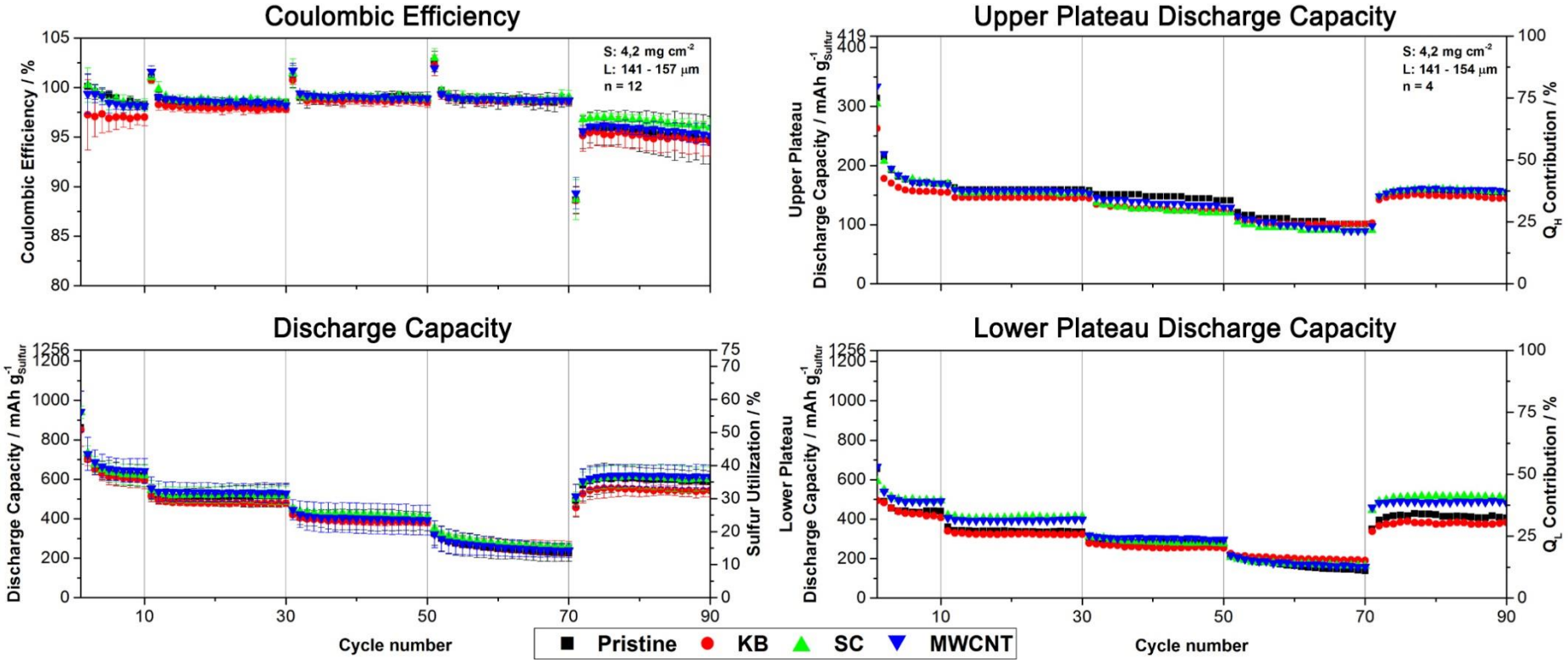

Figure 35 - Electrochemical performance and corresponding coulombic efficiency, and plateau contributions of cells with separator coated with 1 layer of carbon. On top are shown the coulombic efficiencies, and below is represented the corresponding cycling performance of the analyzed cells, where the left axis represents the discharge capacity, and the right axis the sulfur utilization. The other two graphs represent the upper and lower plateau discharge capacities of the best-performing cells of each group analyzed. The left and right axis show the plateau discharge capacity and corresponding plateau contribution, respectivelly. On the top of each chart are given the average sulfur loading and range of thicknesses of the cathodes. The carbon coatings are represented by colored symbols: KB corresponds to (●), SC (▲) and MWCNT (▼). Cells with bare separator correspond to (■).

Starting with the analysis of the rate cyclability in Figure 35, the discharge capacities of the different cells seem to be overlapped, although some differences could be noted. When first cycled at 0.64 mA cm^{-2}, cells with MWCNT@1L show the highest first discharge capacity, 943 (56%) mAh g^{-1}, followed by SC@1L, 939 (56%) mAh g^{-1}, and pristine, 862 (52%) mAh g^{-1}. Cells with KB@1L show the lowest first discharge capacity of all analyzed cells, with 851 (51%) mAh g^{-1}. Although high sulfur utilizations, shown in the parentheses, were obtained in the first cycle, a fast decay of capacity was reported on the following cycles for all analyzed cells, stabilizing after the fifth cycle. This fast deterioration of capacity results mainly from the loss of active material in the form of soluble species in the electrolyte [110, 8]. At the tenth cycle, similar capacities for all cells were reported. For cells with pristine separator and carbon coated-separators of KB@1L, SC@1L and MWCNT@1L, the discharged capacities are 618 (37%), 595 (36%), 619 (37%) and 642 (38%) mAh g^{-1}, respectively.

When discharged at higher current densities, the overall capacities decrease. Hypothesis for this decrease of capacity could be energy losses due to polarization [22], but also the thickness variation of Li_2S at high current densities [43]. After discharged at 4,32 mA cm^{-2}, the cells were once again cycled at 0.64 mA cm^{-2}, the same imposed current density on the first 10 cycles. As shown, the capacity significantly increases to values approximately equal to the first cycles, with the exception of KB@1L which shows an overall decrease of capacity. At the last cycle, the cells with pristine separator and carbon-coated separators of KB@1L, SC@1L and MWCNT@1L, show capacities of 587 (35%), 543 (32%), 599 (36%) and 613 (37%) mAh g^{-1}.

Regarding the coulombic efficiency, in overall all the cells demonstrate high values, approximately 99%, with exception of cells with KB@1L, which shows lower values at the first cycles but further increases with cycling. Nevertheless, after the seventieth cycle, a decrease of the coulombic efficiency was detected in all tested cells. This decrease suggests that changes occurred in the electrochemical system, which influenced the charging/discharging times.

Analyzing the upper plateau discharge capacities of the cells, it seems that the carbon-coatings with one layer of carbon did not contribute to the trapping of these soluble species, since the curves are overlapped. Nevertheless, when analyzing the low plateau discharge capacity, cells with SC@1L and MWCNT@1L seem to slightly enhance the reduction of the polysulfides at the end of discharge, since they are above the curve that represents cells with pristine separator. Therefore, it is possible to conclude that the slight increase of discharge capacity observed on the rate cyclability graph is due to the enhancing reduction potential supplied by the carbon-coatings. On the other hand, cells with KB@1L demonstrated to have no enhancing effects on the increase of reduction potential.

From the previous analysis it was found that the introduction of a layer of KB onto the separator did not improve the capacity of the cells. On the other hand, the cells with one layer of MWCNT and SC, demonstrated higher capacity outputs. These results were already expected. Evoking the SEM investigations performed on the separators coated with one layer of carbon material, it was observed that certain areas of the separator were not fully covered, thus allowing the loss of soluble lithium polysulfides from the cathode.

Rate cyclability of cells employing separators coated with 5 layers of carbon material

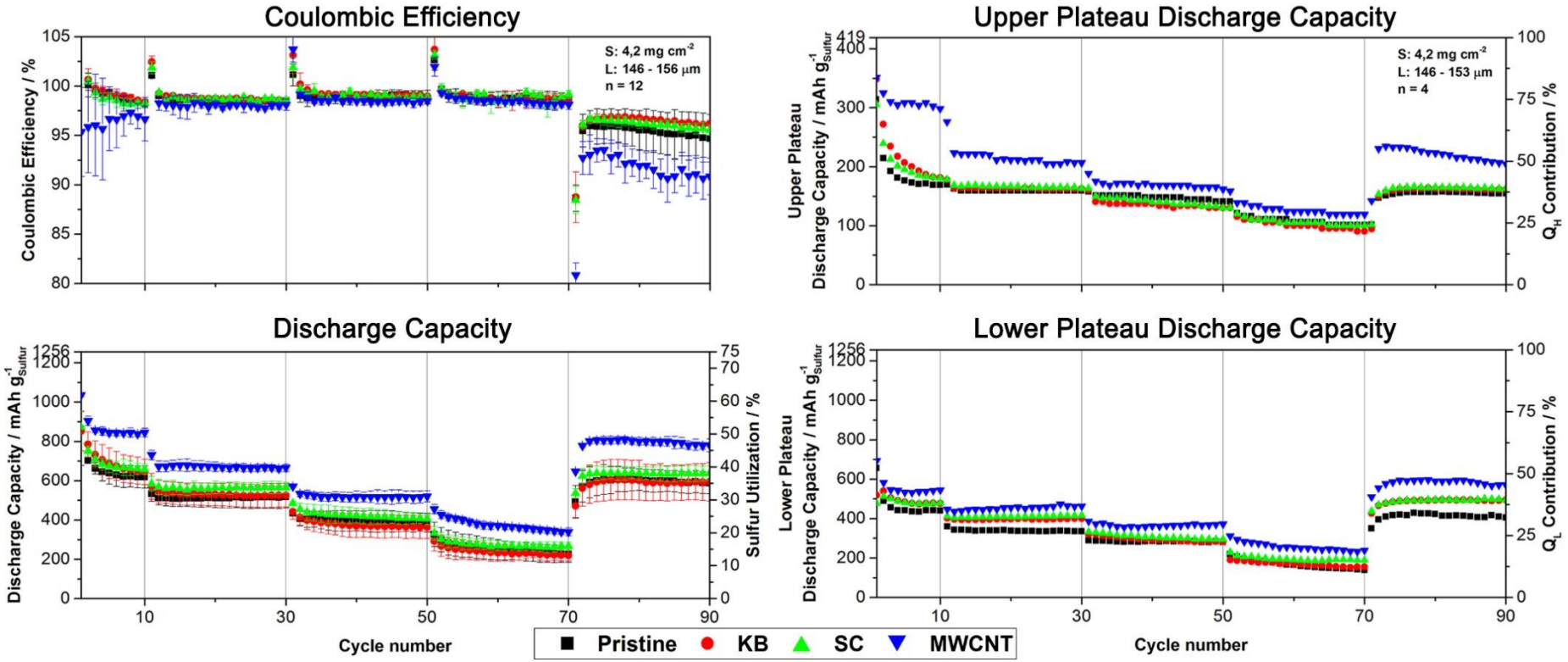

Figure 36 - Electrochemical performance and corresponding coulombic efficiency, and plateau contributions of cells with separator coated with 5 layers of carbon. On top are shown the coulombic efficiencies, and below is represented the corresponding cycling performance of the analyzed cells, where the left axis represents the discharge capacity, and the right axis the sulfur utilization. The other two graphs represent the upper and lower plateau discharge capacities of the best-performing cells of each group analyzed. The left and right axis show the plateau discharge capacity and corresponding plateau contribution, respectivelly. On the top of each chart are given the average sulfur loading and range of thicknesses of the cathodes. The carbon coatings are represented by colored symbols: KB corresponds to (●), SC (▲) and MWCNT (▼). Cells with bare separator correspond to (■).

In Figure 36 are shown the rate cyclability of cells with separators coated with five layers of carbon, corresponding coulombic efficiency, and the contributions of the two plateaus. From a first impression, cells with MWCNT@5L provided a boost of capacity while cells with SC@5L and KB@5L delivered a slight increase of capacity. The first discharge capacity of cells with pristine separator and carbon-coated separators of KB@5L, SC@5L and MWCNT@5L are, respectively, 862 (52%), 851 (51%), 872 (52%) and 1036 (62%) mAh g^{-1}. On the subsequent cycles, all the cells show the typical fast decline of capacity due to the loss of soluble active material, however, cells with MWCNT@5L demonstrate a lower decay. When cycled at higher current densities, the discharge capacity of the cells decrease, although cells with MWCNT@5L maintain always a higher capacity compared to the remaining cells.

Regarding the coulombic efficiency, cells with pristine separator and carbon-coated separator with KB@5L and SC@5L show high values, approximately 99%, over the first seventy cycles. Although, a decrease was observed when cycled again at 0.64 mA cm^{-2}, behavior also observed for cells with carbon-coated separator with one layer. On the other hand, cells with MWCNT@5L show lower coulombic efficiencies when cycled at 0.64 mA cm^{-2}, aggravating when cycled again at 0.64 mA cm^{-2}.

From the analysis of the upper plateau discharge capacity at the ten first cycles, MWCNT@5L shows significant polysulfide trapping capabilities, demonstrated by the superior upper discharge plateau capacity at first cycle, and low decay with further cycling. The upper plateau discharge capacity at the first cycle of the cell is 351 mAh g^{-1}, which corresponds to a plateau contribution of 84%, and at the tenth cycle is 298 mAh g^{-1} (71%). On the other hand, cells with pristine separator, KB@5L and SC@5L show at the first cycle an upper discharge plateau capacity of 314 (75%), 348 (83%) and 305 (73%) mAh g^{-1}, and at the tenth cycle 169 (40%), 182 (43%) and 180 (43%) mAh g^{-1}. This fast decay of upper plateau discharge capacity proves that even with an increase of number of layers, no further improvement was observed on the trapping capability of the cells with separator coated with KB@5L and SC@5L. When discharged at higher current densities, the upper plateau discharge capacity of MWCNT@5L decreases, achieving its minimum at the highest imposed current density, 3.82 mA cm^{-2}. When discharged again at 0.64 mA cm^{-2}, the upper plateau discharge capacity rises. Regarding the upper plateau discharge capacity of cells with KB@5L and SC@5L discharged at higher current densities, the values are approximately the same as the ones from cells with pristine separator. Also, when discharged again at 0.64 mA cm^{-2}, the values are relatively equal. The analysis of the lower plateau discharge capacities of the different cells showed that with the increase of carbon layers to five, higher reduction potentials were achieved. Regardless of the imposed current density, MWCNT@5L show always superior lower plateau discharge capacities compared to the other two carbons. Moreover, after the cell MWCNT@5L was cycled again at 0.64 mA cm^{-2}, it shows even higher values of lower plateau discharge capacities than the reported at the first ten cycles. Cells with KB@5L and SC@5L show similar results in terms of lower plateau discharge capacity. Moreover, the same behavior reported by MWCNT@5L is witnessed in cells with KB@5L and SC@5L when cycled again at 0.64 mA cm^{-2} – higher lower plateau discharge capacities were obtained compared to the first ten cycles. Thus, it is plausible to conclude that the introduction of additional carbon layers on the separator induced an increase of reduction potential.

It was observed that the introduction of additional carbon layers onto the separator resulted in capacity enhancement of the cells. Regarding the capacity provided by each group of cells, MWCNT@5L showed higher capacity retentions, followed by SC@5L and KB@5L, which demonstrated lower capacity improvements. By analyzing the contribution of each plateau, MWCNT@5L revealed superior upper plateau discharge capacities at low current densities, while SC@5L and KB@5L demonstrated negligible improvements at any imposed current density. However, at higher current densities, the upper plateau contribution of MWCNT@5L decreases. Regarding the lower plateau discharge capacity, MWCNT@5L shows superior results compared to the other two carbons. Moreover, when discharged again at a lower current density, the cells with carbon-coated separators show lower plateau discharge capacities slightly higher to those reported at the first ten cycles.

Rate cyclability of cells employing separators coated with 10 layers of carbon material

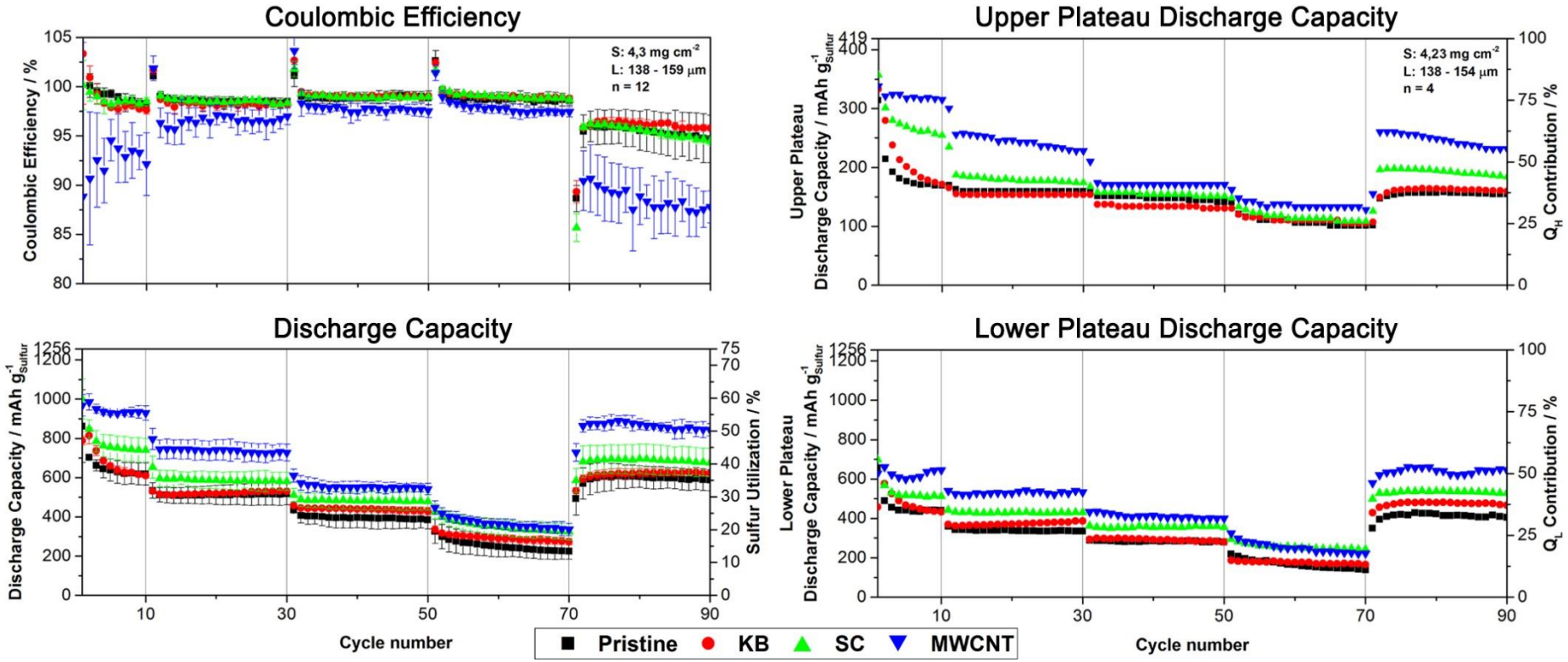

Figure 37 - Electrochemical performance and corresponding coulombic efficiency, and plateau contributions of cells with separator coated with 10 layers of carbon. On top are shown the coulombic efficiencies, and below is represented the corresponding cycling performance of the analyzed cells, where the left axis represents the discharge capacity, and the right axis the sulfur utilization. The other two graphs represent the upper and lower plateau discharge capacities of the best-performing cells of each group analyzed. The left and right axis show the plateau discharge capacity and corresponding plateau contribution, respectivelly. On the top of each chart are given the average sulfur loading and range of thicknesses of the cathodes. The carbon coatings are represented by colored symbols: KB corresponds to (●), SC (▲) and MWCNT (▼). Cells with bare separator correspond to (■).

From Figure 37, remarkable capacity improvements were reported by MWCNT@10L, as shown by a superior first discharge capacity, 968 (58%) mAh g^{-1} and the disappearance of the fast decline of capacity on the first cycles. At the tenth cycle, the reported capacity is 929 (56%) mAh g^{-1}, corresponding to an outstanding decrease of only 2%. Cells with SC@10L also show improvements in terms of capacity retention on the first cycles, although a decrease of sulfur utilization is reported. At the first cycle SC@10L shows a high discharge capacity of 1001 (60%) mAh g^{-1}, while at the tenth cycle the capacity decreases to 739 (44%), which corresponds to a reduction of 16% of the initial capacity. Cells with KB@10L show a first discharge capacity of 788 (47%) mAh g^{-1}, although, with further cycling, they decay to values approximately equal to the ones of cells with pristine separator at the tenth cycle, 609 (36%) mAh g^{-1}. When higher current densities are imposed, cells with MWCNT@10L still show higher capacity outputs compared to the other cells, although, at the highest imposed current density, it shows discharge capacities similar to cells with SC@10L. Upon decrease of current density, an increase of capacity is reported, and is maintained stable until the last cycle. At the ninetieth cycle, cells with MWCNT@10L show a capacity of 844 (50%) mAh g^{-1}. Cells of SC@10L show higher capacity outputs compared to cells with 1 and 5 layers, when discharged at higher current densities. Contrary to the results obtained by the other carbons, KB@10L shows the worst improvement of capacity output.

Regarding the coulombic efficiency, the cells KB@10L and SC@10L show high values of coulombic efficiency, approximately 98-99%, until the seventieth cycle. On following cycles, a decrease is observed, followed by a steady decay. On the other hand, the cells MWCNT@10L show lower and unstable coulombic efficiencies at the first ten cycles, followed by an increase with further cycling. However, when cycled again at 0.64 mA cm^{-2}, the values strongly decrease. Since the other cells show stable coulombic efficiency outputs, and considering that the only component that changed on the cells was the carbon material coated on the separator, it is quite probable that these instabilities on the coulombic efficiency are due to the carbon utilized. As shown in Figure 36, the only cells with unstable coulombic efficiency outputs, were the ones harboring carbon-coated separators with 5 layers of MWCNT, and these show better results than the ones with 10 layers. Therefore, it is plausible to conclude that the increased number of layers of MWCNT on the separator would decrease the coulombic efficiency, when discharged at low current densities.

The significant capacity retention of MWCNT@10L at the first 10 cycles is clearly understood by analyzing the upper plateau discharge capacity. As shown, the upper plateau contribution is as high as 75% on the first cycles. SC@10L also shows an increased upper plateau contribution of 85% at the first cycle, although the decay is more pronounced at the following cycles, decreasing to 61% at the tenth cycle. KB@10L shows a high upper plateau contribution of 80%, however, at the following cycles a fast decay is reported, achieving at the tenth cycle the same upper plateau contribution as the cell with pristine separator, 40%. At a current density of 1.27 mA cm^{-2}, MWCNT@10L shows the highest upper plateau contribution along the other carbons, although a decline is observed. SC@10L, on the other hand, shows a wide decrease of upper plateau contribution, while KB@10L shows no development in terms of upper plateau contribution. At higher current densities, the upper plateau discharge capacities decrease even further, achieving their minimal values at 3.82 mA cm^{-2}. When cycled again at 0.64 mA cm^{-2}, the upper plateau contributions of cells with MWCNT@10L and SC@10L show an increase followed by a steady decline. At the ninetieth cycle, cells with pristine separator and carbon-coated separator with KB@10L, SC@10L and MWCNT@10L show upper plateau capacities of 37%, 38%, 44% and 55%, respectively.

From the lower plateau discharge capacity, it is reported enhancements of the reduction potential for all cells with carbon-coated separators, except KB@10L. When discharged at a current density of 0.64 mA cm^{-2}, MWCNT@10L show sudden increases and decreases of lower plateau contributions, varying always between 50%. SC@10L and KB@10L, on the other hand, show increased lower plateau contributions at the first cycle but decay with further cycling. SC@10L decays until a certain level and maintains the same values, while KB@10L steadily decreases, achieving at the tenth cycle the same lower plateau contribution as the cell with pristine separator. At higher current densities, MWCNT@10L show superior capacity outputs, compared with the other carbon-coated separators, although at 3.82 mA cm^{-2}, the values are approximately the same as the ones from SC@10L. With

decrease of current density, the lower plateau discharge capacity increases and maintains an average value of 50%. SC@10L also demonstrates an increase of lower plateau discharge capacity, when compared to the cells with 1 and 5 layers of this carbon, although lower than cells with MWCNT@10L. On the other hand, cells with KB@10L show no significant improvement in terms of lower plateau discharge capacity at the first seventy cycles, but an improvement is reported on the last cycles.

From the analysis of the rate cyclability in Figure 37, it was concluded that the introduction of 10 layers of MWCNT on the separator brought significant capacity enhancements to the cells, evidenced by the superior capacity at the first cycle, the disappearance of the fast capacity decay on the following cycles, and high rate capabilities. This confirms that coatings of MWCNT provided an efficient trapping of the polysulfides and further improved the reduction potential of these species at the end of discharge. Carbon-coated separators of SC@10L also provided enhancements to the cells performance, although less than cells with carbon-coated separators of MWCNT@10L. Even though the highest first discharge capacity was provided by these cells, a decrease of capacity was observed at the following cycles, evidencing lower polysulfide trapping capabilities when compared to cells of MWCNT@10L. Cells of KB@10L showed the worst results in terms of performance enhancement. This is evidenced by the fast capacity decay at the first cycles, and lowest capacity outputs at different current densities.

The enhancement in capacity provided by each coating, could be explained according to their physicochemical properties. Chang *et al*. and Chung *et al*. [8, 111], suggested that the main factors for blocking the freely migrating polysulfides and for subsequently trapping the dissolved polysulfides are, respectively, the high amount of micropores and high pore volume that create good tortuosity for the polysulfide flux and the small micropores that effectively filter out the dissolved polysulfides species. Moreover, carbon materials with high surface areas provide a more accessible reaction area for reactivating the trapped active materials. Allied to a high surface area, high electrical conductivities are also required to facilitate the electron transport, reactivating and converting the trapped redox intermediates. Regarding these findings, in future works, a full characterization of the carbon coatings should be performed to link with the electrochemical performance enhancement.

The rate cyclabilities obtained in this work, were then compared with the ones reported by Kim *et al*. [103], as shown in Figure 38. The analysis was performed solely between the first and tenth cycle since in this range a significant decrease of capacity is typically observed, due to the loss of active material in the form of soluble species. Therefore, high capacity retentions demonstrate efficient trapping abilities of the functionalized separators, while low capacity retentions implicate inferior polysulfide confining capabilities.

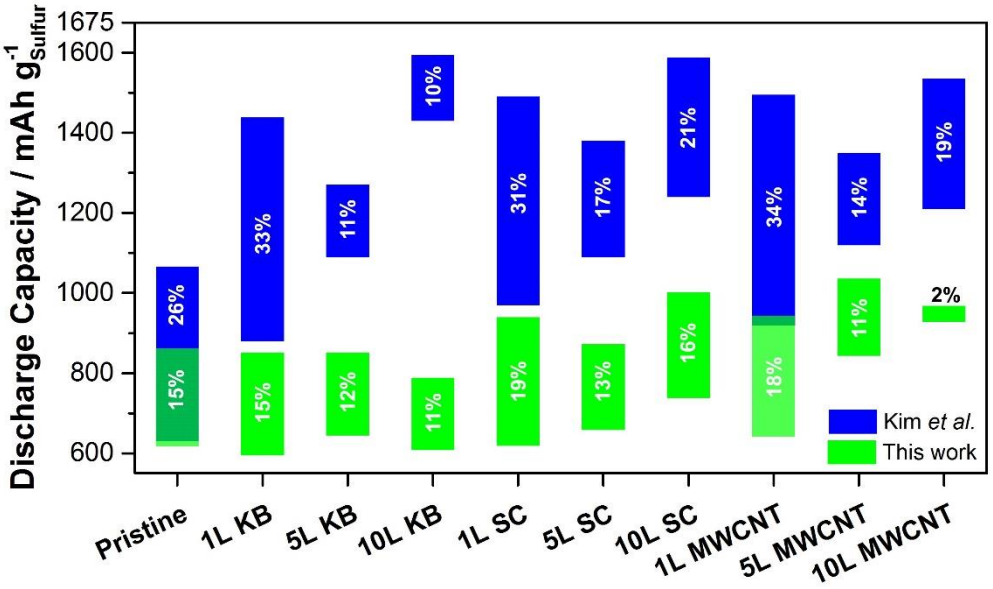

Figure 38 - Comparison of discharge capacities at the first and tenth cycles, of cells employing multi-layered carbon-coated separators, reported by Kim *et al.* [103] and the ones obtained in this work. The top of each bar represents the first discharge capacity, and above is evidenced the discharge capacity at the tenth cycle. The decrease of capacity, in percentage, is evidenced in the bars. The lower axis represents the carbon coating utilized, and the left axis shows the discharge capacity of the cell. The blue and green colored bars represent the results reported by Kim *et al.* and in this work, respectively.

As shown in Figure 38, the discharge capacities reported by Kim *et al*. are much higher than the ones obtained in this work. The disparity in discharge capacities is mainly due to the cathodes composition and electrolyte/sulfur ratios.

Cathodes with high sulfur loading and content suffer from lower electric and ionic conductivities [112, 113, 114]. Sulfur is regarded as an electric insulating material, and high contents of sulfur on the cathode lead to a decrease of the overall electric conductivity, thus lowering the electrochemical performance. Cathodes with high sulfur loadings are typically thick. Thick cathodes hinder the penetration of the electrolyte in the core of the cathode, decreasing the Li^+ penetration, thus reducing the active material utilization. Since the cathodes used by the authors show lower sulfur loadings and content, 0.5-0.55 mg cm^{-2} and 50 wt.%, compared to the high sulfur loading cathodes used in this work, 4.25 mg cm^{-2} and 60 wt.%, it is expected a difference in capacity outputs.

Regarding the amount of electrolyte, low quantities could lead the cell's failure since continued lithium deposition and dissolution during charge and discharge, lead to the continuous formation of a new SEI through the consumption of the electrolyte components. This process worsens at high sulfur loadings, since more lithium will be utilized to react with sulfur [115]. In this regard, excess of electrolyte is used to maintain a margin of safety, although, it results in the decrease of the cells specific energy and energy density. The electrolyte/sulfur ratio used by Kim *et al*. and in this work were 80:1 and 9:1, respectively. Therefore, it would be expected that the cycling performances reported by Kim *et al.*, would be significantly higher than the ones reported in this work.

Regardless of the discrepancy between the discharge capacity outputs, the effect on the capacity, due to the carbon material used, and the number of layers deposited on the separator, is clearly evidenced - cells harboring coated separators with multiple layers achieved superior initial discharge capacities and higher capacity retentions. However, some differences could be noted. The electrochemical results reported by Kim *et al.* showed superior cycling performances on cells with separators coated with KB, while in this work, cells with KB demonstrated the worst cycling performance. On the other hand, cells with carbon-coated separators of MWCNT produced in this work, achieved the best results in terms of capacity retention - an impressive decrease of capacity of only 2% was reported from cells employing carbon-coated separators with 10 layers of MWCNT.

A possible explanation for the negligible performance enhancement provided by the carbon-coated separators of KB used in this work could be the coating procedure adopted. Recalling the SEM micrographs showed in section 4.2, carbon-coated separators with KB and SC revealed successive interspaces between the aggregates, which could decrease the tortuosity upon the movement of the soluble lithium polysulfide species, thus enabling the loss of the active material from the cathode, in the form of soluble species. On the other hand, the net-like entangled crisscrossed nanotubes, observed on the MWCNT coated separators, showed no interspaces, and consequently, higher tortuosity could be expected. In this regard, the tortuosity obtained from the different functionalized separators is intimately linked with the coating method.

4.4. Electrochemical performance of cells without additive $LiNO_3$

After investigating the performance enhancement provided by the introduction of multi-layered carbon-coated separators on Li-S cells, it was concluded that some carbons contributed better to the improvement of the capacity than others. Moreover, this improvement was also found to greatly depend on the number of deposited layers. Since separators coated with 10 layers of MWCNT provided the best improvements in terms of polysulfide retention and increased reduction potential of the insulating intermediates, further investigations were performed to understand the efficiency of the polysulfide trapping capabilities of these separators through galvanostatic cycling of cells with electrolyte E2. In the electrolyte E2, contrary to electrolyte E1, $LiNO_3$ salts were not added. Therefore, no protective passivation layer against the polysulfides was built at the lithium anodes surface, allowing the shuttling of polysulfides.

In Figure 39 are shown the charge/discharge voltage profiles of cells, cycled at 0.64 mA cm^{-2}, with separators coated with 10 layers of MWCNT, using the electrolytes E1 and E2. For comparison, the voltage profiles of cells with a pristine separator are also shown. At the first cycle, the cell with pristine separator, employing the electrolyte E1 (Pristine@E1), shows the characteristic discharge curve of a Li-S cell, identified by the two plateaus – the upper plateau, ranging between 2.4-2.3 V, and the lower plateau, between 2.1-2.0 V. Moreover, it reports a high first discharge capacity of 971 mAh g^{-1} (58%). In the charge process, two plateaus can also be identified, at 2.2 V, the lower plateau, and 2.4 V, which corresponds to the upper plateau. With further cycling, the discharge capacity rapidly fades to 618 mAh g^{-1} (37%) at the fifth cycle, followed by a shrinkage of the plateaus. The cell MWCNT@E1, also demonstrates a superior first discharge capacity, 965 mAh g^{-1} (58%), but contrary to the cell Pristine@E1, a high capacity retention on the following cycles is observed, evidenced by the overlapping discharge curves. Therefore, it was demonstrated that the introduction of a carbon-coated separator of 10 layers of MWCNT greatly enhanced the cell performance. In the

fifth cycle, the cell demonstrates a discharge capacity of 917 (55%) mAh g^{-1}, which corresponds to a decrease of 2% of the initial discharge capacity.

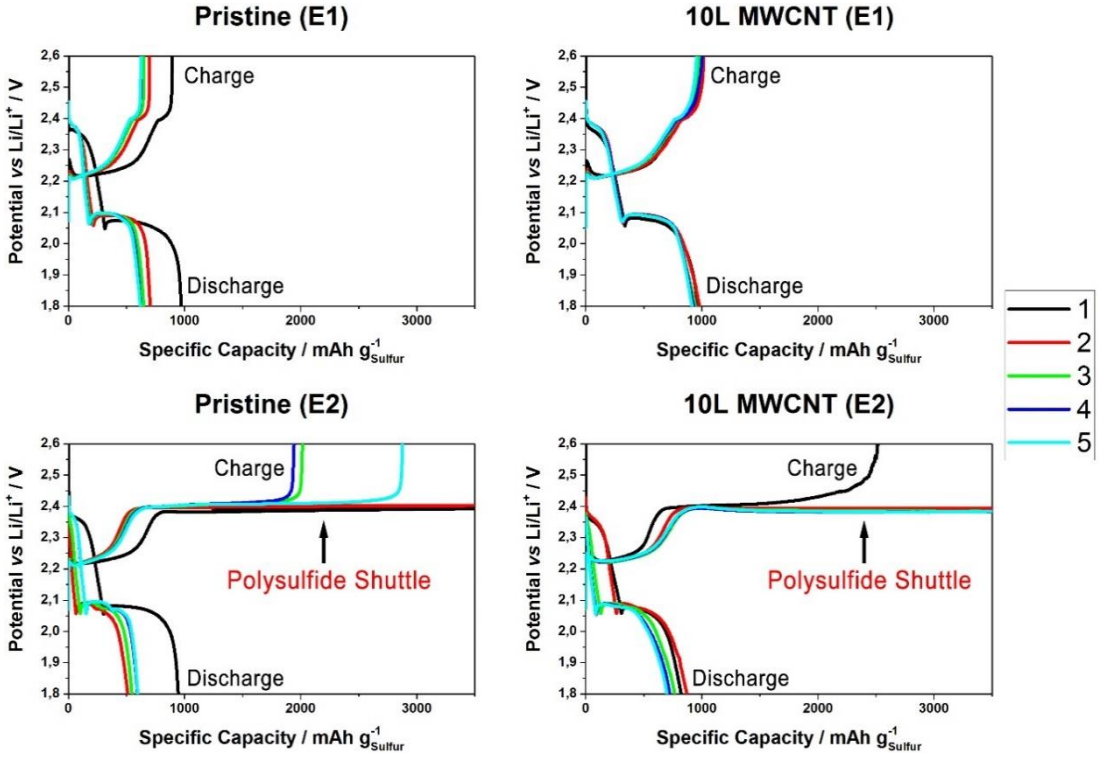

Figure 39 - Electrochemical performance of cells with pristine separator and carbon-coated separator of MWCNT with 10 layers. The cells were cycled at 0.64 mA cm^{-2}, using electrolyte E1 and E2. At the top of each chart, are shown the separators utilized and the electrolyte employed. On the left axis is the potential, and on the lower axis is the specific capacity of the cell. The color of the lines represents the cycle number.

Cells employing the electrolyte E2 already demonstrate changes on the charge regime, compared to cells with electrolyte E1. The cell Pristine@E2 shows a high first discharge capacity of 945 (56%) mAh g^{-1}, followed by a charge capacity far higher than the discharge capacity. With further cycling, the charging regime maintains its unstable behavior, showing increases and decreases of capacity. As discussed in section 2.4.1, the polysulfide shuttle produces parasitic current, which does not contribute to the charging of the current. Here, the shuttle effect is evidenced by the long upper charging plateau. In the following cycles, the discharge capacities decrease, reporting a discharge capacity of 597 (36%) mAh g^{-1} at the fifth cycle. Regarding the cell MWCNT@E2, the first discharge capacity is 822 (49%) mAh g^{-1}, lower than in the previous cells, and at charging, it is also evidenced a long upper plateau, although, a lower capacity value was obtained in this first cycle compared to the cell Pristine@E2. Nevertheless, with further cycling, the reported charging capacities achieve high values. This analysis demonstrated that even with the best carbon-coated separator, the full trapping of the polysulfides was not achieved. Even though the shuttling of polysulfides remains, a pronounced capacity retention is observed. The capacity at the final cycle is 700 (42%) mAh g^{-1}, corresponding to a capacity decrease of 7%. Interestingly, analyzing the plateaus contribution of the cell MWCNT@E2, a wide decrease of the upper plateau is observed, but compensated with the increase of lower plateau. The shrinkage of the upper plateau was also detected in the cell Pristine@E2, although, the compensation of capacity loss by an increase of lower plateau discharge capacity was not observed.

According to these results, it is plausible to conclude that the presence of the carbon coating allowed the preservation of the capacity, identified by the overlap of discharge curves. Nevertheless, the shuttle of the polysulfides was reported, which indicates that polysulfides still migrate out of the carbon layer. A proper explanation for the incomplete confinement of the polysulfides is fundamentally due to the nonpolarity of carbon materials, which are incapable of immobilizing polar

polysulfides. Although the weak physical interaction could suppress the diffusion of polysulfides in the short-term, the polysulfides may eventually diffuse out of the carbon layer to the anode

Since polysulfides are intrinsically polar, effective strategies to efficiently confine these species would be through chemical interactions, by the functionalization of the carbon materials with compounds which chemically adsorb polysulfides [116], rather than solely relying on the high surface area or pore structure. Therefore, a rational integration of polymers, oxides and carbon materials, can effectively help suppressing the polysulfides diffusion, improve the cathodes conductive network and eventually help to stabilize the lithium anode.

4.5. SEM investigations

After analyzing galvanostatically cells employing the best-performing carbon-coated separator without the additive $LiNO_3$, it was demonstrated that polysulfides still migrated through the carbon coating, although a capacity retention was observed. Therefore, to further investigate possible explanations for the capacity retention offered by the carbon-coated separator, SEM investigations were conducted on the surface of cycled metallic lithium anodes, from cells with pristine separator and carbon-coated separator of MWCNT with 10 layers, employing electrolyte E2. For comparison, SEM micrographs of an uncycled metallic lithium disk were introduced here.

In Figure 40 are shown SEM investigations performed on the surface of a pristine metallic lithium. From the SE imaging, a smooth surface is observed with a defined pattern of parallel lines. BSE investigations show a similar contrast all over the analyzed surface of the metal, although some particular sites, identified by wither spots, suggest that other elements, other than lithium, are present on the surface. This is also supported from the defined carbon signals, which are overlapped with the high intensity spots from the BSE analysis. From this point of view, it is plausible to state that the particles are carbon-related, which might be dust or residual substances transposed onto the metal while it was prepared for the analysis. High oxygen signals are observed, which could have their source from the reaction with the oxygen molecules present in the air. Moreover, weak and homogeneously distributed fluorine and sulfur signals were also detected, suggesting that upon the preparation of the sample, the metallic lithium promptly reacted with the particles close to it.

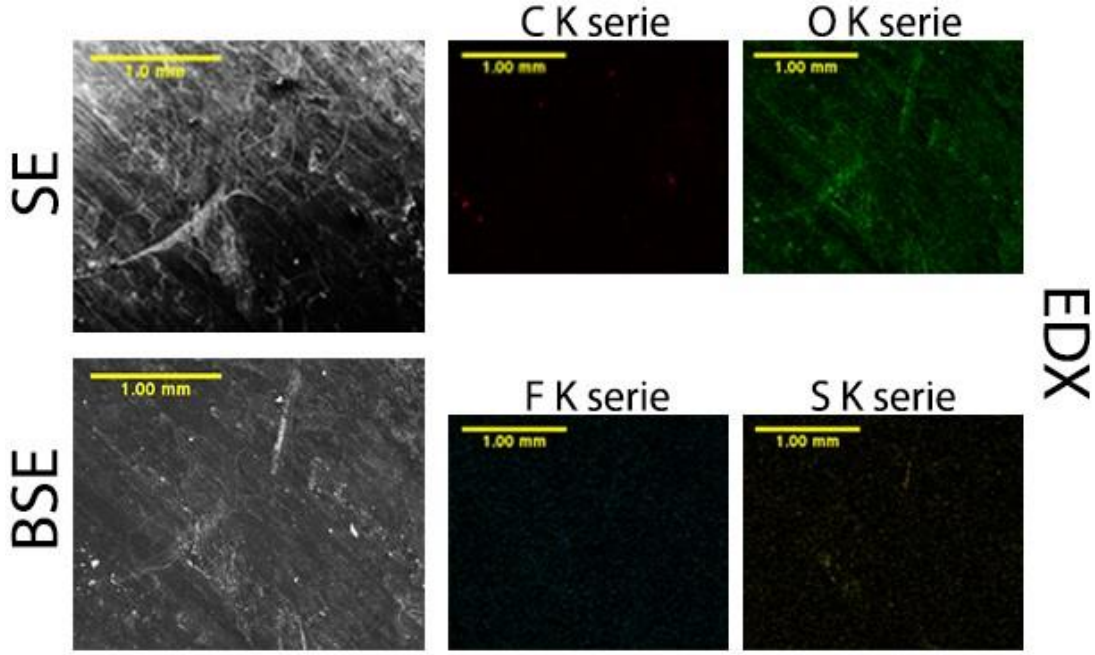

Figure 40 – SEM micrographs of fresh metallic lithium. SE imaging and BSE analysis are shown on the right, and the elemental tracking of carbon (C), oxygen (O), fluorine (F), and sulfur (S), on the left.

Further on, regarding the cycled anodes, the SEM investigations and galvanostatic data are reported and discussed. The cycling performance of the two cycled cells was introduced in this section to link with the SEM investigations performed. Figure 41 shows the electrochemical performance of the two cells, and similar results reported on the previous section were also obtained here. The cell with pristine separator reports a high first discharge capacity, 947 mAh g^{-1} (57%), but with further cycling, the capacity rapidly decreases, due to the loss of active material into the electrolyte, as soluble polysulfides. At the fifth cycle, the reported discharge capacity is 597 mAh g^{-1} (36%), 21% decrease compared to the first discharge capacity. Regarding the charging process, higher capacities are also reported, evidencing the shuttle of the polysulfides. The cell with the carbon-coated separator shows a lower first discharged capacity, compared to the cell with pristine separator, 824 mAh g^{-1} (49%), although, a retention of capacity was observed over the following cycles. At the last cycle, the reported discharge capacity is 701 mAh g^{-1} (42%), 7% lower than the first discharge capacity. Analyzing the charging process, a first unstable charging is observed, and with further cycling, the charging capacities achieve high values. Therefore, even with the best performing carbon-coating, the shuttle of lithium polysulfides was not suppressed, although, a retention of capacity was observed.

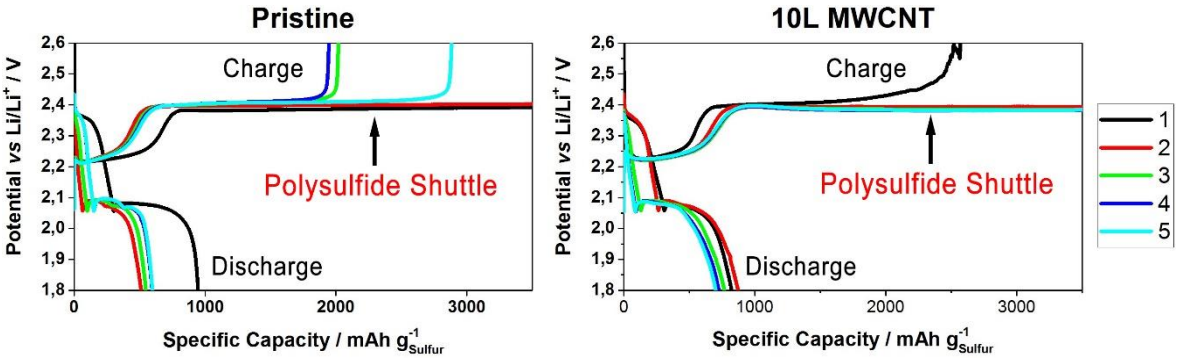

Figure 41 - Electrochemical performance of cells with pristine separator and carbon-coated separator of MWCNT with 10 layers. Cells cycled at 0.64 mA cm^{-2}, with electrolyte E2. Colored lines correspond the cycle number.

After cycling, the cells were disassembled, and the anodes were retrieved to further analyze through SEM. The following group of SEM micrographs, reported in Figure 42, are related to the cycled anode retrieved from the cell with pristine separator. The SE mapping shows a rather heterogeneous surface, compared to the uncycled anode. The clean surface of the pristine metallic lithium is now covered with complex composites, and some agglomerates can be already identified. The BSE signals confirm the hypothesis of a chemically heterogeneous surface, demonstrated by the different intensities observed on the analyzed area. The agglomerate-like compounds show higher intensities, suggesting that these species have higher atomic numbers that the ones around. Regarding the elemental mapping, the carbon, oxygen and fluorine signals are present all over the analyzed surface. This indicates that the lithium formed a SEI, through the consumption of the species present in the electrolyte. Such results were also reported by Aurbach *et al*. [37], which described the contributions of the various components present in the electrolyte, such as DOL, LiTFSI and lithium polysulfides, to the surface chemistry of metallic lithium. DOL promptly reacts with lithium, resulting in the ring-opening reaction and further formation of surface species, such as ROLi, HCO_2Li and poly-DOL oligomers. In DOL/LiTFSI solutions, the surface chemistry of the metallic lithium is dominated by the reduction of the anion species, hence, species containing C-F, S-O, and S=O bonds could also be found. Strong sulfur signals were also reported here, and are more pronounced on the agglomerates spotted in the BSE investigations. Therefore, it can be concluded that sulfur related species were deposited on the surface of the metallic lithium, probably Li_2S, due to the reaction of dissolved polysulfides with the lithium anode. The presence of sulfur-related species on the lithium surface is in conformity with the cycling performance of the cell with a pristine separator, demonstrated in

Figure 41. Since the polysulfide shuttling occurred, evidenced by the long charging period, it was expected to find sulfur compounds on the lithium surface.

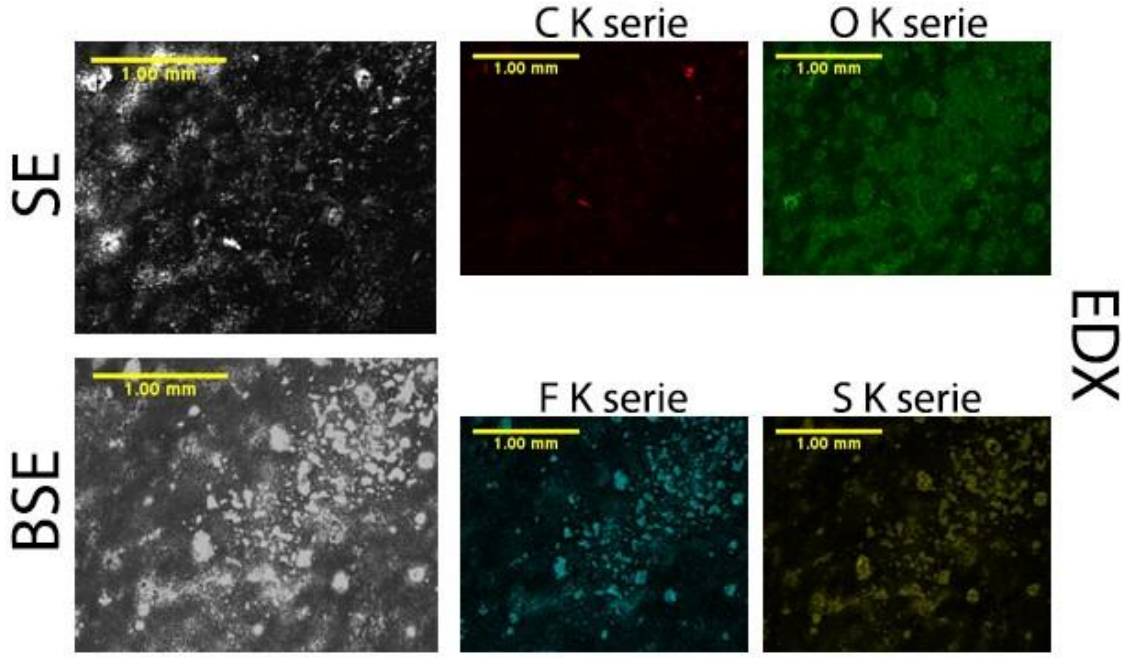

Figure 42 - SEM micrographs of cycled metallic lithium, from cell employing pristine separator. SE imaging and BSE analysis are shown on the right, and the elemental tracking of carbon (C), oxygen (O), fluorine (F), and sulfur (S), on the left.

Figure 43 shows the SEM investigations performed on the cycled metallic lithium retrieved from the cell employing the separator coated with 10 layers of MWCNT. At a first look, the SE mapping shows an irregular corroded surface of the metallic lithium, with abundant damaged zones. Moreover, different surface species can also be detected from the different intensities in the BSE analysis. Regarding the elemental mapping, strong carbon, oxygen and fluorine signals were observed, which indicates that a passivation layer was formed on top of the metallic lithium surface. The sulfur signals are also strong, and similarly to the previous analysis, these are overlapped with the zones with the higher intensities in the BSE, thus it can be concluded that these species could be Li_2S agglomerates formed through the shuttle reaction, evidenced in Figure 41.

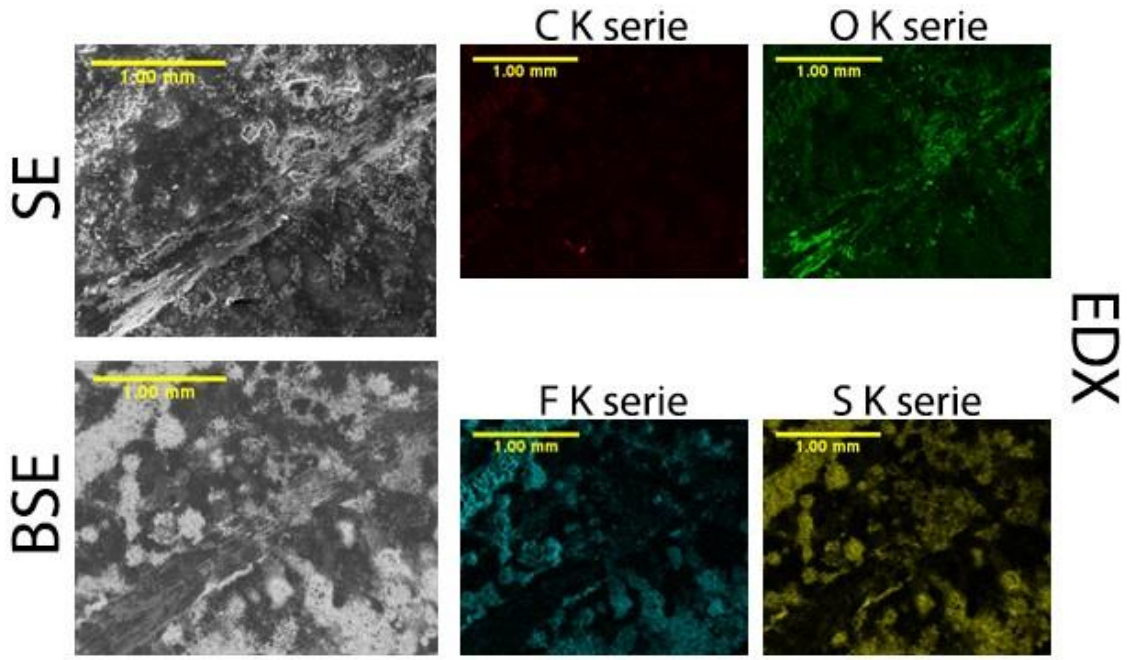

Figure 43 - SEM micrographs of cycled metallic lithium, from cell employing separator coated with 10 layers of MWCNT. SE imaging and BSE analysis are shown on the right, and the elemental tracking of carbon (C), oxygen (O), fluorine (F), and sulfur (S), on the left.

Nevertheless, SEM analysis should not be restrained into a single spot, nor at high magnifications, the full sample should be analyzed to find proper justifications to the augmented capacity retention reported by the introduction of the best-performing carbon-coated separator. In this regard, the previous elemental mappings were added and marked in a larger SE image, to identify the analyzed areas, as shown in Figure 44.

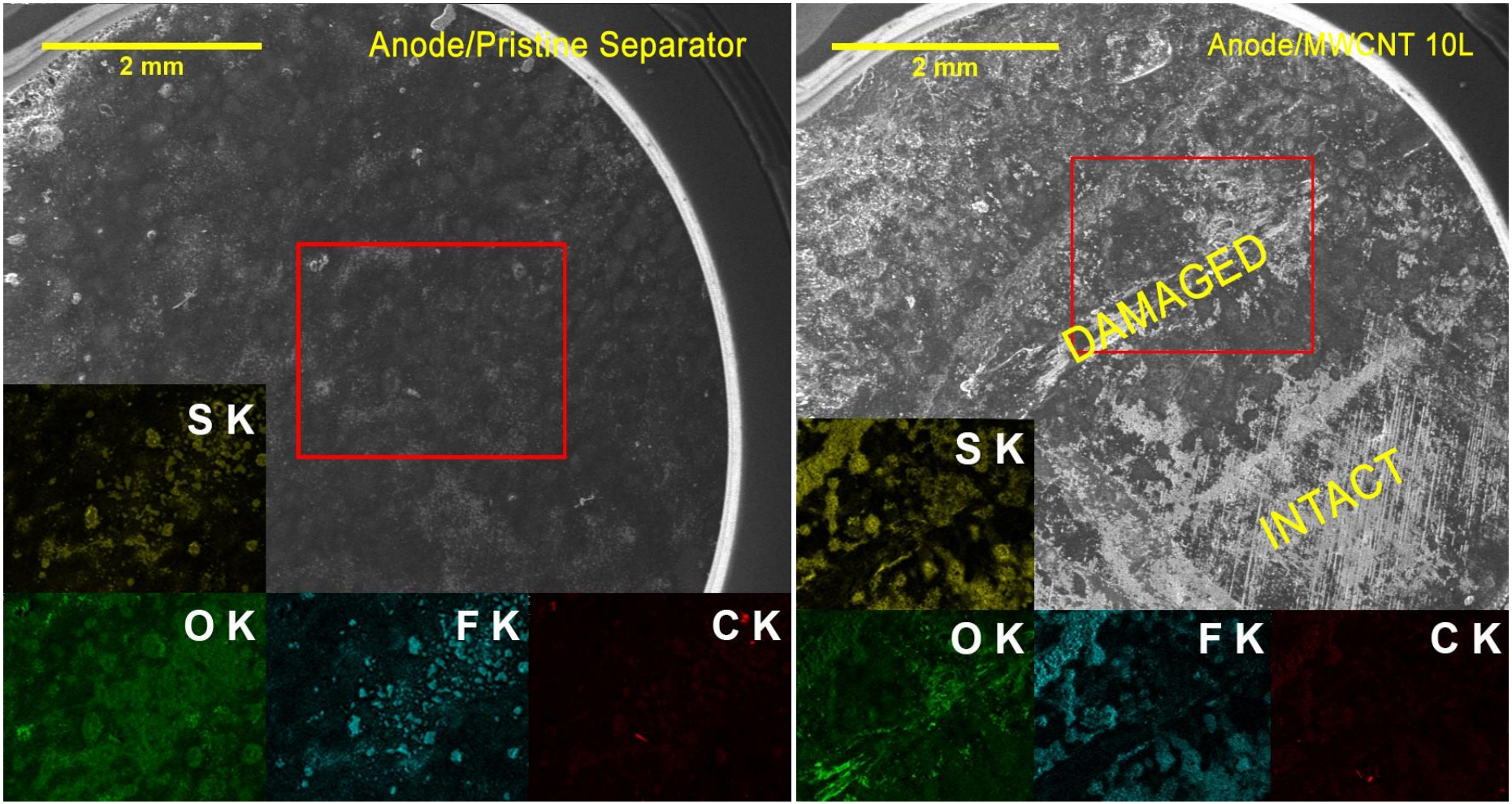

Figure 44 - SEM micrographs of cycled metallic lithium anodes from cell with pristine separator (right) and separator coated with 10 layers of MWCNT (left).

The SE image of the cycled lithium anode, retrieved from the cell employing the pristine separator, shows a fully covered surface. As discussed before, sulfur-related compounds were detected by the overlap of the sulfur signals and the BSE mapping. Therefore, it is expected that certain zones of the cycled anode are also covered with lithium sulfide aggregates. Regarding the SE image of the cycled lithium anode, recovered from the cell harboring the carbon-coated separator with 10 layers of MWCNT, two distinct zones can be identified – the upper part, which shows an extremely damaged surface, and the lower part, that seems much less corroded, and even shows the smooth linear pattern identified on the uncycled anode SEM micrographs (see Figure 40). Recalling the electrochemical performance of this cell, it was found that high shuttling of polysulfides occurred. Since the reactions that comprise the shuttling promote the corrosion of the lithium anode, it is not surprising that the surface of the anode shows a damaged appearance. Nevertheless, a portion of the anode seemed intact, with the patterns identified in the pristine metallic lithium. This could be due to the effective retention of the soluble polysulfides on that specific zone of the carbon layer, which could also explain the capacity retention observed on the cycling performance demonstrated by the cell.

4.6. Influence of the manufacturing process on the cathodes structure

Additional investigations were conducted on different compositions of Li_2S cathodes. As described in section 3.2, the cathodes were produced through a heat-pressing method, in the absence of any solvent. The cathode formulations consisted of pristine or core-shell Li_2S particles, carbon additive Ketjenblack, and as binders PVP or PEO.

Issues regarding the mechanical failure of the cathode film were observed, translated by the loss of material. After retrieving the heat-pressed cathodes from the stainless steel template, the peeling of the top surface was observed. Moreover, additional loss of material, due to the attachment of the cathode film to the heat-resistant polymer layer, was observed. Higher deterioration of the cathode structure was evidenced in heat-pressed cathodes containing pristine Li_2S particles while cathodes comprised of core-shelled Li_2S particles demonstrated better structural integrity. Such results were also reported by Ding *et al*. [112], where high loading cathodes integrating carbon blacks with high surface areas were particularly brittle and easily peeled of the current collector. Nevertheless, the situation could be solved by replacing carbon black with conductive fine graphite powders. Regarding the superior structural integrity of the cathodes containing carbon-coated Li_2S particles, it is believed that the core-shell structures could work as the component necessary to increase the cohesion between the particles, avoiding the addition of other carbon materials.

4.7. Electrochemical performance of cells with Li_2S as cathode material

Here, rate cyclability examinations are presented with respect to cells with different cathode formulations, employing electrolyte E1.

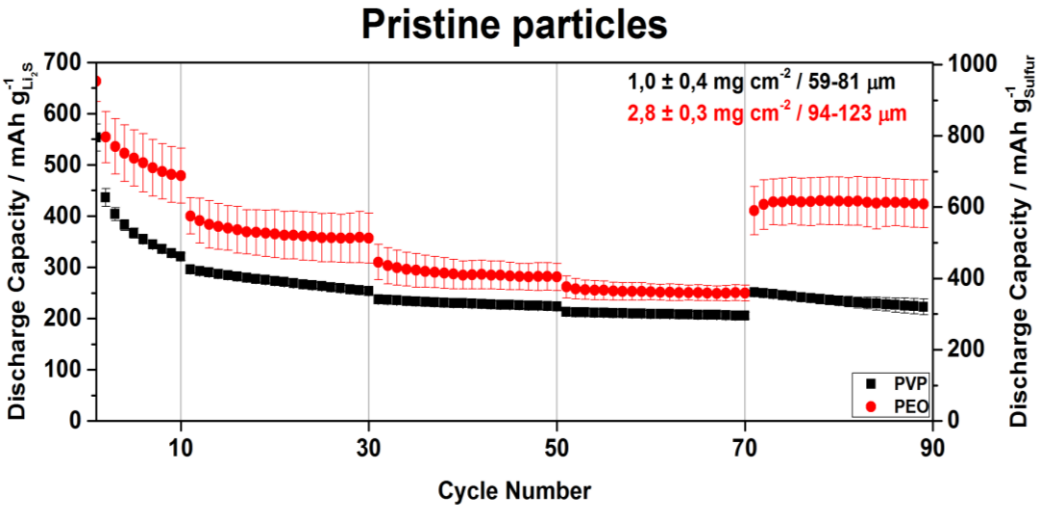

Figure 45 - Electrochemical performance of cells with cathodes composed of pristine Li_2S particles, with different binders. PVP corresponds to (■) and PEO (●). The left and right axis represent the discharge capacity with respect to the mass of Li_2S and sulfur, respectively, and above are represented the cycle number. On the top left corner of each chart are listed the average Li_2S loadings, and the thickness range of the cathodes analyzed.

Figure 45 shows the electrochemical performance of cells employing cathodes with pristine Li_2S particles, with different binder mixtures. It is immediately apparent that cells employing PEO report significant advantages compared to the other cathode formulations. Moreover, higher Li_2S loadings and thicker cathodes were obtained using PEO as binder material.

Cells with PEO reported the highest first discharge capacity, 663 mAh g^{-1}, and at the tenth cycle it demonstrates a discharge capacity of 479 mAh g^{-1}, which corresponds to a decrease of 15% from the

initial discharge output. When cycled at higher current densities, the cells still achieve better results compared to the other cells, and when discharged again at 0.64 mAh g^{-1}, stable capacity outputs were obtained, ranging in the 426 mAh g^{-1}.

Cathode formulations with PVP showed the lowest Li_2S loadings and thicknesses. As first discharge capacity, 553 mAh g^{-1} was obtained, and with further cycling the capacity rapidly fades, achieving at the tenth cycle 320 mAh g^{-1}, a decrease of 20% of the first discharge capacity. At higher discharging rates, a slight decrease of capacity is observed. When discharged again at 0.64 mAh g^{-1}, a decrease of capacity is observed, achieving a discharge capacity of 223 mAh g^{-1} on the last cycle.

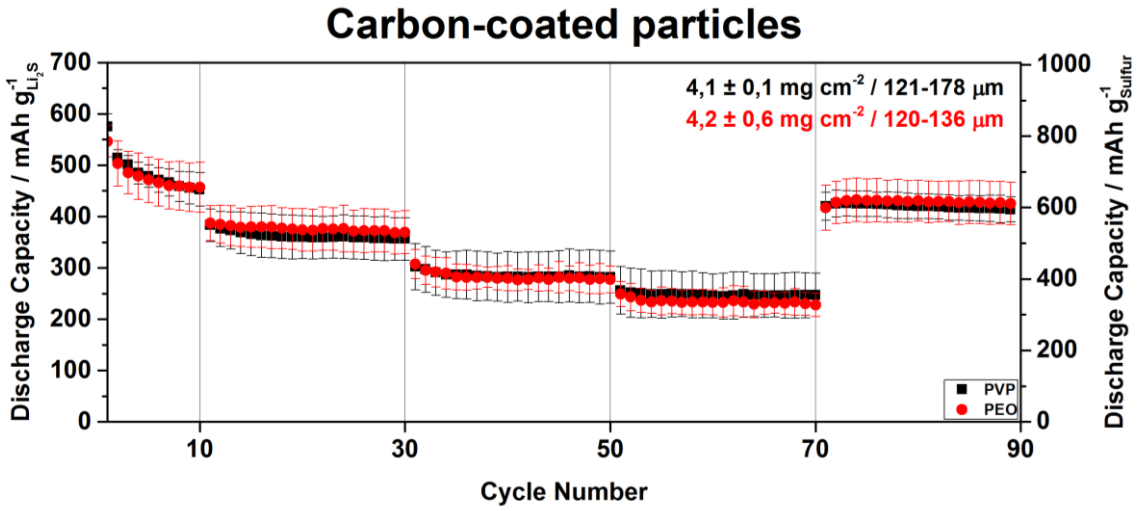

Figure 46 - Electrochemical performance of cells with carbon-coated Li_2S particles, with different binders. PVP corresponds to (■) and PEO (●). The left and right axis represent the discharge capacity with respect to the mass of Li_2S and sulfur, respectively, and above are represented the cycle number. On the top left corner of each chart are listed the average Li_2S loadings, and the thickness range of the cathodes analyzed

Figure 46 demonstrates the electrochemical performance of cells employing cathodes of core-shelled Li_2S particles, with different electrode compositions. Better rate capabilities and cycling performances were achieved by using carbon-coated Li_2S particles instead of pristine Li_2S particles. Moreover, a lower decrease of capacity on the first cycles was observed, evidencing superior polysulfide trapping. Since a carbon film covers the Li_2S surface, it is believed that an increase in electric conductivity is provided, enabling higher active material utilizations. Furthermore, the carbon-shell structure could enhance the encapsulation of the lithium polysulfides, while allowing the flow of Li^+ through the structure [56]. Moreover, higher Li_2S loadings were reported, compared to the previous study, probably due to an increased binding effect between the cathode components due to the carbon-coating involving the Li_2S particles. It is noteworthy that despite higher Li_2S loadings were obtained, enhanced electrochemical utilizations remained.

As shown, cells with PVP and PEO show similar capacity outputs. Cells employing PVP demonstrate the highest first discharge capacity, 575 mAh g^{-1} and at the tenth cycle it shows a discharge capacity of 453 mAh g^{-1}, representing a 10% decrease of the initial discharge capacity. When cycled at higher current densities, a decrease of capacity is observed, although stable capacity outputs are reported. When the current density returns to 0.64 mA cm^{-2}, a stable capacity output is observed, ranging 420 mAh g^{-1}.

Cells with PEO show a first discharge capacity of 546 mAh g^{-1}, and at the 10^{th} cycle it reports a capacity output of 457 mAh g^{-1}, which corresponds to a decrease of 8% of the initial capacity. When discharged at higher rates, the capacity output decreases, although with minimal losses of reversible capacity. When cycled again at the initial current density, 0.64 mA cm^{-2}, a stable capacity is obtained, with the values ranging 428 mAh g^{-1}.

Comparing the cycling performances obtained in both graphs, it was verified that the presence of a carbon-coating on the Li_2S surface deeply affected the specific capacity of cells employing PVP. Although similar initial discharge capacities were obtained, a rapid decay of capacity was evidenced in the first cycles of cathodes employing pristine Li_2S particles, while cells containing core-shelled Li_2S particles reported a moderate decrease of capacity. In contrast, cathodes with PEO demonstrate similar cycling performances, however in cathodes with pristine Li_2S particles it was observed higher losses of capacity on the initial cycles. These findings further support the hypothesis that the core-shell structure amplifies the confinement of the lithium polysulfides while permitting the movement of Li^+.

Chapter 5 – Conclusion and Future Outlook

Functionalized separators with different carbon materials were produced, exploiting a variant of the Langmuir-Blodgett technique. The coating method, known as Langmuir-Blodgett Scooping, was first developed by Kim *et al.* and further explored in this work. It was found that the main parameters that influenced the quality of the carbon films - concentration and level of dispersion of the carbon particles, and flow rate of suspension -, played a crucial role in the stability and homogeneity of the produced carbon-coatings. Low concentration of nanoparticles and ideally dispersed suspensions are preferred, while high concentration and poorly dispersed carbon nanoparticles resulted in the transposition of carbon clusters onto the film, which negatively influenced the homogeneity and stability of the film. Steady flow rates are also desired since discontinued injection of suspension on the water surface lead to defective LB films and loss of nanomaterial into the subphase. These improvements allowed the conceiving of thin and low weight multi-layered carbon coatings. Carbon coatings of MWCNT showed the lowest values of loading and thickness, followed by KB and SC. Moreover, the LBS process permitted the coating of the separator in a fraction of seconds, while methods such as vacuum-filtration and tape-casting require longer periods, ranging from minutes to hours.

The produced carbon-coated separators were introduced in Li-S cells to understand the enhancing effects in the electrochemistry. It was found that the number of layers and the carbon characteristics strongly influenced the cell behavior. Cells employing carbon-coated separators with one layer of carbon did not show enhancements regarding capacity increase or retention. As demonstrated by SEM of the carbon films, the separator was not fully covered by the carbon film allowing the diffusion of lithium polysulfides through the cell. An increase of capacity was reported for cells with five layers, in particular with MWCNT. When increasing the number of layers to ten, significant improvements were observed. Cells employing carbon-coated separators of MWCNT experienced superior capacity retentions, translated by efficient trapping of the soluble polysulfides, and increased rate capabilities. Carbon coatings of SC also showed enhancements concerning the capacity output, although not as pronounced as MWCNT. On the other hand, carbon-coatings of KB demonstrated the worst developments. These cells showed comparable capacity outputs as cells with the uncoated separator, which contradicts the findings of several research groups [9, 103]. A possible explanation for the low performance of separators coated with KB resides on the low tortuosity obtained. As evidenced by the high magnification SEM investigations on the carbon layers of KB, interspaces between the carbon clusters were detected, which could open paths for the free movement of the polysulfides outside the cathodes region, promoting the loss of capacity. A full characterization of the carbon coatings should thus be performed to link with the electrochemical performance enhancement. The characterization should comprise the measurement of the effective electrical resistivity, surface area distribution, pore size and volume distributions, through a four-point probe method, Brunauer-Emmett-Teller (BET), and Barrett-Joyner-Halenda (BJH) analysis, respectively. Such parameters are important to analyze since the trapping capabilities and further electrochemical utilization of polysulfides are strongly dependent on the characteristic of the carbon film's physical structure. Moreover, other electrochemical techniques could be adopted in future works, such as electrochemical impedance spectroscopy (EIS) methods, which determine several important parameters, such as the electrolyte resistance, charge transfer resistance of the cathode and the Li^+ diffusion into the bulk of the cathode. Understanding the magnitude of each parameter further clarifies the effect of the carbon-coatings on the electrochemical performance.

The trapping effect provided by the best performing carbon-coated separator, separators coated with 10 layers of MWCNT, was also analyzed. The galvanostatic investigations were carried out employing an electrolyte without the additive $LiNO_3$, which would produce a passivation layer on the lithium anode that ceases the shuttling of polysulfides. It was observed that even with the best-performing carbon coating, the shuttle effect was not inhibited, concluding that soluble polysulfides still escaped. However, a retention of capacity was observed, demonstrating that lithium polysulfides were trapped on the carbon film and were electrochemically accessible.

Through SEM, morphological and elemental investigations were performed on retrieved anodes from cycled cells employing a pristine separator and separator coated with 10 layers of MWCNT. It was found that sulfur aggregates were formed on the surface of the lithium anodes, which was in agreement with the cycling performance of the cells. Moreover, pronounced surface deterioration was observed on the cycled anode retrieved from the cell employing the best performing carbon-coated separator. Nevertheless, unaffected zones on the metallic lithium were also detected, which could indicate that certain regions of the carbon film efficiently trapped the polysulfides. A suggestion is that further SEM examinations of the cycled anodes should cover all the anode's surface, to identify the magnitude of corrosion occurred during the cycling. Moreover, the cathode surface could also be investigated through SEM, to search for possible Li_2S aggregates formed at the surface.

In summary, separators coated with MWCNT demonstrated superior polysulfide retention and electrochemical utilization, followed by SC and KB. Such claims are strongly evidenced by the examinations performed, but further improvements are needed. The polysulfide shuttling was not avoided and, consequently, loss of capacity was reported. Nevertheless, the results are quite satisfactory since outstanding capacity retentions were obtained for cells employing coated separators with 10 layers of MWCNT. The results in the publications are mostly achieved with low electrolyte/sulfur ratios, which result in high capacities but low energy densities. On the other hand, low electrolyte/sulfur ratios result in poorer utilization of active material, thus lower capacities are achieved. Despite the fact that low electrolyte/sulfur ratios were adopted in this work, still considerable capacity outputs were achieved, demonstrating the efficacy of the carbon-coatings of MWCNT. Moreover, it is important to note that the carbon loading of 10 layers of MWCNT is 76% and 29% that to KB and SC, respectively, implying that the MWCNT coating is by far the most efficient of the carbon materials studied. Another important feature regarding the coating technique practiced was the negligible weight gained, which is best appreciated by comparison to literature results where carbons were coated using vacuum filtration or tape-casting methods.

Furthermore, solvent-free Li_2S cathodes were manufactured with a heat-pressing method, and the rate performances investigated. Regarding the formulations adopted, it was found that the cathodes showed poor structural integrity, resulting in major losses of material upon its handling. Nevertheless, cathodes containing core-shelled Li_2S demonstrated rather lower losses of material compared to cathodes comprised of pristine Li_2S, which leads to the assumption that the carbonaceous shell involving the Li_2S particles enhances the cohesion between the different compounds of the cathode.

Concerning the cycling performance of cells employing the Li_2S cathodes, superior results were achieved by using cathodes with carbon-coated Li_2S particles instead of pristine Li_2S particles. The main reason resides on the carbon-shell structure which could block the diffusion of soluble polysulfides, while maintaining the flow of Li^+, and facilitate the active material utilization since carbon materials present high electronic conductivities, thus enhancing the electrochemical kinetics. Furthermore, higher Li_2S loadings, accompanied with better cycling performances, were obtained from cells employing core-shelled Li_2S. Regarding these findings, it is certain that the functionalization of Li_2S particles, by depositing a carbon-layer on the surface, carries improvements in several aspects, such as the interparticle adherence, and cycling performance.

References

[1] D. Larcher and J. M. Tarascon, "Towards greener and more sustainable batteries for electrical energy storage," *Nature Chemistry,* 17 November 2014.

[2] M. Armand and J. -M. Tarascon, "Building better batteries," *Nature,* February 2008.

[3] R. Van Noorden, "Sulfur back in vogue for batteries," *Nature,* 2013.

[4] P. G. Bruce, S. A. Freunberger, J. L. Hardwick and J.-M. Tarascon, "Li-O2 and Li-S batteries with high energy storage," *Nature Materials,* vol. 11, pp. 19-29, 2012.

[5] L. Ma, K. E. Hendrickson, S. Wei and L. A. Acher, "Nanomaterials: Science and applications in the lithium-sulfur battery," *Nano today,* vol. 10, pp. 315-338, 2015.

[6] M. Hagen, D. Hanselmann, K. Ahlbrecht, R. Maça, D. Gerber and J. Tübke, "Lithium-Sulfur Cells: The Gap between the State-of-the-Art and the Requirements for High Energy Battery Cells," *Advanced Energy Materials,* 2015.

[7] J.-Q. Huang, Q. Zhang and F. Wei, "Multi-functional separator/interlayer system for high-stable lithium-sulfur batteries: Progress and prospects," *Energy Storage Materials,* vol. 1, pp. 128-135, 2015.

[8] C.-H. Chang, S.-H. Chung and A. Manthiram, "Effective Stabilization of a High-Loading Sulfur Cathode and a Lithium-Metal Anode in Li-S Batteries Utilizing SWCNT-Modulated Separators," *Small,* vol. 2, pp. 174-179, 2016.

[9] D. Zhao, X. Qian, L. Jin, X. Yang, S. Wang, X. Shen, S. Yao, D. Rao, Y. Zhou and X. Xi, "Separator modified by Ketjen black for enhanced electrochemical performance of lithium-sulfur batteries," *RCS Advances,* vol. 6, pp. 13680-13685, 2016.

[10] S.-H. Chung and A. Manthiram, "Bifunctional Separator with a Light-Weight Carbon-Coating for Dynamically and Statically Stable Lithium-Sulfur Batteries," *Advanced Functional Materials,* vol. 24, pp. 5299-5306, 2014.

[11] H.-J. Peng, D.-W. Wang, J.-Q. Huang, X.-B. Cheng, Z. Yuan, F. Wei and Q. Zhang, " Janus Separator of Polypropylene-Supported Cellular Graphene Framework for Sulfur Cathodes with High Utilization in Lithium–Sulfur Batteries," *Advanced Science,* vol. 3, p. 1500268, 2016.

[12] S.-H. Chung and A. Manthiram, "High-Performance Li-S Batteries with an Ultra-lighweight MWCNT-Coated Separator," *Physical Chemistry Letters,* vol. 5, pp. 1978-1983, 2014.

[13] G. Zhou, L. Li, D.-W. Wang, X.-y. Shan, P. Songfeng and F. Li, "Li–S Batteries: A Flexible Sulfur-Graphene-Polypropylene Separator Integrated Electrode for Advanced Li–S Batteries," *Advanced Materials,* vol. 27, pp. 641-647, 2015.

[14] Y. Son, L. Jung-Soo, Y. Son, J. Ji-Hyun and C. Jaephil, "Recent Advances in Lithium Sulfide Cathode Materials and Their Use in Lithium Sulfur Batteries," *Advanced Energy Materials,* vol. 5, pp. 1500110-1500124, 2015.

[15] S. Meini, R. Elazari, A. Rosenman, A. Garsuch and D. Aurbach, "The use of Redox Mediators for Enhancing Utilization of Li2S Cathodes for Advanced Li-S Battery Systems," *Physical Chemistry Letters*, vol. 5, pp. 915-918, 2014.

[16] K. Pinkwart and J. Tübke, "Thermodynamics and Mechanistics," in *Handbook of Battery Materials*, Weinheim, Wiley-VCH Verlag & Co. KGaA, 2011, pp. 3-26.

[17] D. Linden and T. B. Reddy, "Basic Concepts," in *Linden's Hanbook of Batteries*, T. B. Reddy, Ed., The McGraw-Hill Companies, Inc, 2011, pp. 1.3 - 1.17.

[18] G. E. Blomgren, "Battery Electrolytes," in *Lynden's Handbook of Batteries*, T. B. Reddy, Ed., The McGraw-Hill Companies, Inc., 2011, pp. 7.1 - 7.11.

[19] P. Arora and Z. J. Zhang, "Battery Separators," *Chemical Reviews*, vol. 104 (10), pp. 4419-4462, 2004.

[20] W. Böhnstedt, "Separators," in *Handbook of Battery Materials*, C. Daniel and J. O. Besenhard, Eds., Weinheim, Wiley-VCH, 2011, pp. 285-340.

[21] K. E. Thomas, J. Newman and R. M. Darling, "Mathematical Modeling of Lithium Batteries," in *Advances in Lithium-ion Batteries*, W. A. van Schalkwijk and B. Scrosati, Eds., Kluwer Academic Publishers, 2002, pp. 354-392.

[22] M. Salomon, "Electrochemical Principles and Reactions," in *Lynden's Handbook of Batteries*, T. B. Reddy and D. Linden, Eds., Mc Gray Hill, 2011, pp. 2.1 - 2.6.

[23] J. M. Tarascon and M. Armand, "Issues and challenges facing rechargeable lithium batteries," *Nature*, vol. 414, p. 359–367, 2001.

[24] G. Bieker, M. Winter and P. Bieker, "Electrochemical in situ investigations of SEI and dendrite formation on the lithium metal anode," *Physical Chemistry Chemical Physics*, vol. 17, pp. 8670-8679, 2015.

[25] Z. Peng, S. Wang, J. Zhow, Y. Jin, Y. Liu, Y. Qin, C. Shen, W. Han and D. Wang, "Volumetric variation confinement: surface protective structure for high cyclic stability of lithium metal electrodes," *Journal of Materials Chemistry A*, vol. 4, pp. 2427-2432, 2016.

[26] W. Xu, J. Wang, F. Ding, X. Chen, E. Nasybulin, Y. Zhang and J.-G. Zhang, "Lithium metal anodes for rechargeable batteries," *Energy and Environmental Science*, vol. 7, p. 513–537, 2014.

[27] F. Orsini, A. Du Pasquier, B. Beaudoin, J. M. Tarascon, M. Trentin, N. Langenhuizen, E. De Beer and P. Notten, "In situ Scanning Electron Microscopy (SEM) observation of interfaces within plastic lithium batteries," *Journal of Power Sources*, vol. 76, pp. 19-29, 1998.

[28] J. Dahn and G. M. Ehrlicj, "Chapter 26: Lithium-ion Batteries," in *Linden's Handbook of Batteries*, McGraw-Hill Education, 2011, p. 26.2.

[29] A. Manthiram and T. Muraliganth, "Lithium Intercalation Cathode Materials for Lithium-Ion Batteries," in *Handbook of Battery Materials*, C. Daniel and J. O. Besenhard, Eds., Weinheim, Weinheim: Wiley-VCH Verlag & Co. KGaA, 2011.

[30] M. S. Whittingham, "Lithium Batteries and Cathode Materials," *Chemical Reviews,* vol. 103, pp. 4271-4301, 2004.

[31] S. Min-Kuy, P. Soojin, A. M. Faisal, C. Jaephil and L. Meilin, "Nanostructured electrodes for lithium-ion and lithium-air batteries: the latest developments, challenges, and perspectives," *Materials, Science and Engineering,* vol. 72, pp. 203-252, 2011.

[32] M. Wohlfahrt-Mehrens, C. Vogler and J. Garche, "Aging mechanisms of lithium cathode materials," *Journal of power Sources,* vol. 127, pp. 58-64, 2004.

[33] G. Sarre, P. Blanchard and M. Broussely, "Aging of lithium-ion batteries," *Journal of Power Sources,* vol. 127, pp. 65-71, 2004.

[34] W. Qingsong, P. Ping, Z. Xuejuan, C. Guanquan, S. Jinhua and C. Chunhua, "Thermal runway caused fire and explosion of lithium ion battery," *Journal of Power Sources,* vol. 208, pp. 210-224, 2012.

[35] N. Angulakshmi and A. M. Stephan, "Efficient electrolytes for lithium-sulfur batteries," *Frontiers in Energy Research,* vol. 3, pp. 1-8, 2015.

[36] D. Moy, A. Manivannan and S. R. Narayanan, "Direct Measurement of Polysulfide Shuttle Current: A Window into Understanding the Performance of Lithium-Sulfur Cells," *Journal of the Electrochemical Society,* vol. 162 (1), pp. A1-A7, 2015.

[37] D. Aurbach, E. Pollak, R. Elazari, G. Salitra, C. Scordilis Kelley and J. Affinito, "On the Surface Chemical Aspects of Very High Energy Density, Rechargeable Li-Sulfur Batteries," *Journal of the ElectrochemicalSociety,* vol. 156, pp. A694-A702, 2009.

[38] S. S. Zhang, "Liquid electrolyte lithium/sulfur battery: Fundamental chemistry, problems, and solutions," *Power Sources,* vol. 231, p. 154, 2013.

[39] T. Poux, P. Novák and S. Trabesinger, "Pitfalls in LiS Rate-Capability Evaluation," *Journal of The Electrochemical Society,* vol. 163 (7), pp. A1139-A1145, 2016.

[40] Y. V. Mikhaylik and J. R. Akridge, "Polysulfide Shuttle Study in the Li/S Battery," *Journal of The Electrochemical Society,* vol. 151 (11), pp. A1969-A1976, 2004.

[41] A. F. Hofmann, D. N. Fronczek and W. G. Bessler, "Mechanistic modeling of polysulfide shuttle and capacity loss of lithium-sulfur batteries," *Journal of Power Sources,* vol. 259, pp. 300-310, 2014.

[42] C. Sang-Eun, K. Ki-Seok, C. Ji-Hoon, K. Sun-Wook, C. Eog-Yong and K. Hee-Tak, "Rechargeable Lithium Sulfur Battery I. Structural Change of Sulfur Cathode During Discharge and Charge," *Journal of Eletrochemical Society,* vol. 150 (6), pp. A796-A799, 2003.

[43] C. Sang-Eun, K. Ki-Seok, C. Ji-Hoon, K. Sun-Wook, C. Eog-Yong and K. Hee-Tak, "Rechargeable Lithium Sulfur Battery II. Rate Capability and Cycle Characteristics," *Journal of Electrochemical Society,* no. 150, pp. A800-A805, 2003.

[44] C. Sang-Eun, C. Soo-Seok, H. Ji-Seong, C. Yun-Suk, J. Bok-Hwan and L. S. Hong, "Capacity Fading Mechanisms on Cycling a High-Capacity Secondary Sulfur Cathode," *Journal of The Electrochemical Society,* vol. 151 (12), pp. A2067-A2073, 2004.

[45] R. Elazari, G. Salitra, Y. Talyosef, J. Grinblat, C. Scordilis-Kelley, A. Xiao, J. Affinito and D. Aurbach, "Morphological and Structural Studies of Composite Sulfur Electrodes upon Cycling by HRTEM, AFM and Raman Spectroscopy," *Journal of The Electrochemical Society,* vol. 157 (10), pp. A1131-A1138, 2010.

[46] H. S. Ryu, H. J. Ahn, K. W. Kim, J. H. Ahn, K. K. Cho and T. H. Nam, "Discharge characteristics of lithium/sulfur batteries using TEGDME liquid electrolyte," *Electrochimica Acta,* vol. 52, pp. 1563-1566, 2006.

[47] D.-W. Wang, Q. Zeng, G. Zhou, L. Yin, F. Li, H.-M. Cheng, I. R. Gentle and G. Q. M. Lu, "Carbon-sulfur composites for Li-S batteries: status and prospects," *Journals of Materials Chemistry A,* vol. 1, pp. 9382-9394, 2013.

[48] S. Zhang, K. Ueno, K. Dokko and M. Watanabe, "Recent Advances in Electrolytes for Lithium-Sulfur Batteries," *Material Views,* vol. 5, pp. 2-28, 2015.

[49] J. Shim, K. A. Striebel and E. J. Cairns, "The Lithium/Sulfur Rechargeable Cell Effects of Electrode Composition and Solvent on Cell Performance," *Journal of the Electrochemical Society,* vol. 149, pp. 1321-1325, 2002.

[50] H. Jha, I. Buchberger, X. Cui, S. Meini and H. A. Gasteiger, "Li-S Batteries with Li2S Cathodes and Si/C Anodes," *The Electrochemical Society,* vol. 162 (9), pp. A1829-A1835, 2015.

[51] M. Agostini, J. Hassoun, J. Liu, M. Jeong, H. Nara, T. Momma, T. Osaka, Y.-K. Sun and B. Scrosati, "A Lithium-Ion Sulfur Battery Based on a Carbon-Coated Lithium-Sulfide Cathode and an Electrodeposited Silicon-Based Anode," *Applied Materials & Interfaces,* vol. 6, p. 10924–10928, 2014.

[52] J. Hassoun, Y.-K. Sun and B. Scrosati, "Rechargeable lithium sulfide electrode for a polymer tin/sulfur lithium-ion battery," *Power Sources,* vol. 196, pp. 343-348, 2010.

[53] S. Zheng, Y. Chen, Y. Xu, F. Yi, Y. Zhu, Y. Liu, Y. Junhe and C. Wang, "In Situ Formed Lithium Sulfide/Microporous Carbon Cathodes for Lithium-Ion Batteries," *ACS Nano,* vol. 7 (12), pp. 10995-11003, 2013.

[54] C. Brissot, M. Rosso, J. -N. Chazalviel and S. Lascaud, "Dendritic growth mechanisms in lithium/polymer cells," *Journal of Power Sources,* Vols. 81-82, pp. 925-929, 1999.

[55] X. H. Liu, L. Zhong, L. Q. Zhang, A. Kushima, S. X. Mao, J. Li, Z. Z. Ye, J. P. Sullivan and J. Y. Huang, "Lithium fiber growth on the anode in a nanowire lithium ion battery during charging," *Applied Physics Letters,* vol. 98, p. 183107, 2011.

[56] T. Yang, X. Wang, W. Donghuang, L. Shuhan, D. Xie, X. Zhang and J. Tu, "Facile and scalable synthesis of nanosized core-shell Li2S@C composite for high-performance lithium-sulfur batteries," *Journal of Materials Chemistry A,* vol. 4, pp. 16653-16660, 2016.

[57] M. N. Obrovac and J. R. Dahn, "Electrochemically Active Lithia/Metal and Lithium Sulfide/Metal Composites," *Electrochemical and Solid-State Letters,* vol. 5 (4), pp. A70-A73, 2002.

[58] Y. Yang, G. Zheng, S. Misra, J. Nelson, M. F. Toney and Y. Cui, "High-Capacity Micrometer-Sized Li2S Particles as Cathode Materials for Advanced Rechargeable Lithium-Ion Batteries," *The American Chemical Society,* vol. 134, pp. 15837-15394, 2012.

[59] Y. Jung and B. Kang, "Understanding abnormal potential behaviors at the 1st charge in Li2S cathode material for rechargeable Li-S batteries," *PCCP,* 2016.

[60] R. Xu, X. Zhang, C. Yu, Y. Ren, J. C. M. Li and I. Belharouak, "Paving the Way for Using Li2S Batteries," *ChemSusChem,* vol. 7, pp. 2457-2460, 2014.

[61] A. Manthiram, Y. Fu, S.-H. Chung, C. Zu and Y.-S. Su, "Rechargeable Lithium-Sulfur Batteries," *Chemical Reviews,* vol. 114, 2014.

[62] J. Hassoun and B. Scrosati, "A High-Performance Polymer Tin Sulfur Lithium Battery," *Angewandte Chemie,* vol. 49, pp. 2371-2374, 2010.

[63] J. Xiulei, L. Kyu Tae and N. Linda F., "A highly ordered nanostructured carbon-sulphur cathode for lithium-sulphur batteries," *Nature Materials,* vol. 8, pp. 500-506, 2009.

[64] N. Jayaprakash, J. Shen, S. S. Moganty, A. Corona and L. A. Archer, "Porous Hollow Carbon@Sulfur Composites for High-Power Lithium-Sulfur Batteries," *Angewadte Chemie,* vol. 50, pp. 5094-5098, 2011.

[65] Z. Guangyuan, Y. Yuan, C. Judy J., H. Seung Sae and Y. Cui, "Hollow Carbon Nanofiber-Encapsulated Sulfur Cathodes for High Specific Capacity Rechargeable Lithium Batteries," *Nanoletters,* vol. 11, pp. 4462-4467, 2011.

[66] M. Barghamadi, A. Kapoor and C. Wen, "Review on Li-S Batteries as a High Efficiency Rechargeable Lithium Battery," *Journal of The Electrochemical Society,* vol. 160 (8), pp. A1256-A1263, 2013.

[67] Z. W. Seh, Q. Zhang, W. Li, G. Zheng, H. Yao and Y. Cui, "Stable cycling of lithium sulfide cathodes through strong affinity with a bifunctional binder," *Chemical Science,* vol. 4, pp. 3673-3677, 2013.

[68] M. J. Lacey, F. Jeschull, K. Edström and D. Brandell, "Why PEO as a binder or polymer coating increases capacity in the Li-S system," *Chemical Communications,* vol. 49, pp. 8531-8533, 2013.

[69] H. Schneider, A. Garsuch, A. Panchenko, O. Gronwald, N. Janssen and P. Novák, "Influence of different electrode compositions and binder materials on the performance of lithium-sulfur batteries," *Journal of Power Sources,* vol. 205, pp. 420-425, 2012.

[70] J. Gao, M. A. Lowe, Y. Kiya and H. D. Abruña, "Effects of Liquid Electrolytes on the Charge-Discharge Performance of Rechargeable Lithium/Sulfur Batteries: Electrochemical and in-Situ X-ray Absorption Spectroscopic Studies," *Physical Chemistry C,* vol. 115, pp. 25132-25137, 2011.

[71] Y. Gofer, Y. Ein Ely and D. Aurbach, "Surface Chemistry of Lithium in 1,3-dioxolane," *Electrochimica Acta,* vol. 37, pp. 1897-1899, 1992.

[72] Y. Mikhaylik, I. Kovalev, R. Schock, K. Kumaresan, J. Xu and J. Affinito, "High Energy Rechargeable Li-S Cells for EV Application. Status, Remaining Problems and Solutions," *ECS Transactions,* vol. 25, pp. 23-34, 2010.

[73] Y. Aihara, T. Bando, H. Nakagawa, H. Yoshida, K. Hayamizu, E. Akiba and W. S. Price, "Ion Transport Properties of Six Lithium Salts Dissolved in γ-Butyrolactone Studied by Self-Diffusion and Ionic Conductivity Measurements," *Journal of The Electrochemical Society,* vol. 151 (1), pp. A119-A122, 2004.

[74] J. T. Dudley, D. P. Wilkinson, G. Thomas, R. LeVae, S. Woo, H. Blom, C. Horvath, M. W. Juzkow, B. Denis, P. Juric, P. Aghakian and J. R. Dahn, "Conductivity of electrolytes for rechargeable lithium batteries," *Journal of Power Sources,* vol. 35, pp. 59-82, 1991.

[75] K. Xu and C. A. Angell, "Sulfone-Based Electrolytes for Lithium-Ion Batteries," *Journal of Electrochemical Society,* vol. 149, pp. A920-A926, 2001.

[76] S. S. Zhang, "Role of LiNO3 in rechargeable lithium/sulfur battery," *Electrochimica Acta,* vol. 70, pp. 344-348, 2012.

[77] X. Y., L. J., L. J., L. D., X. Z., Q. D., L. K., D. T. and T. H., "Advanced Separators for Lithium-Ion and Lithium-Sulfur Batteries: A Review of Recent Progress," *ChemSusChem,* vol. 9, p. 3023–3039, 2016.

[78] S. Yan, X. Xiao, X. Huang, X. Li and Y. Qi, "Unveiling the environment-dependent mechanical properties of porous polypropylene separators," *Polymer,* vol. 55, pp. 6282-6292, 2014.

[79] L. Celgard, "Celgard Product Comparison," 2009. [Online]. Available: http://www.jobike.it/Public/data/Daniele%20Consolini/2012517114032_Celgard_Product_Comparison_10002.pdf. [Accessed 5 6 2016].

[80] H. Yao, K. Yan, W. Li, G. Zheng, D. Kong, Z. W. Seh, V. K. Narasimhan, Z. Liang and Y. Cui, "Improved lithium-sulfur batteries with a conductive coating on the separator to prevent the accumulation of inactive S-related species at the cathode-separator interface," *Energy & Environmental Science,* Vols. 3381-3390, p. 7, 2014.

[81] A. Manthiram, S.-H. Chung and C. Zu, "Lithium-Sulfur Batteries: Progress and Prospects," *Advanced Materials,* vol. 27, pp. 1980-2006, 2015.

[82] Y.-S. Su and A. Manthiram, "A new approach to improve cycle performance of rechargeable lithium–sulfur batteries by inserting a free-standing MWCNT interlayer," *Chemical Communications,* vol. 48, pp. 8817-8819 , 2012.

[83] R. Singhal, S.-H. Chung and A. Manthiram, "A free-standing carbon nanofiber interlayer for high-performance lithium-sulfur batteries," *Materials Chemistry A,* vol. 3, pp. 4530-4538, 2015.

[84] I. W. Hamley, "Nanotechnology with Soft Materials," *Angewandte Chemie,* vol. 42, pp. 1692-1712, 2003.

[85] M. Grzelczak, J. Vermant, E. M. Furst and L. M. Liz-Marzán, "Directed Self-Assembly of Nanoparticles," *ACS Nano,* vol. 4, pp. 3591-3605, 2010.

[86] K. J. Stine and B. G. Moore, "Langmuir Monolayers: Fundamentals and Relevance to Nanotechnology," in *Nano-Surface Chemistry*, M. Rosoff, Ed., New York, Macel Dekker, Inc., 2002, pp. 59-139.

[87] C. H. Giles, S. D. Forrester and G. G. Roberts, "Historial Introduction," in *Langmuir-Blodgett Films*, G. Roberts, Ed., Springer Science+Business Media, LLC, 1990, pp. 1-14.

[88] A. Ulman, "Applications of LB and SA films," in *An Introduction to Ultrathin Organic Films From Langmuir-Blodgett to Self-Assembly*, San Diego, Academic Press, Inc, 1991, pp. 339 - 413.

[89] "Unified Approach to Self-Assembly," in *Self-Assembly and Nanotechnology: A Force Balance Approach*, New Jersey, John Wiley & Sons, Inc, 2008, pp. 3-18.

[90] L. S. Yoon, "Nanostructured Films," in *Self-Assembly and Nanotechnology: A Force Balance Approach*, Hoboken, New Jersey, John Wiley & Sons, Inc., 2008, pp. 249-269.

[91] R. A. Hann, "Molecular Structure and Monolayer Properties," in *Langmuir-Blodgett Films:*, G. Roberts, Ed., New York, Springer Science+Business Media, LLC, 1990, pp. 17-92.

[92] Y. Yuan and T. R. Lee, "Contact Angle and Wetting Properties," in *Surface Science Techniques*, vol. 51, G. Bracco and B. Holst, Eds., Springer, 2013, pp. 3-34.

[93] M. C. Petty, "Monolayers: two-dimensional phases," in *Langmuir-Blodgett Films: An Introduction*, Cambridge University Press, 1996, pp. 12-37.

[94] M. C. Petty and W. A. Barlow, "Film Deposition," in *Langmuir-Blodgett Films*, G. Roberts, Ed., New York, Springer Science+Business Media, LLC, 1990, pp. 93-132.

[95] O. Witzgall, Herstellung und Optimierung von wässrigen Schwefelkathoden, Bachelor, 2016.

[96] M. Simolka, Li2S Kathoden der nächsten Generation, Fraunhofer Institute of Chemical Technology, 2014.

[97] R. Maça, Sulfur Cathodes and Li-S Pouch cells, Fraunhofer Institute of Chemical Technology, 2014.

[98] F. Bordet, K. Ahlbrecht, J. Tübke, J. Ufheil, T. Hoes, M. Oetken and M. Holzapfel, "Anion intercalation into graphite from sodium-containing electrolyte," *Electrochimica Acta*, vol. 174, p. 1318, 2015.

[99] A. J. Bard and L. R. Faulkner, "Electrochemical Methods: Fundamentals and Applications," vol. 2, New York, John Wiley & Sons, Inc., 2001, pp. 305-327.

[100] J. R. Taylor, "Statistical Analysis of Random Uncertainties," in *An Introduction to Error Analysis, The study of uncertainties in physical measurements*, Sausalito, California, University Science Books, 1997, pp. 93-119.

[101] J. I. Goldenstein, D. E. Newbyry, P. Echlin, D. C. Joy, C. E. Lyman, E. Lifshin, L. Sawyer and J. R. Michael, "Electron Beam-Specimen Interactions," in *Scanning Electron Microscopy and X-Ray Microanalysis*, New York, Kluwer Academic/Plenum Publishers, 2003, pp. 61-97.

[102] J. I. Goldstein, D. E. Newbury, P. Echlin, D. C. Joy, C. E. Lyman, E. Lifshin, L. Sawyer and J. R. Michael, "Generation of X-Rays in the SEM Specimen," in *Scanning Electron Microscopy and X-ray Microanalysis*, 3 ed., New York, Kluwer Academic/Plenum Publishers, 2003, pp. 271-295.

[103] M. S. Kim, L. Ma, S. Choudhury, S. Wei and L. A. Archer, "Fabricating multifunctional nanoparticle membranes by a fast layer-by-layer Langmuir-Blodgett process: application in lithium batteries," *Materials Chemistry A*, vol. 4, p. 14709–14719, 2016.

[104] B. G. Pollet, "Let's Not Ignore the Ultrasonic Effects on the Preparations of Fuel Cell Materials," *Electrocatalysis*, pp. 330-343, 2014.

[105] L. Dumée, K. Sears, J. Schütz, N. Finn, M. Duke and G. Stephen, "Influence of the Sonication Temperature on the Debundling Kinetics of Carbon Nanotubes in Propan-2-ol," *Nanomaterials*, pp. 70-85, 2013.

[106] J. Hilding, E. A. Grulke, G. Z. Zhang and F. Lockwood, "Dispersion of Carbon Nanotubes in Liquids," *Dispersion Science and Technology*, vol. 24, pp. 1-41, 2003.

[107] IKA®, "Manual T 10 basic ULTRA-TURRAX®," 2016. [Online]. Available: http://www.ika.com/owa/ika/catalog.product_downloads?iProduct=3737000. [Accessed 11 September 2016].

[108] Y. M. Park, D. H. Lee, W. R. Hwang, S. B. Lee and S.-I. Jung, "Hydrodynamics of CNT dispersion in high shear dispersion mixers," *Korea-Australia Rheology*, vol. 26, pp. 347-353, 2014.

[109] L. Vaisman, H. D. Wagner and G. Marom, "The role of surfactants in dispersion of carbon nanotubes," *Advances in Colloid and Interface Science*, pp. 128-130, 2006.

[110] Y. Jianhua, L. Xingbo and L. Bingyun, "Capacity Fade Analysis of Sulfur Cathodes in Li-S Batteries," *Material Views*, vol. 3, pp. 1-10, 2016.

[111] S.-H. Chung, P. Han, R. Singhal, V. Kalra and A. Manthiram, "Electrochemically Stable Rechargeable Lithium-Sulfur Batteries with a Microporous Carbon Nanofiber Filter for Polysulfide," *Advanced Energy Materials*, vol. 5, p. 1500738, 2015.

[112] N. Ding, S. W. Chien, T. S. A. Hor, Z. Liu and Y. Zong, "Key parameters in design of lithium sulfur batteries," *Journal of Power Sources*, vol. 269, pp. 111-116, 2014.

[113] D. Lv, J. Zheng, Q. Li, X. Xie, S. Ferrara, Z. Nie, L. B. Mehdi, N. D. Browning, J.-G. Zhang, G. L. Graff and J. Xiao, "High Energy Density Lithium-Sulfur Batteries: Challenges of Thick Sulfur Cathodes," *Advanced Energy Materials*, vol. 5, p. 1402290, 2015.

[114] J. Brückner, S. Thieme, H. T. Grossmann, S. Dörfler, H. Althues and S. Kaskel, "Lithium-sulfur batteries: Influence of C-rate, amount of electrolyte and sulfur loading on cycle performance," *Journal of Power Sources*, vol. 268, pp. 82-87, 2014.

[115] M. Hagen, P. Fanz and J. Tübke, "Cell energy density and electrolyte/sulfur ration in Li-S cells," *Journal of Power Sources*, vol. 264, pp. 30-34, 2014.

[116] P. Quan, L. Xiao, C. Z. Kwok and L. F. Nazar, "Review - The Importance of Chemical Interactions between Sulfur Host Materials and Lithium Polysulfides for Advanced Lithium-Sulfur Batteries," *Journal of The Electrochemical Society*, vol. 162, pp. A2567-A2576, 2015.

[117] X. Rui, L. Jun and A. Khalil, "Progress in Mechanistic Understanding and Characterization Techniques of Li-S Batteries," *Advanced Energy Materials*, vol. 5, pp. 1-22, 2015.

Appendices

A1: Image of multi-layered carbon-coated separators of Super C65

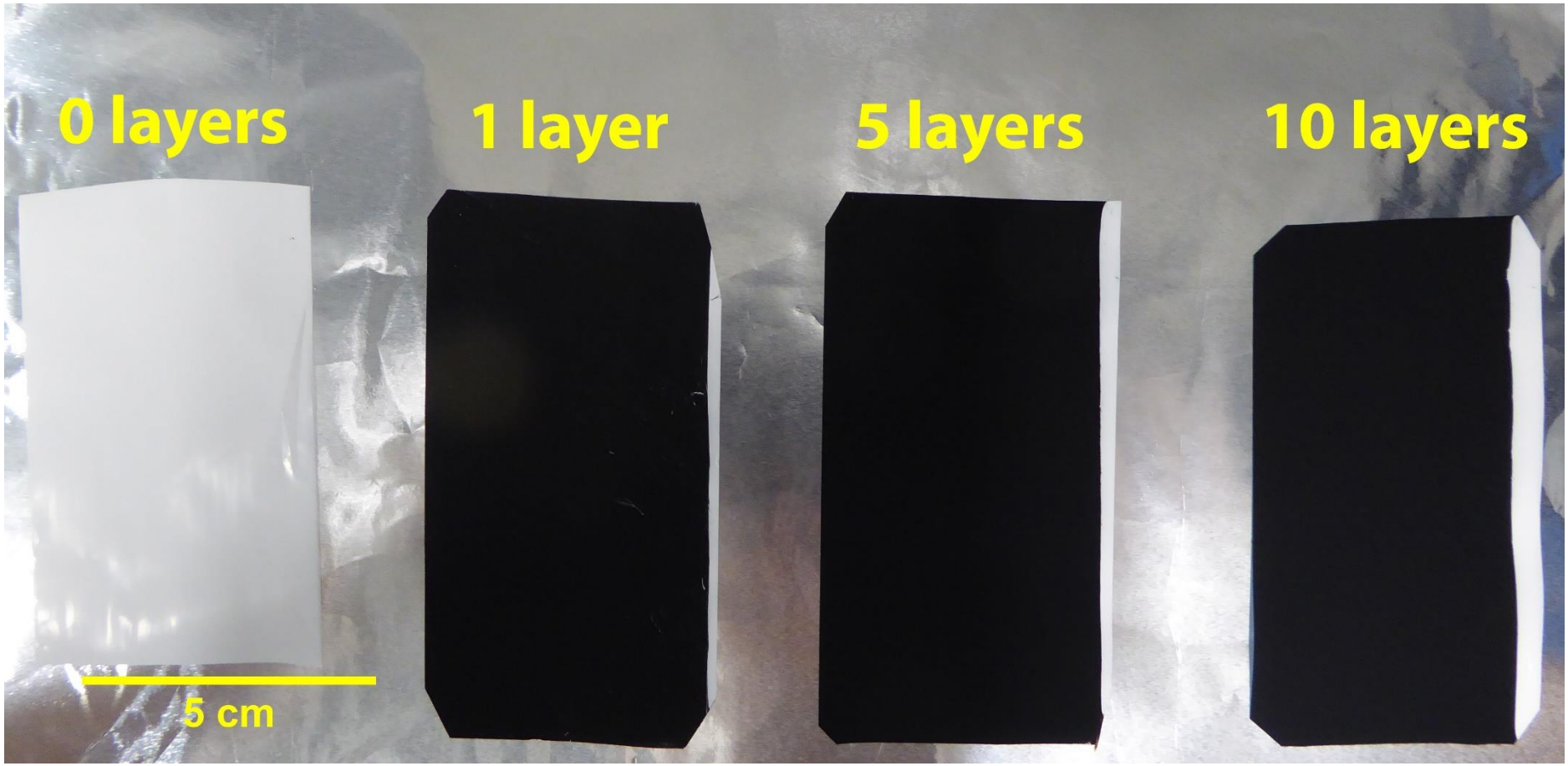

A2: Images of pouched carbon-coated separators

Front side

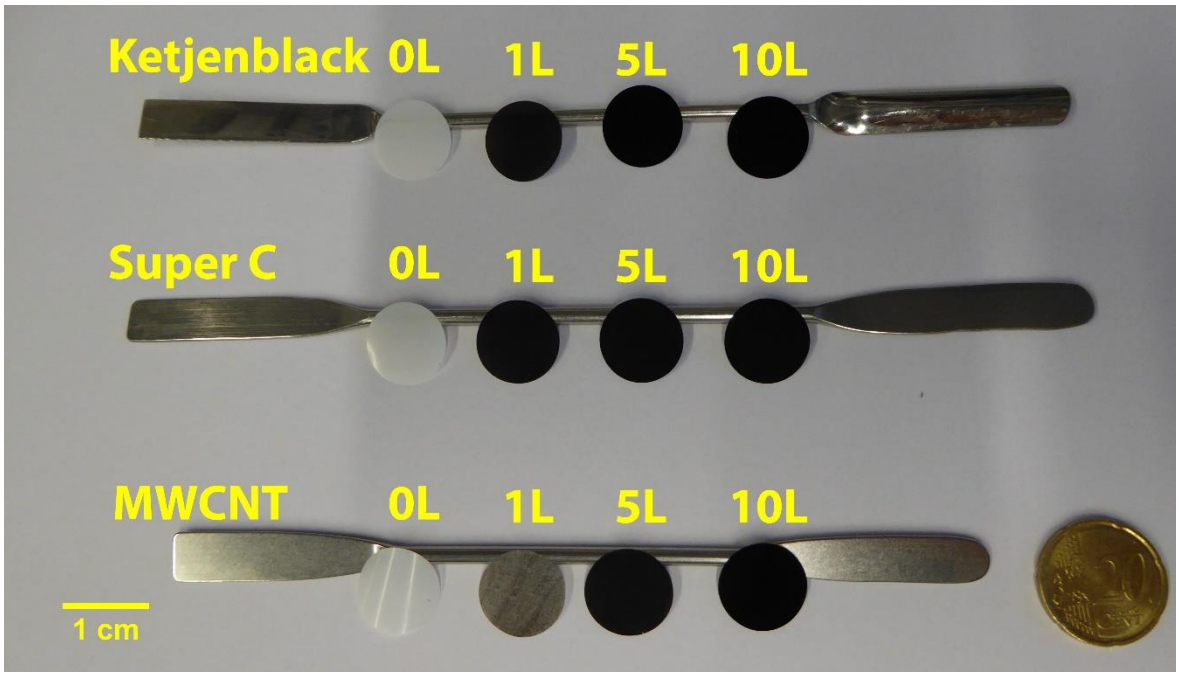

Back side

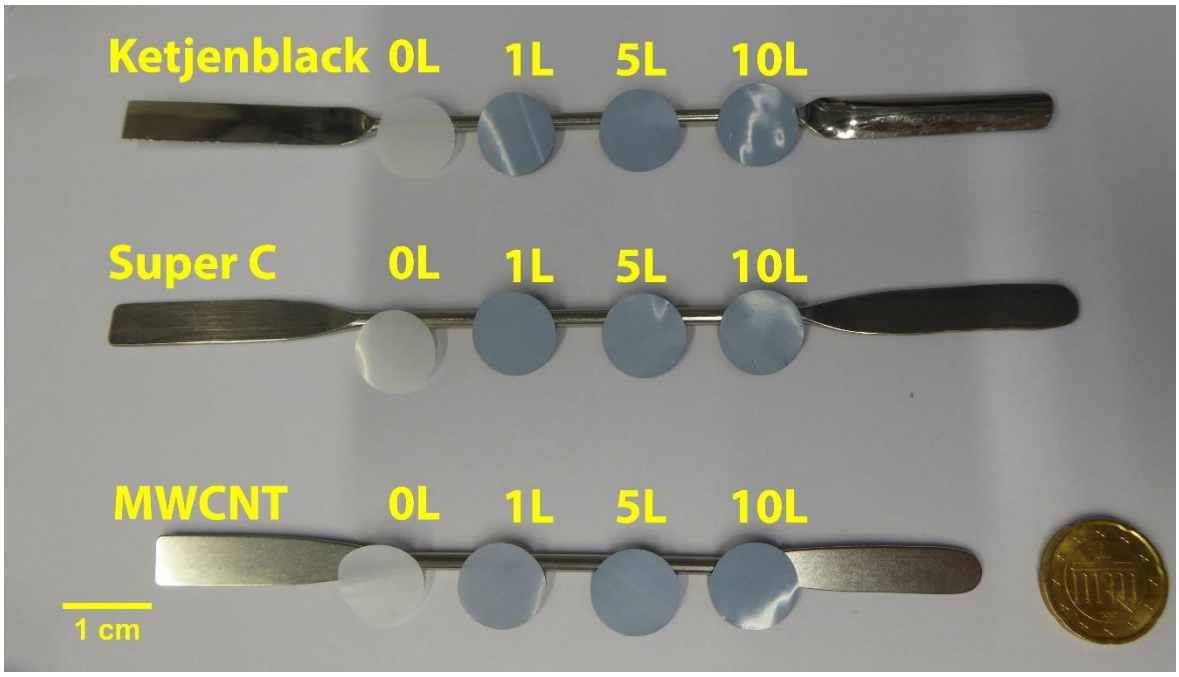

B: Galvanostatic cycling protocols

B1: Cells employing carbon-coated separators (Section 3.1)

Instructions	Current / mA	Current density / mA cm^{-2}	Conditions
Discharge	-0.5	-0.64	U < 1.8V & t>5 s
Charge	0.5	0.64	U > 2.6 V & t>25 h
Cycle end	Number = 10		
Discharge	-1.0	-1.27	U < 1.8V & t>5 s
Charge	1.0	1.27	U > 2.6 V & t>12 h
Cycle end	Number = 20		
Discharge	-2.0	-2.55	U < 1.8V & t>5 s
Charge	2.0	2.55	U > 2.6 V & t>6 h
Cycle end	Number = 20		
Discharge	-3.0	-3.82	U < 1.8V & t>5 s
Charge	3.0	3.82	U > 2.6 V & t>4 h
Cycle end	Number = 20		
Discharge	-0.5	-0.64	U < 1.8V & t>5 s
Charge	0.5	0.64	U > 2.6 V & t>25 h
Cycle end	Number = 20		

B2: Cells employing Li_2S cathodes (Section 4.7)

Instructions	Current / mA	Current density / mA cm^{-2}	Conditions
Charge	0.5	0.64	U > 3.8 V & t>25 h
Discharge	-0.5	-0.64	U < 1.8V & t>5 s
Cycle end	Number = 1		
Charge	0.5	0.64	U > 2.6 V & t>25 h
Discharge	-0.5	-0.64	U < 1.8V & t>5 s
Cycle end	Number = 9		
Charge	1.0	1.27	U > 2.6 V & t>12 h
Discharge	-1.0	-1.27	U < 1.8V & t>5 s
Cycle end	Number = 20		
Charge	2.0	2.55	U > 2.6 V & t>6 h
Discharge	-2.0	-2.55	U < 1.8V & t>5 s
Cycle end	Number = 20		
Charge	3.0	2.55	U > 2.6 V & t>4 h
Discharge	-3.0	-2.55	U < 1.8V & t>5 s
Cycle end	Number = 20		
Charge	0.5	0.64	U > 2.6 V & t>25 h
Discharge	-0.5	-0.64	U < 1.8V & t>5 s
Cycle end	Number = 19		

B3: Cells employing electrolyte E2 and SEM investigations (Sections 4.4 and 4.5)

Instructions	Current / mA	Current density / mA cm^{-2}	Conditions
Discharge	-0.5	-0.64	U < 1.8V & t>5 s
Charge	0.5	0.64	U > 2.6 V & t>25 h
Cycle end	Number = 5		

C: Thickness and active material loading of cathodes

C1: Sulfur cathodes used in galvanostatic investigations

Carbon-coating	Layers	Cell	Sulfur loading / mg cm^{-2}	Thickness / µm
None (Pristine)	0	1	4.2	146
		2	4.2	152
		3	4.2	156
Ketjenblack EC-600 JD	1	1	4.2	141
		2	4.2	147
		3	4.2	150
	5	1	4.2	150
		2	4.2	148
		3	4.2	152
	10	1	4.2	147
		2	4.2	148
		3	4.2	138
Super C65	1	1	4.3	152
		2	4.3	152
		3	4.2	151
	5	1	4.3	153
		2	4.2	152
		3	4.2	153
	10	1	4.3	153
		2	4.3	154
		3	4.2	154
Nanocyl NC7000	1	1	4.3	154
		2	4.3	155
		3	4.3	157
	5	1	4.3	156
		2	4.3	155
		3	4.3	150
	10	1	4.3	159
		2	4.3	149
		3	4.3	152

C2: Solvent-free Li_2S cathodes used in galvanostatic investigations

Carbon-coating	Layers	Cell	Li_2S loading / mg cm^{-2}	Thickness / µm
Pristine	PVP	1	0.6	59
		2	0.9	70
		3	1.5	81
	PEO	1	2.4	94
		2	3.1	123
		3	2.8	123
Carbon-coated	PVP	1	4.0	178
		2	4.2	123
		3	4.1	121
	PEO	1	3.5	120
		2	4.9	136
		3	4.3	121

D: Weight of the carbon-coating

The loading of the carbon-coatings was calculated by subtracting the mass of a carbon-coated separator and a pristine separator, and divided by the area of the separator (Ø = 1.6 cm, A = 2.01 cm^2).

Carbon-coating	Layers	Measurement 1	Measurement 2	Measurement 3	Average loading / µg cm^{-2}
Ketjenblack	1	39.79	34.82	34.82	36.47
	5	99.47	84.55	134.29	106.10
	10	104.45	94.50	174.08	124.43
Super C	1	74.60	39.79	99.47	71.29
	5	208.89	213.86	213.86	212.21
	10	303.39	343.18	328.26	324.94
MWCNT	1	39.79	39.79	39.79	39.79
	5	79.58	84.55	69.63	77.92
	10	64.66	109.42	109.42	94.50

E: EDX spectra

E1: Pristine metallic lithium

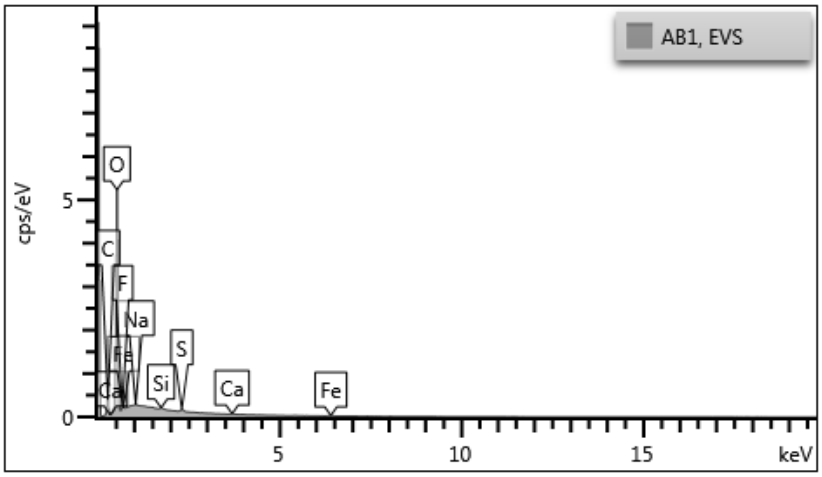

E2: Cycled metallic lithium anode retrieved from cycled cell employing pristine separator

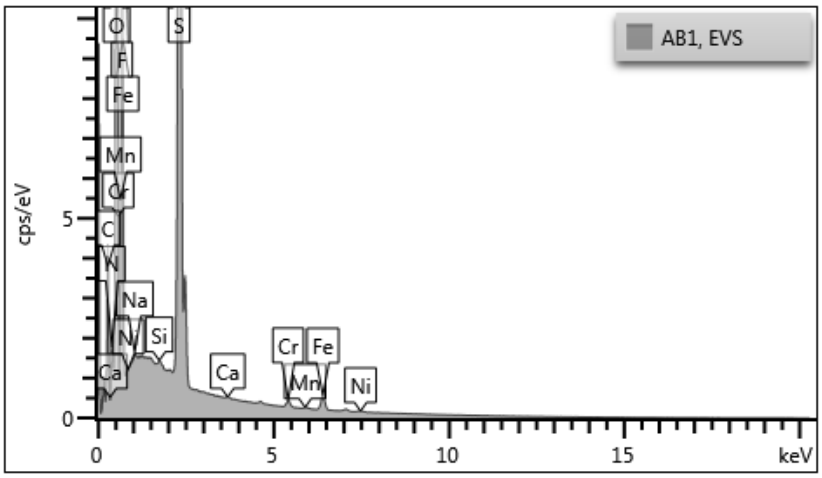

E2: Cycled metallic lithium anode retrieved from cycled cell employing coated separator with 10 layers of MWCNT

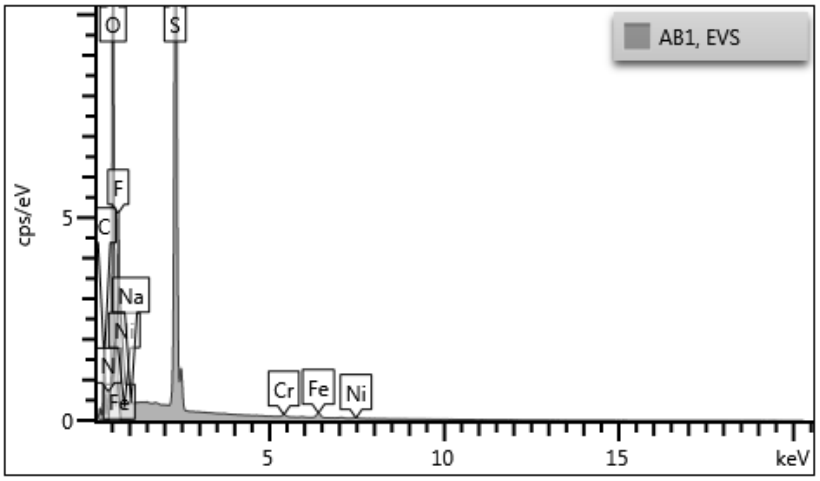

F: Thickness of the carbon-coatings

The thickness of multi-layered carbon-coatings was measured through confocal microscopy and micrometer. The measurements with a confocal microscope were performed by subtracting the average thickness at a spot with a carbon-coating and an area without the coating. Below is shown an image of a sample utilized to perform the confocal microscopy investigations, where is also illustrated the areas where the analysis was performed. The thicknesses calculated through this method are reported on the following pages. Nevertheless, it should be noted that some samples were not possible to analyze, such as the carbon-coatings comprised of 1 and 5 layers of MWCNT (marked in red on the table below). Therefore, another method was applied to quantify the thickness, for example with a micrometer. In such cases, the thickness was calculated by subtracting the thickness of a carbon-coated separator and a separator. After measuring the thicknesses, the values were averaged, and are listed in the table below.

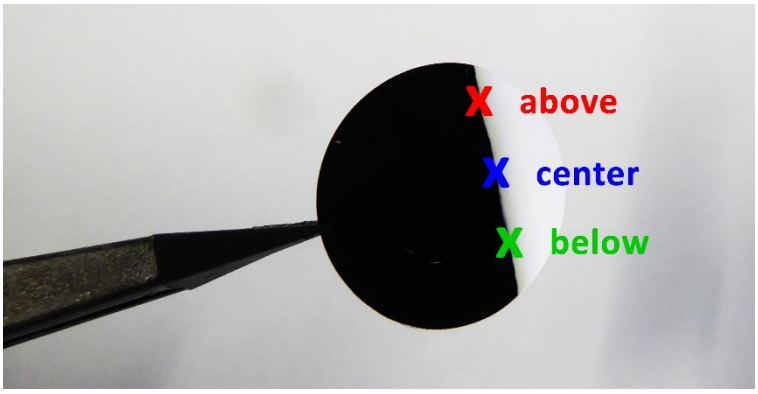

Carbon-coating	Layers	Measurement 1	Measurement 2	Measurement 3	Average thickness / µm
Ketjenblack	1	0.89	0.36	1.12	0.79
	5	1.45	1.83	1.28	1.52
	10	4.22	4.54	3.52	4.09
Super C	1	0.85	1.27	-	1.06
	5	4.53	2.87	2.59	3.24
	10	6.70	8.58	7.85	7.71
MWCNT	1	**1.00**	**0.00**	**0.00**	**0.33**
	5	**2.00**	**2.00**	**3.00**	**2.33**
	10	2.82	-	-	2.82

F1: Confocal microscopy investigations on carbon-coatings comprised of Ketjenblack EC600-JD – Ketjenblack (KB)

1 Layer

Above

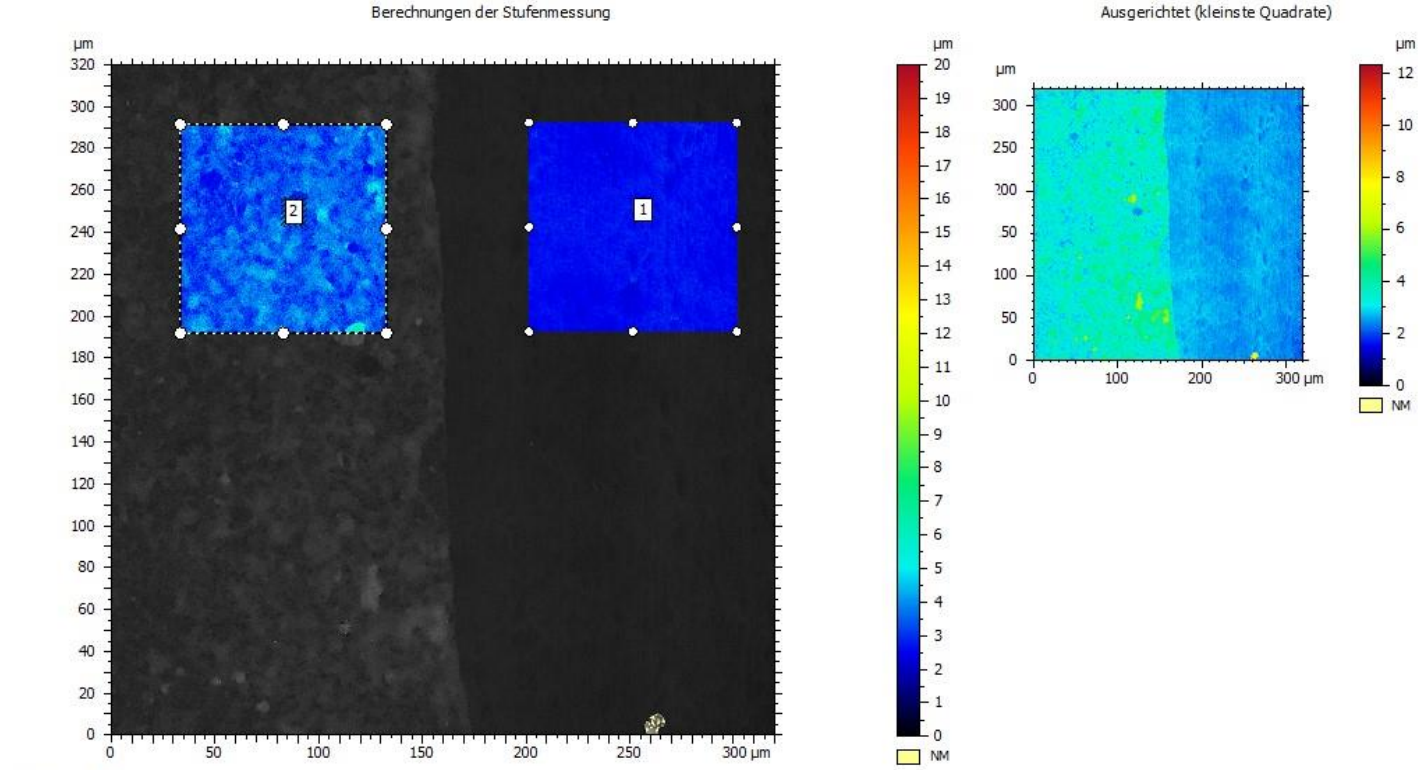

Differenzielle Parameter	Einheit	Wert
Zmean(2) - Zmean(1)	**µm**	**0.894**

Ebenen-Parameter	Einheit	Ebene 1	Ebene 2
Zmin	µm	0.778	0.573
ZMean	µm	2.60	3.49
Zmax	µm	3.57	6.96

Center

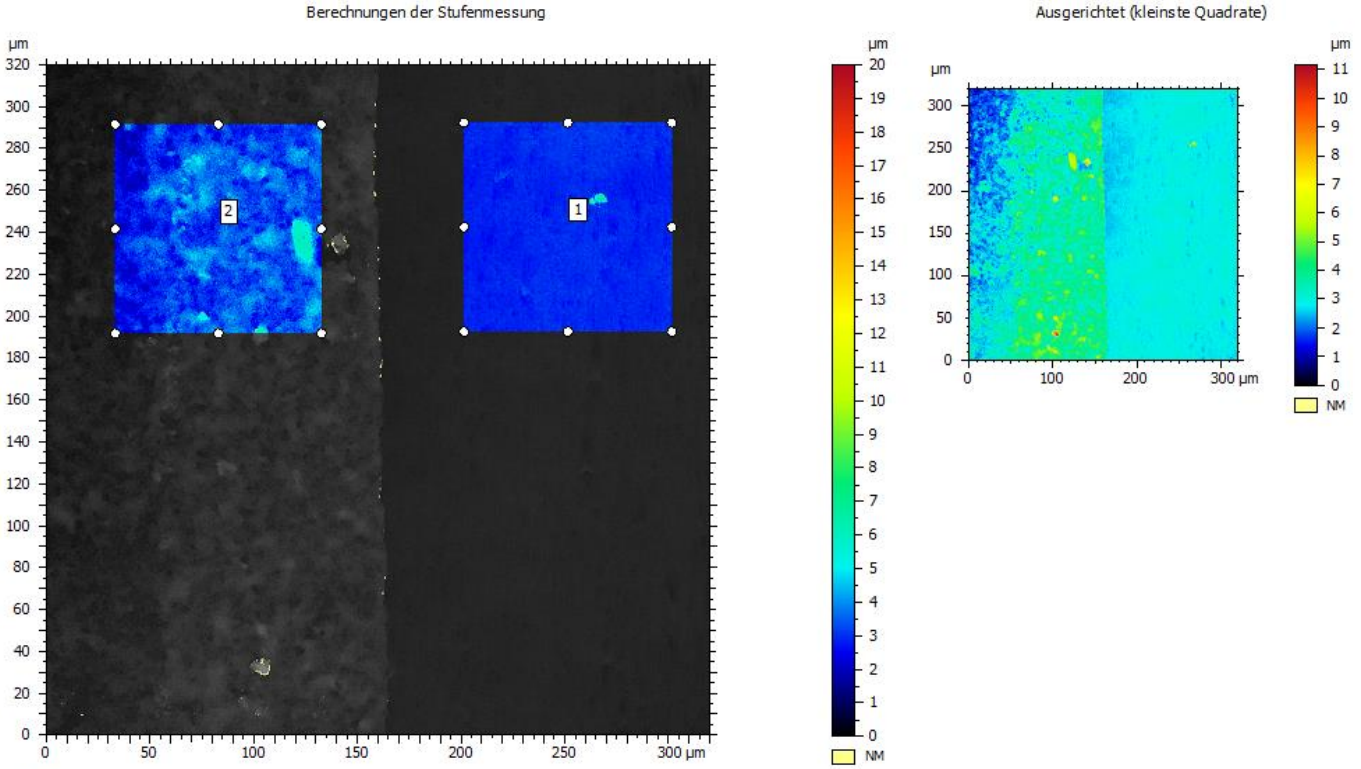

Differenzielle Parameter	Einheit	Wert
Zmean(2) - Zmean(1)	**µm**	**0.359**

Ebenen-Parameter	Einheit	Ebene 1	Ebene 2
Zmin	µm	0.784	0.466
ZMean	µm	2.91	3.27
Zmax	µm	7.77	7.04

Below

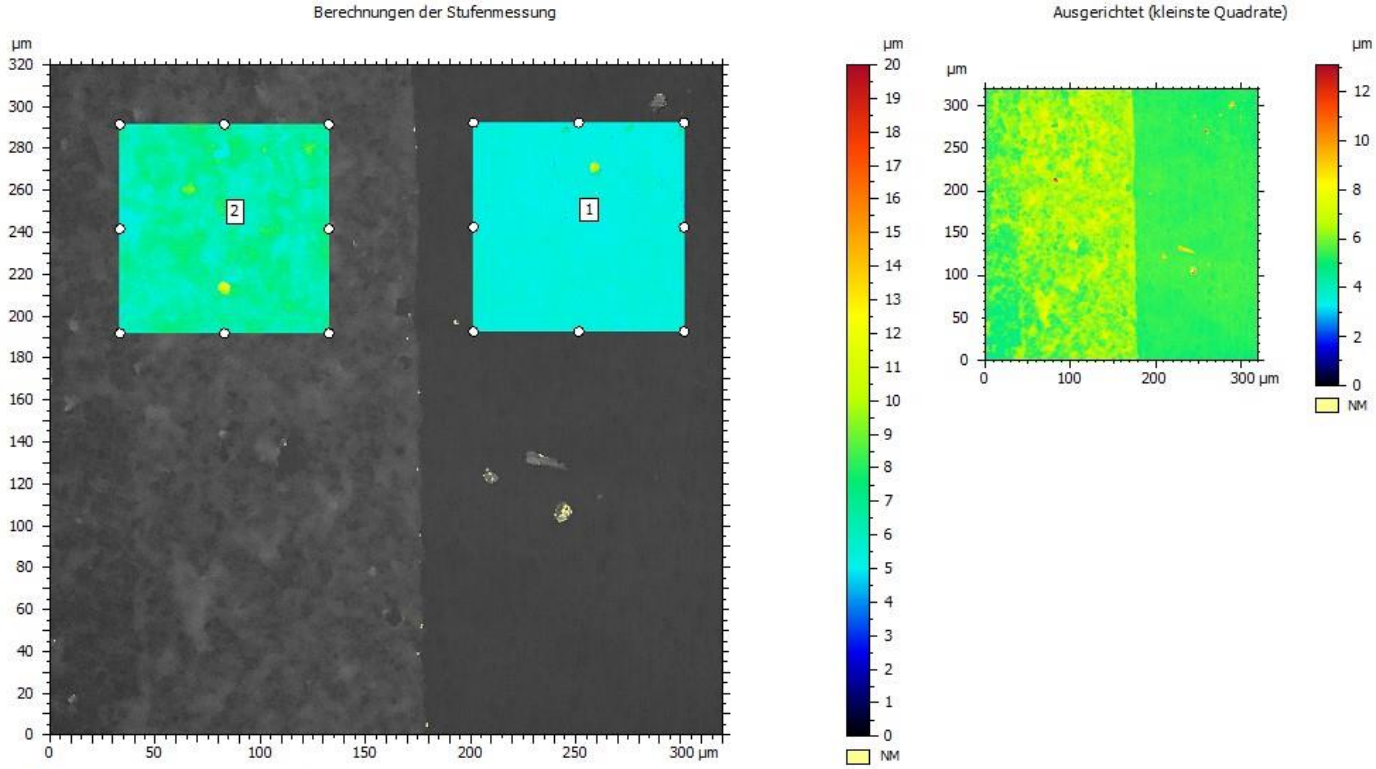

Differenzielle Parameter	Einheit	Wert
Zmean(2) - Zmean(1)	**µm**	**1.12**

Ebenen-Parameter	Einheit	Ebene 1	Ebene 2
Zmin	µm	3.02	3.48
ZMean	µm	5.37	6.49
Zmax	µm	11.8	13.0

5 Layers

Above

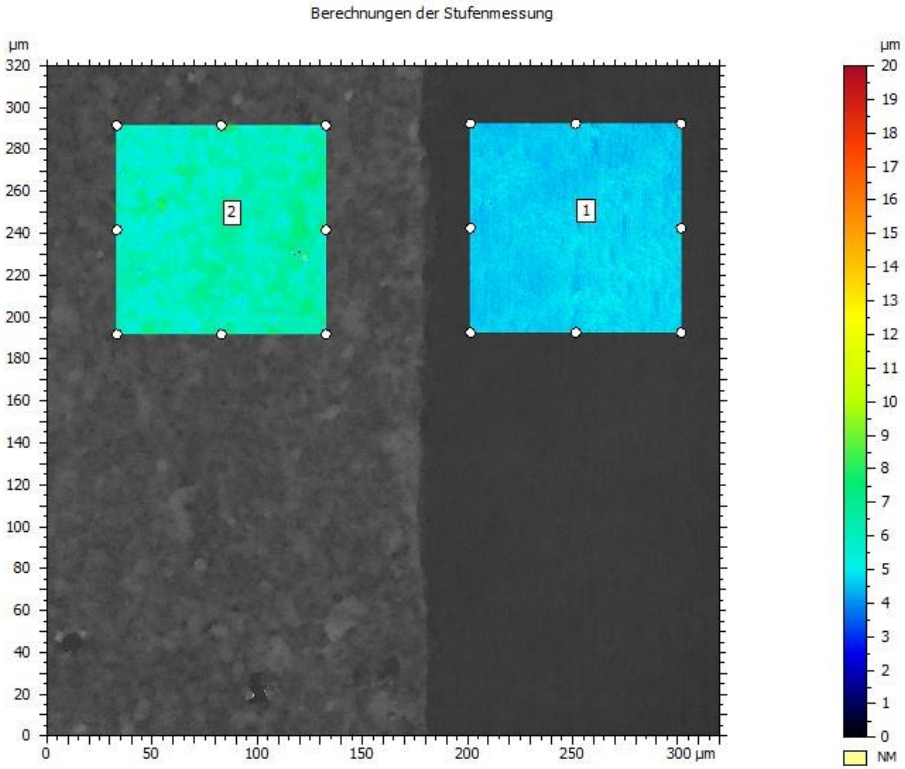

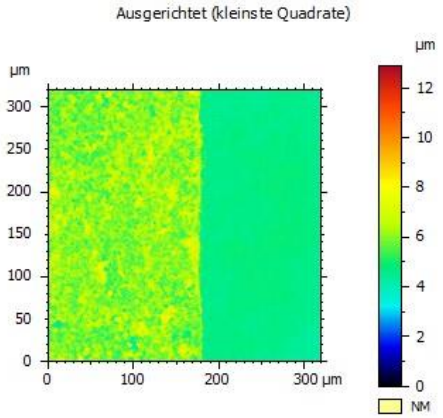

Differenzielle Parameter	Einheit	Wert
Zmean(2) - Zmean(1)	**µm**	**1.45**

Ebenen-Parameter	Einheit	Ebene 1	Ebene 2
Zmin	µm	2.77	0.00
ZMean	µm	4.66	6.12
Zmax	µm	5.76	12.9

Center

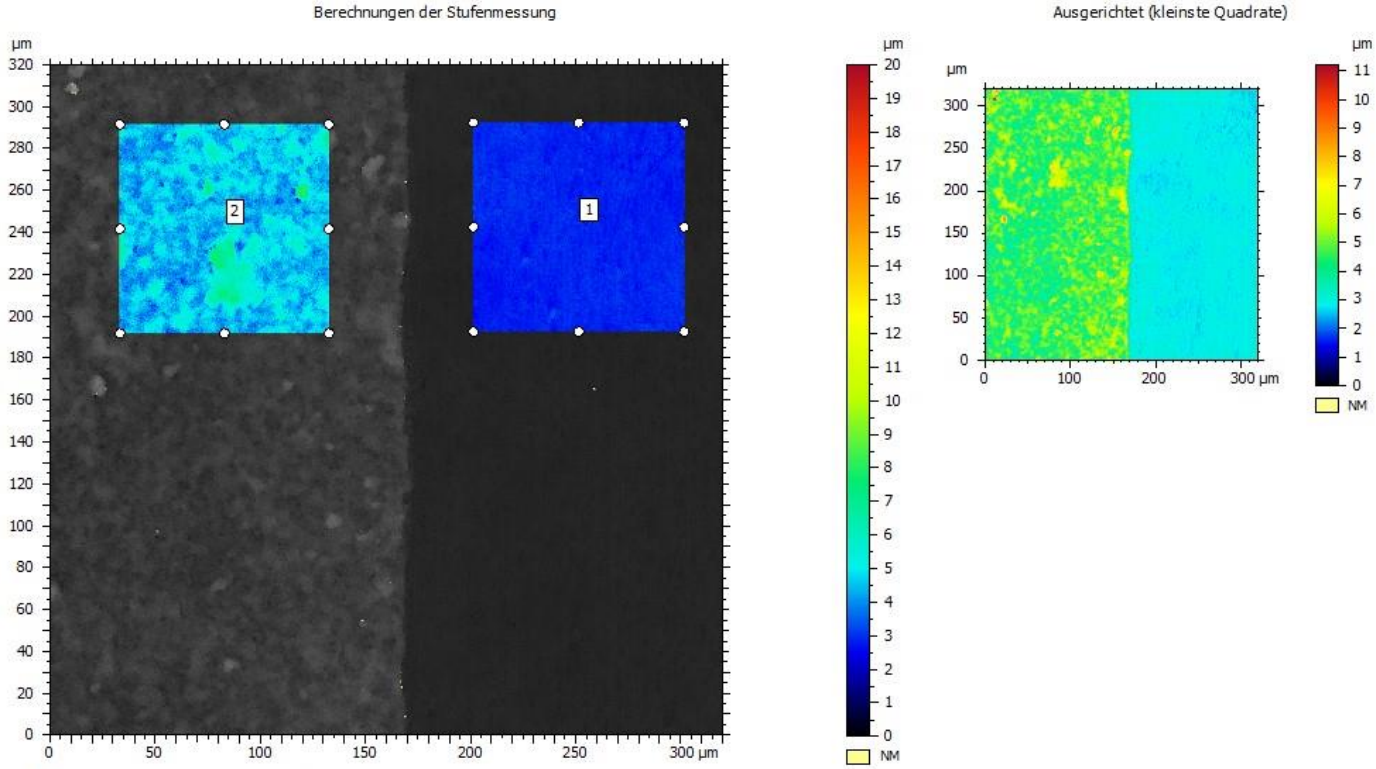

Differenzielle Parameter	Einheit	Wert
Zmean(2) - Zmean(1)	**µm**	**1.83**

Ebenen-Parameter	Einheit	Ebene 1	Ebene 2
Zmin	µm	1.24	1.98
ZMean	µm	2.87	4.70
Zmax	µm	4.03	8.87

Below

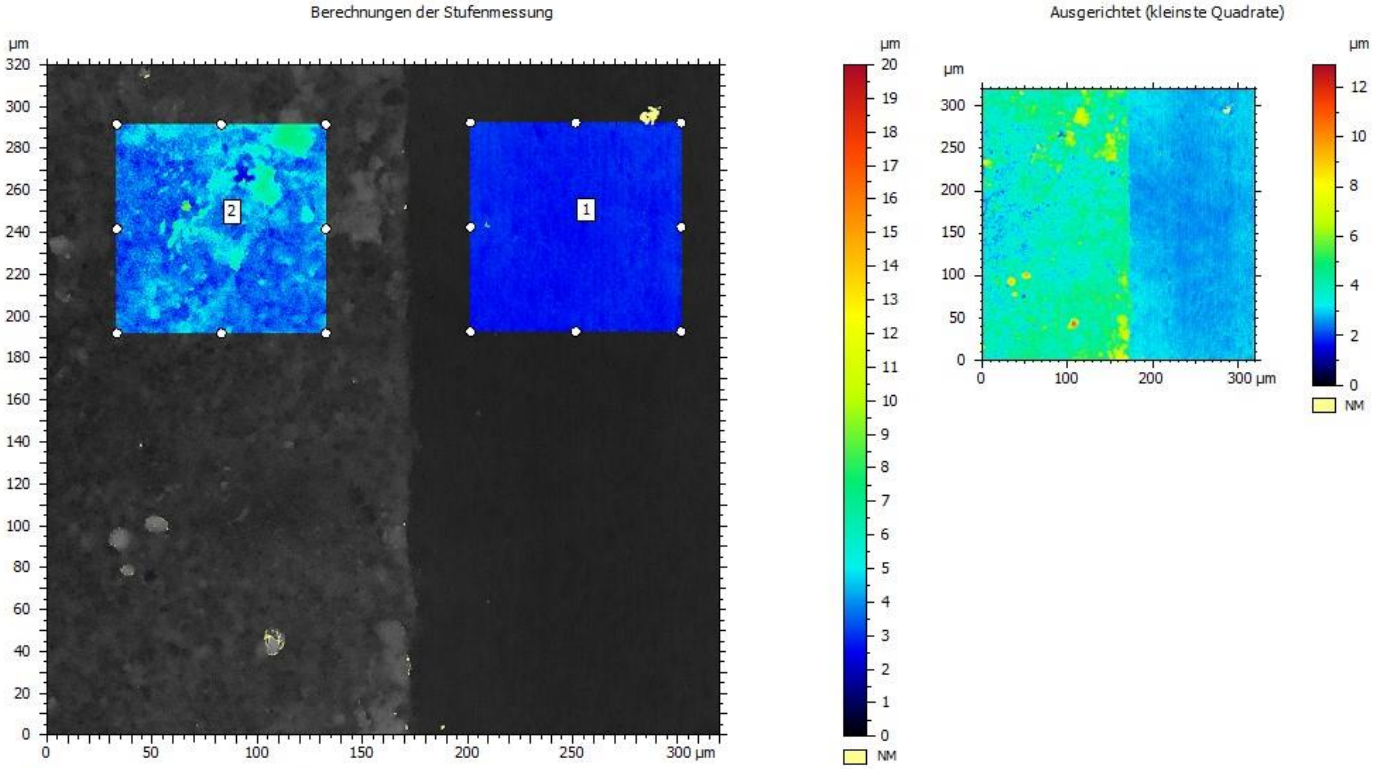

Differenzielle Parameter	Einheit	Wert
Zmean(2) - Zmean(1)	**µm**	**1.28**

Ebenen-Parameter	Einheit	Ebene 1	Ebene 2
Zmin	µm	0.00	0.805
ZMean	µm	2.78	4.05
Zmax	µm	7.32	10.4

10 Layers

Above

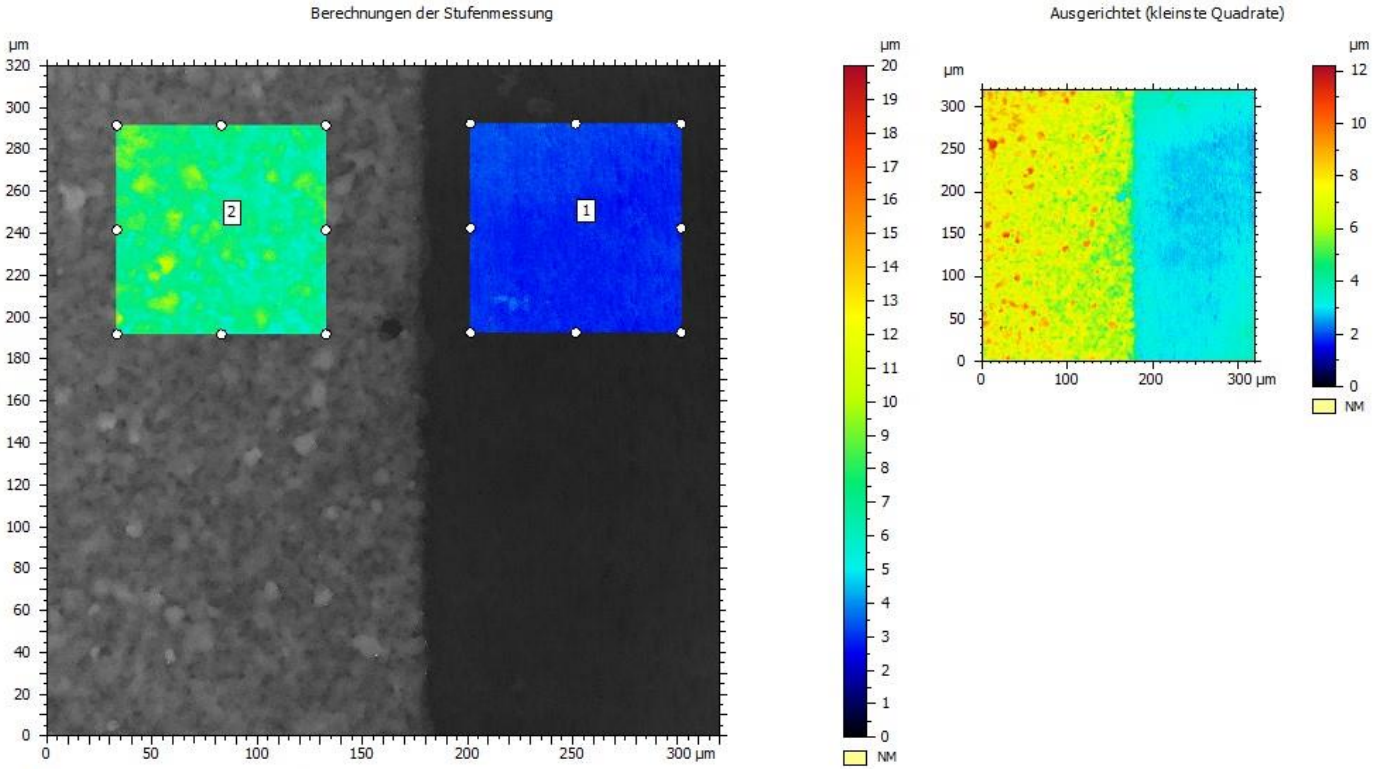

Differenzielle Parameter	Einheit	Wert
Zmean(2) - Zmean(1)	µm	4.22

Ebenen-Parameter	Einheit	Ebene 1	Ebene 2
Zmin	µm	0.819	3.41
ZMean	µm	2.95	7.17
Zmax	µm	4.58	12.1

Center

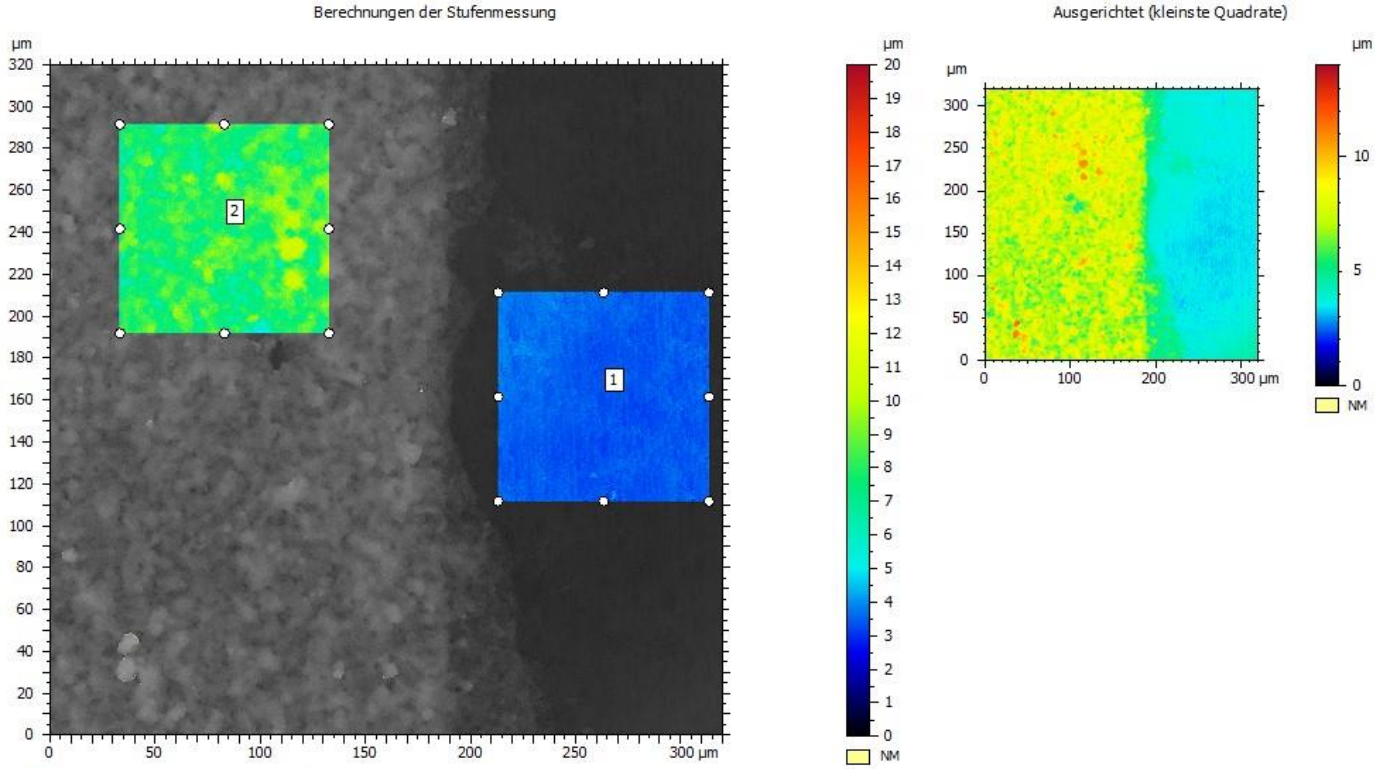

Differenzielle Parameter	Einheit	Wert
Zmean(2) - Zmean(1)	**µm**	**4.54**

Ebenen-Parameter	Einheit	Ebene 1	Ebene 2
Zmin	µm	0.916	3.67
ZMean	µm	3.47	8.01
Zmax	µm	4.72	12.4

Below

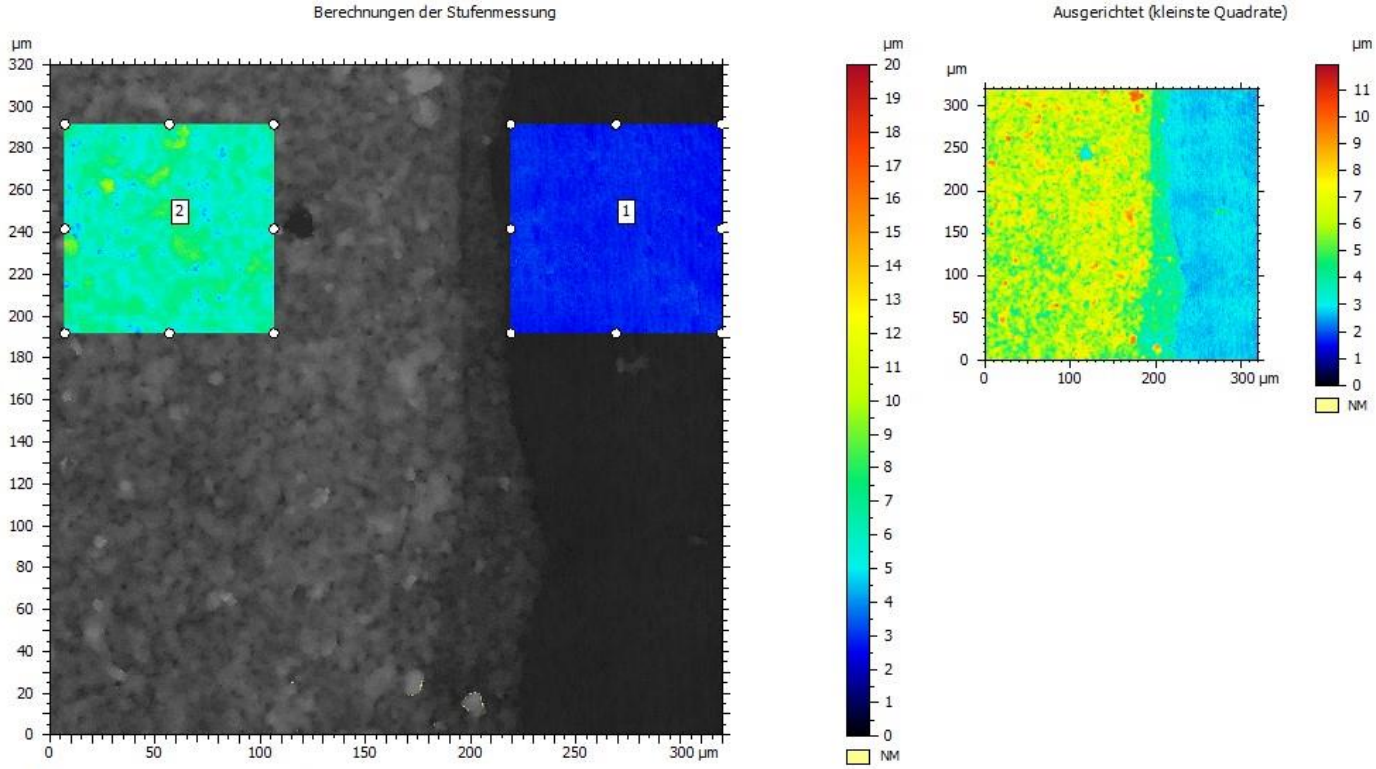

Differenzielle Parameter	Einheit	Wert
Zmean(2) - Zmean(1)	**µm**	**3.52**

Ebenen-Parameter	Einheit	Ebene 1	Ebene 2
Zmin	µm	0.800	2.99
ZMean	µm	2.83	6.35
Zmax	µm	4.32	10.4

F2: Confocal microscopy investigations on carbon-coatings comprised of Super C65 – Super C (SC)

1 Layer

Above

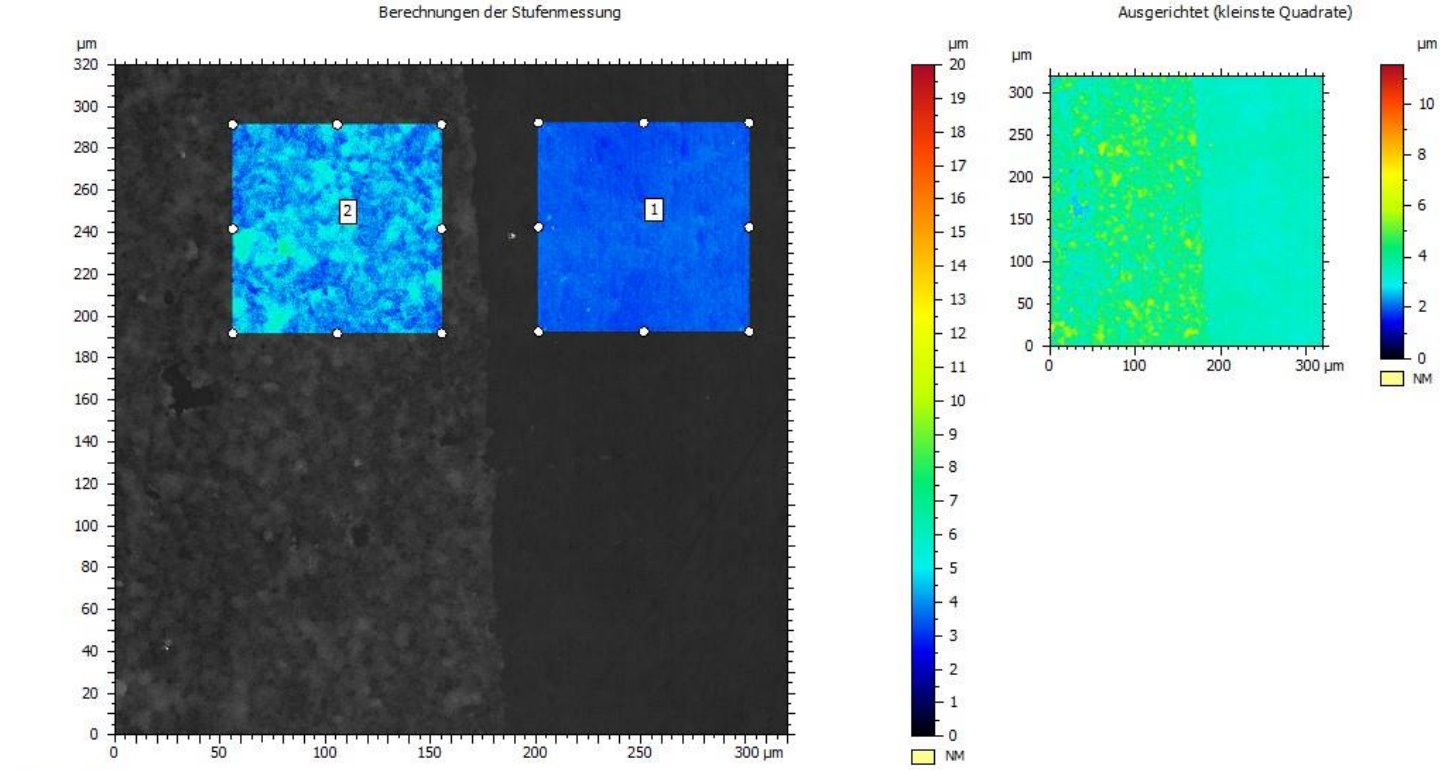

Differenzielle Parameter	Einheit	Wert
Zmean(2) - Zmean(1)	µm	0.850

Ebenen-Parameter	Einheit	Ebene 1	Ebene 2
Zmin	µm	0.673	1.13
ZMean	µm	3.44	4.29
Zmax	µm	5.08	7.82

Center

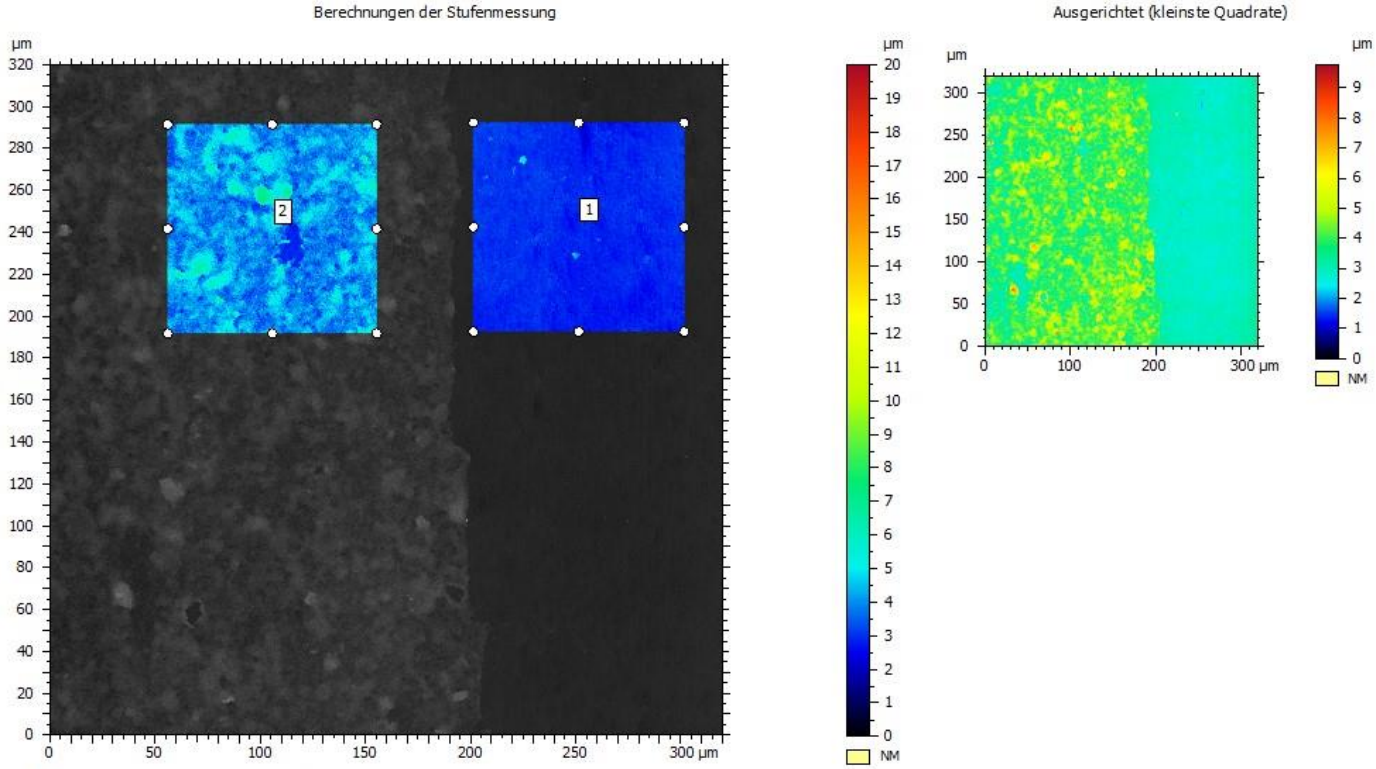

Differenzielle Parameter	Einheit	Wert
Zmean(2) - Zmean(1)	**µm**	**1.27**

Ebenen-Parameter	Einheit	Ebene 1	Ebene 2
Zmin	µm	0.00	0.904
ZMean	µm	2.93	4.19
Zmax	µm	6.10	8.15

5 Layers

Above

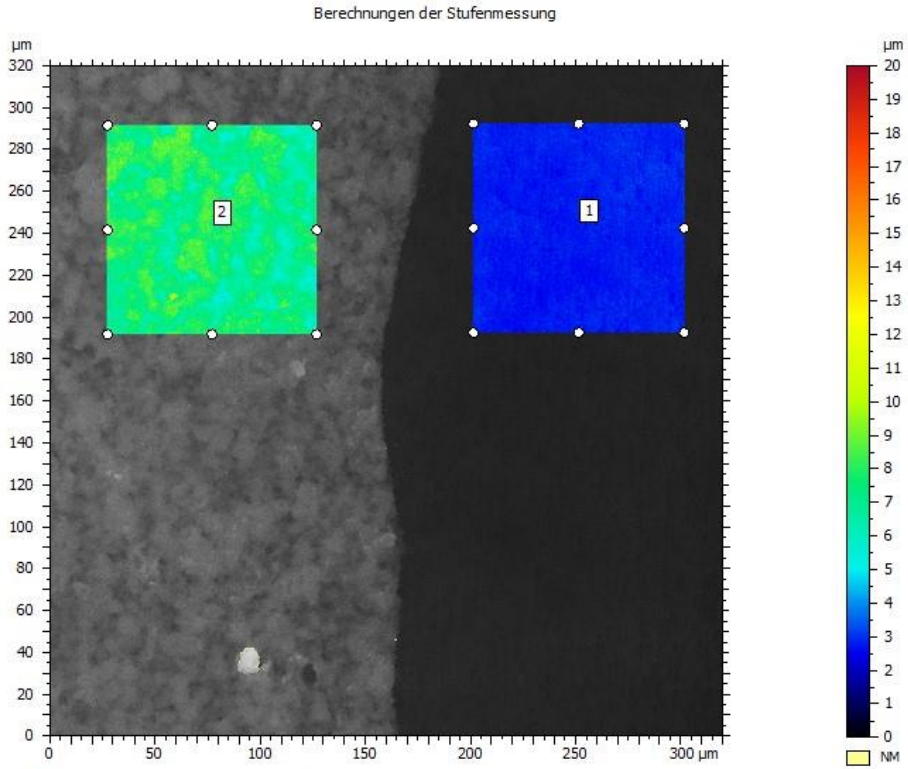

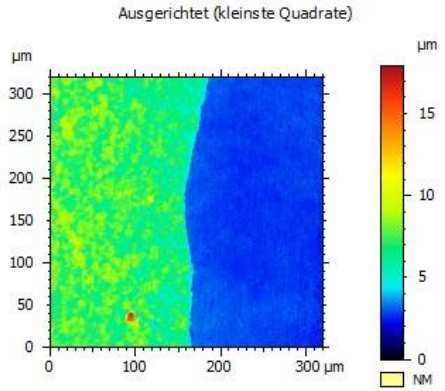

Differenzielle Parameter	Einheit	Wert
Zmean(2) - Zmean(1)	**µm**	**4.53**

Ebenen-Parameter	Einheit	Ebene 1	Ebene 2
Zmin	µm	0.00	4.11
ZMean	µm	2.80	7.33
Zmax	µm	3.56	11.0

Center

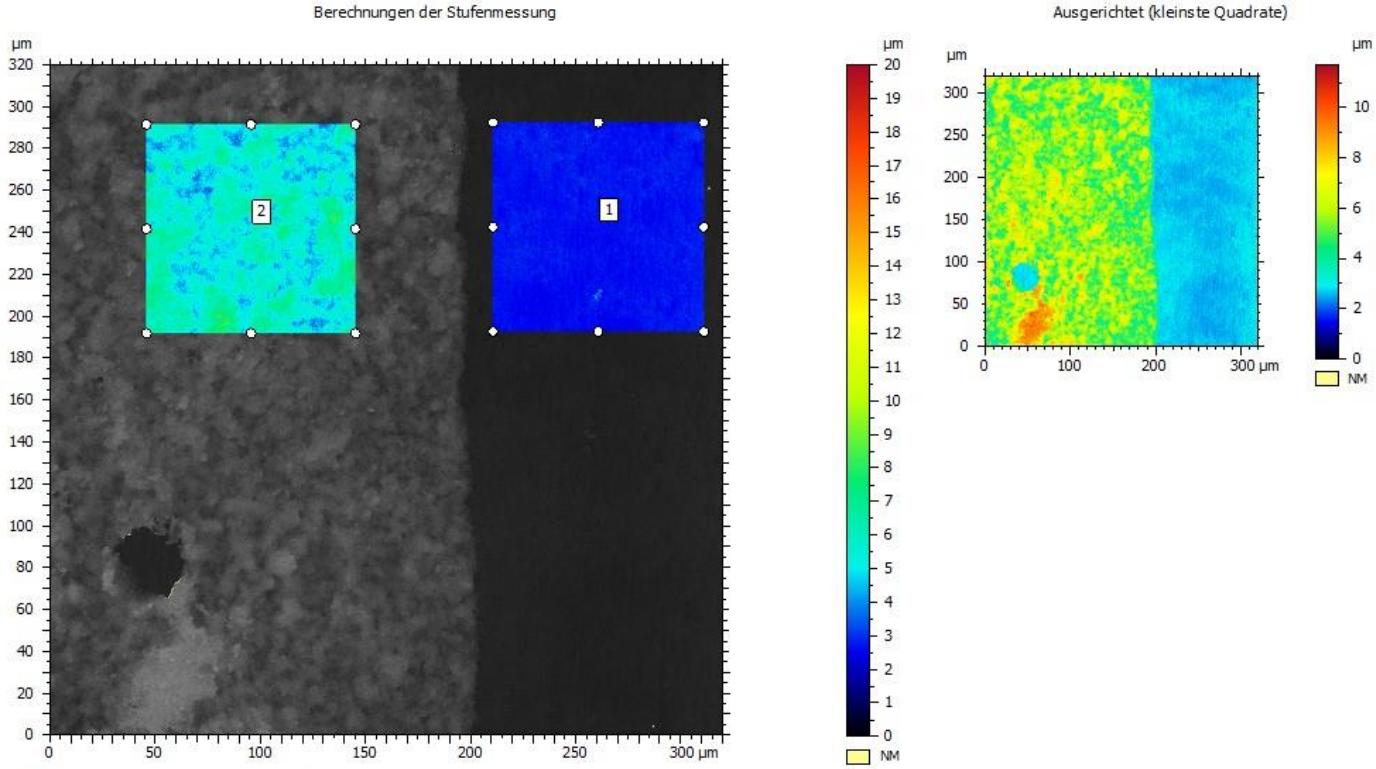

Differenzielle Parameter	Einheit	Wert
Zmean(2) - Zmean(1)	**µm**	**2.87**

Ebenen-Parameter	Einheit	Ebene 1	Ebene 2
Zmin	µm	0.632	2.16
ZMean	µm	2.69	5.56
Zmax	µm	4.89	9.08

Below

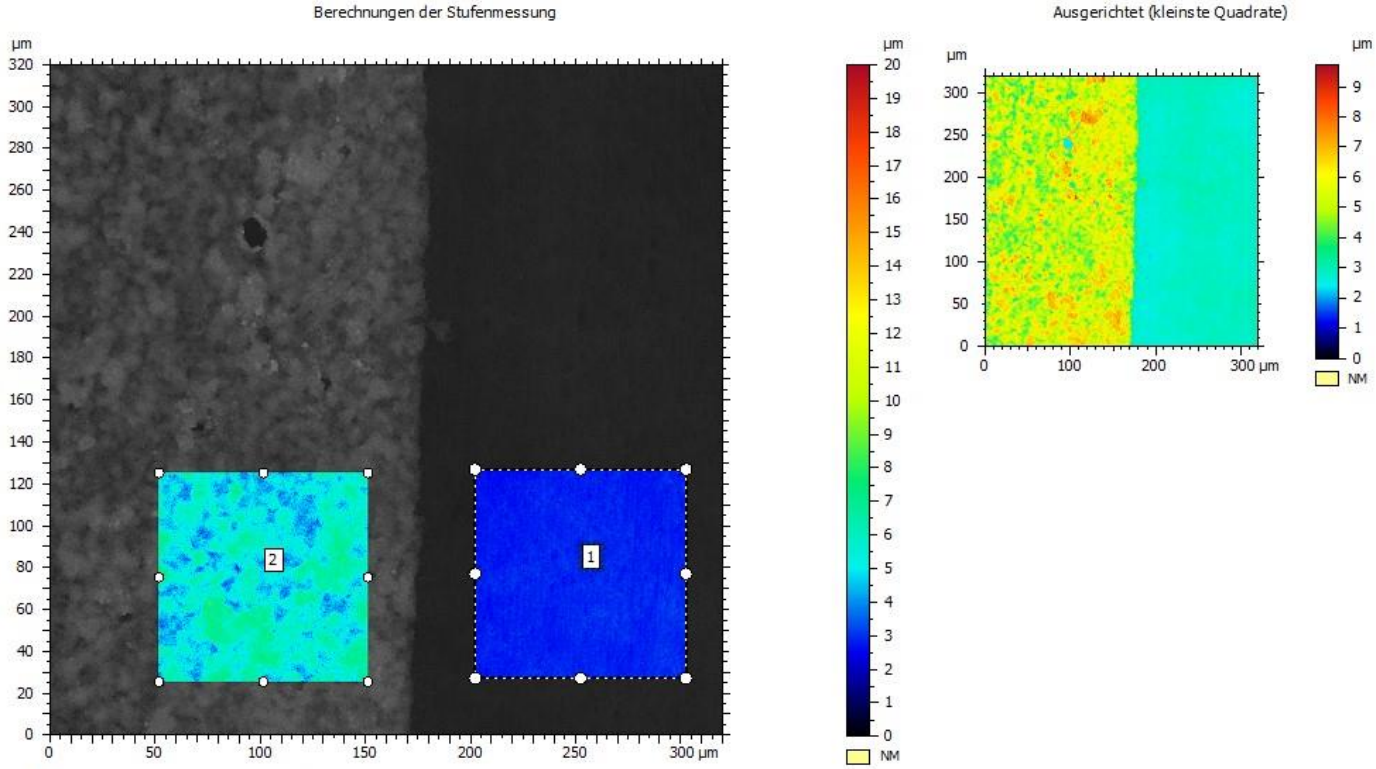

Differenzielle Parameter	Einheit	Wert
Zmean(2) - Zmean(1)	**µm**	**2.59**

Ebenen-Parameter	Einheit	Ebene 1	Ebene 2
Zmin	µm	0.593	1.66
ZMean	µm	2.85	5.43
Zmax	µm	3.64	9.32

10 Layers

Above

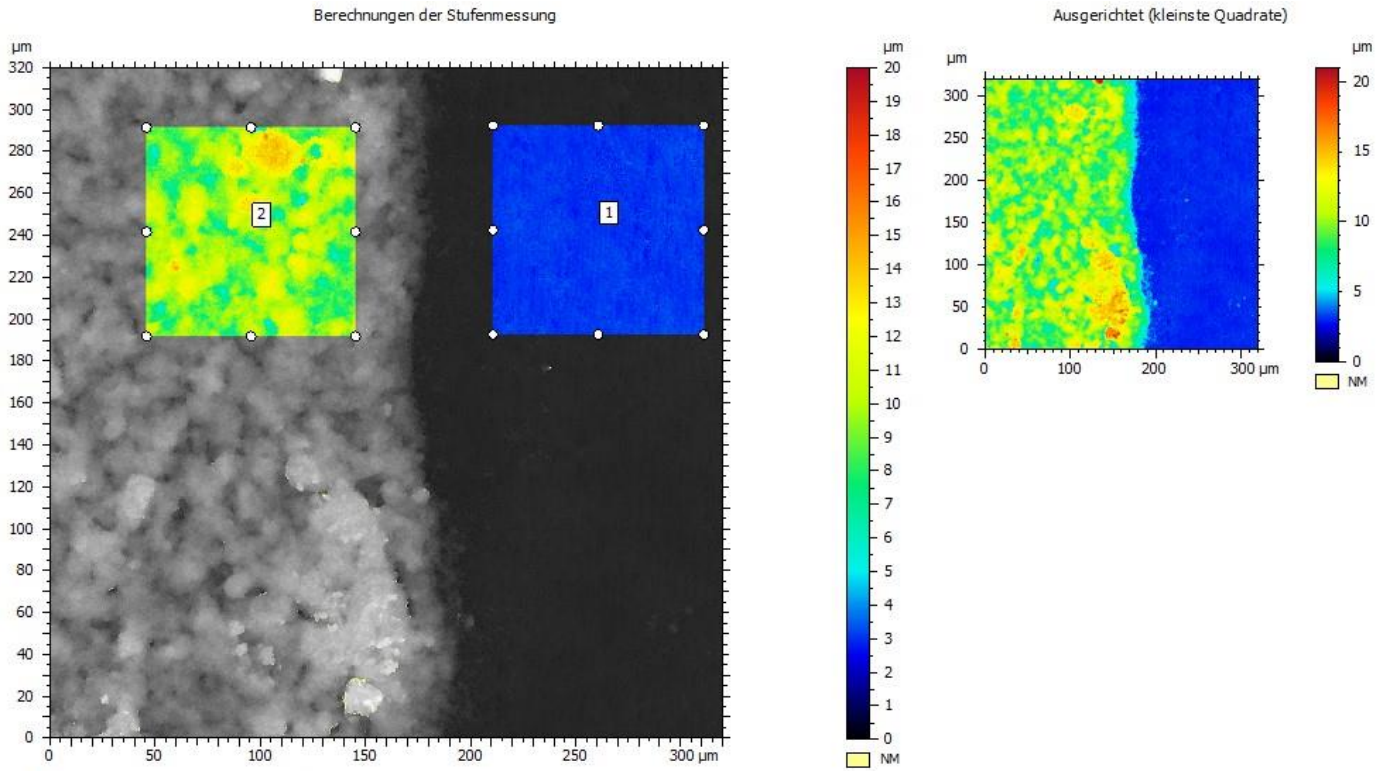

Differenzielle Parameter	Einheit	Wert
Zmean(2) - Zmean(1)	**µm**	**6.70**

Ebenen-Parameter	Einheit	Ebene 1	Ebene 2
Zmin	µm	0.558	3.65
ZMean	µm	3.08	9.78
Zmax	µm	4.44	16.3

Center

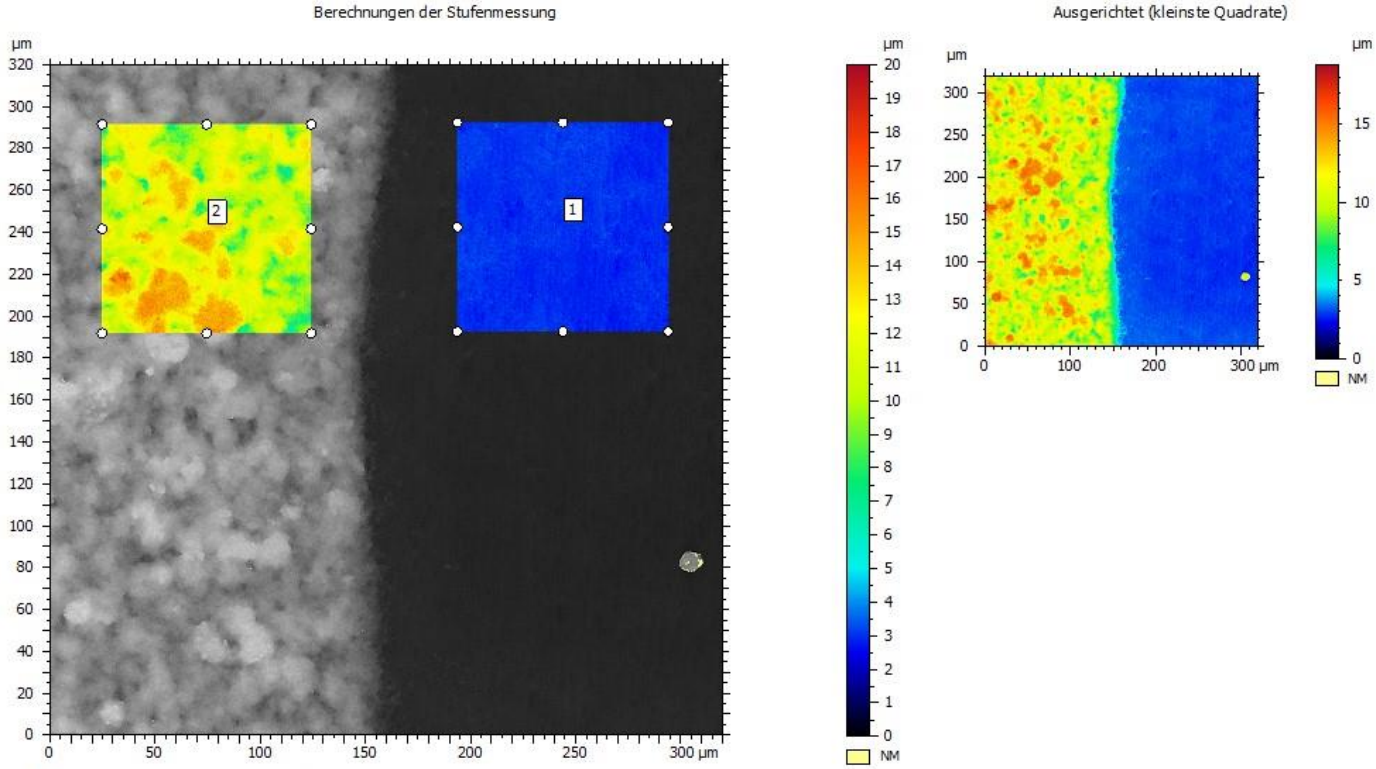

Differenzielle Parameter	Einheit	Wert
Zmean(2) - Zmean(1)	**µm**	**8.58**

Ebenen-Parameter	Einheit	Ebene 1	Ebene 2
Zmin	µm	1.28	4.90
ZMean	µm	2.99	11.6
Zmax	µm	4.03	18.0

Below

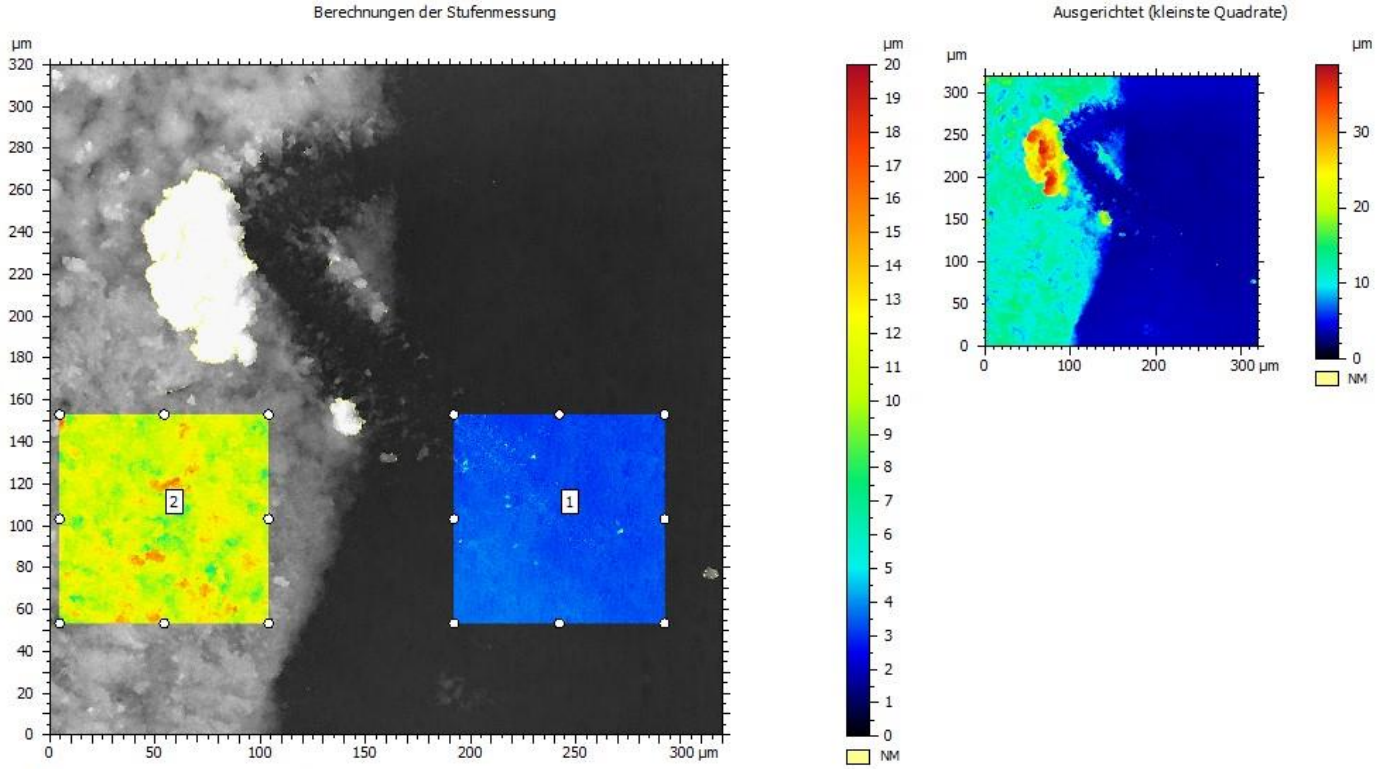

Differenzielle Parameter	Einheit	Wert
Zmean(2) - Zmean(1)	**µm**	**7.85**

Ebenen-Parameter	Einheit	Ebene 1	Ebene 2
Zmin	µm	0.141	6.18
ZMean	µm	3.37	11.2
Zmax	µm	6.90	17.5

F3: Confocal microscopy investigations on carbon-coatings comprised of Nanocyl NC7000 – Multiwalled carbon nanotubes (MWCNT)

1 Layer

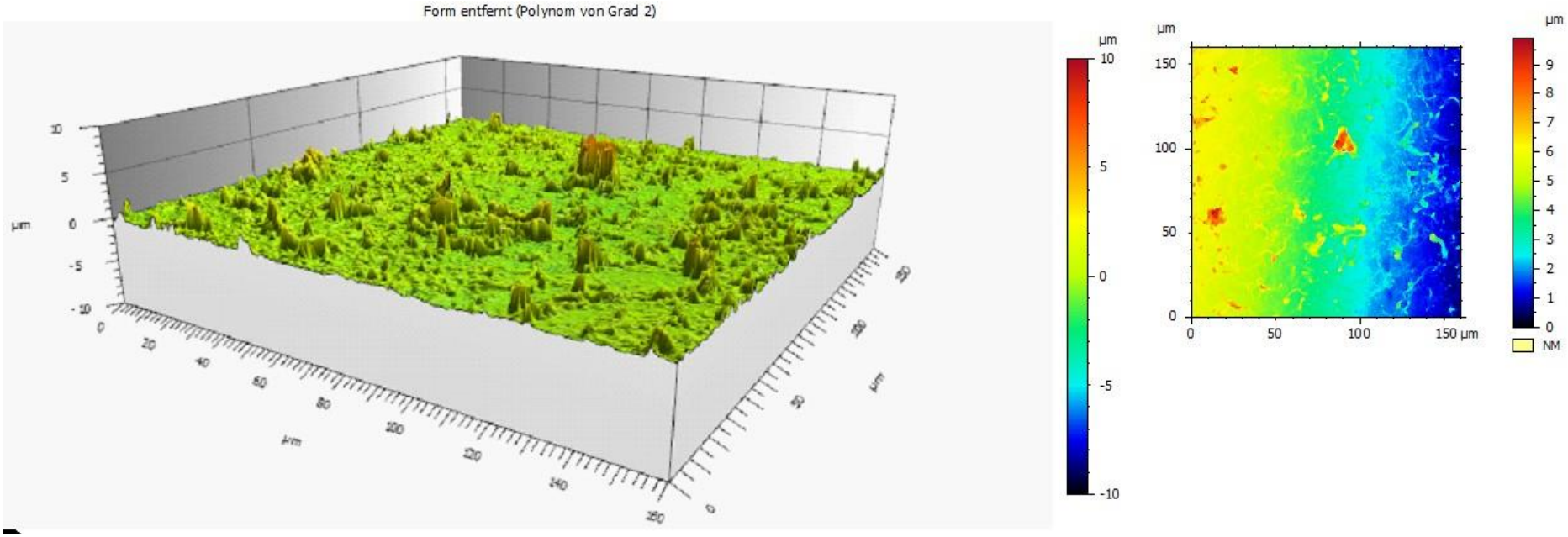

5 Layers

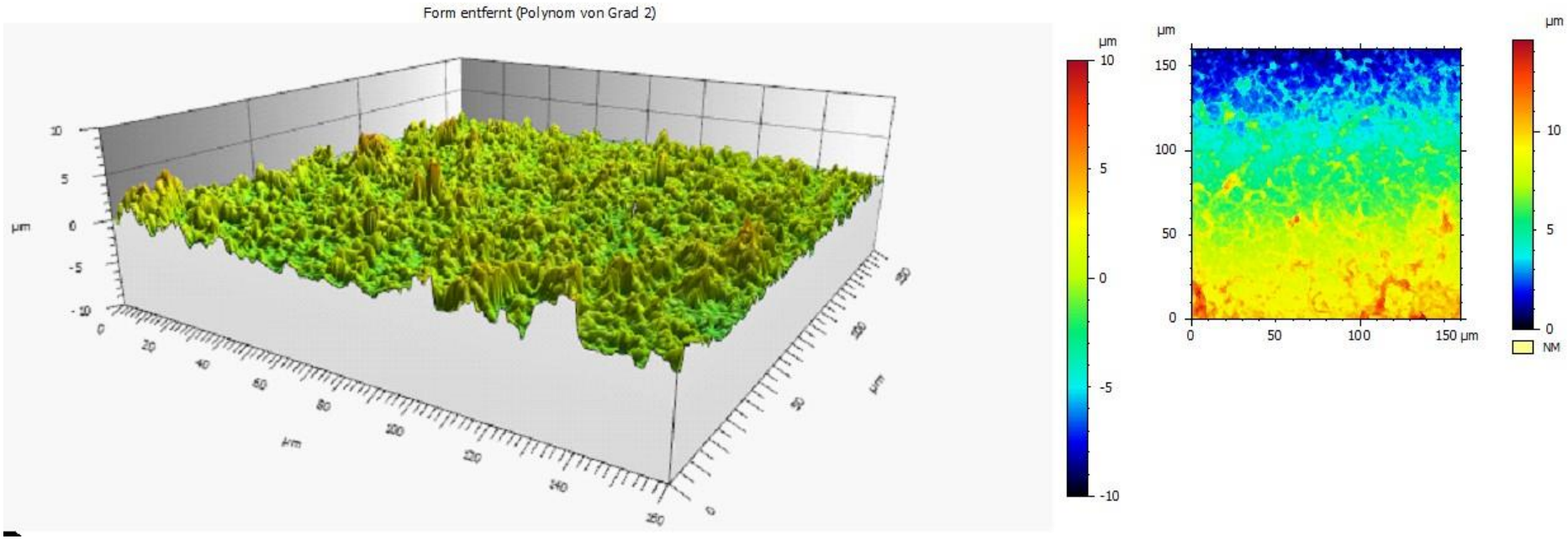
Form entfernt (Polynom von Grad 2)
µm
10
5
0
-5
-10
0
20
40
60
80
100
120
140
160
µm
µm
150
100
50
0
0
50
100
150 µm
µm
10
5
0
NM

10 Layers

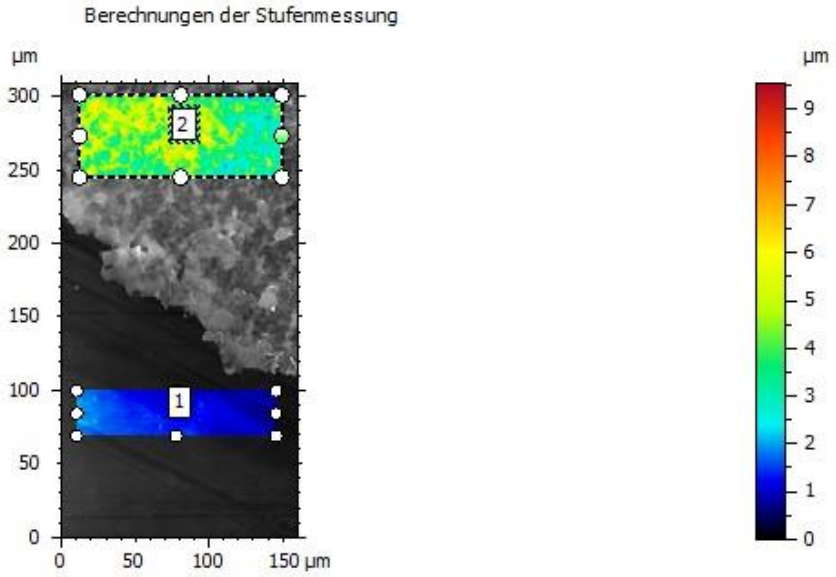

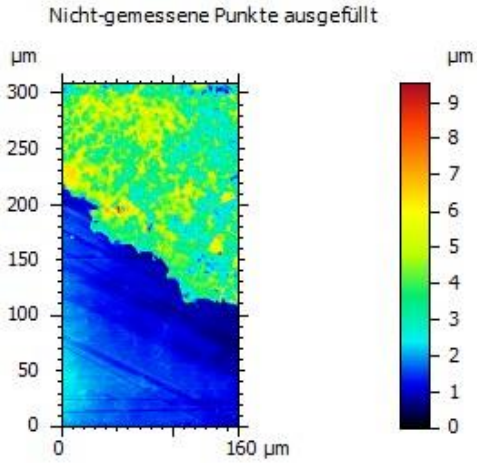

Differenzielle Parameter	Einheit	Wert
Zmean(2) - Zmean(1)	**µm**	**2.82**

Ebenen-Parameter	Einheit	Ebene 1	Ebene 2
Zmin	µm	0.458	1.06
ZMean	µm	1.23	4.05
Zmax	µm	2.25	8.37

G: Datasheets of carbons

G1: Ketjenblack EC-600JD

AkzoNobel

Product Data Sheet

Ketjenblack® EC-600JD

Chemical description	Electroconductive carbon black, pellets	
	CAS No.	: 1333-86-4
	EINECS/ELINCS No.	: 215-609-9
	TSCA status	: listed on inventory
Specifications	Appearance	: Black free-flowing pellets
	Pore volume (DBP)	: 480-510 ml/100 g
	Fines smaller than 125 micron	: 7% max.
	Grit content	: 30 mg/kg max.
	Moisture	: 0.5% max.
	Volatiles	: 1.0% max.
	Iodine absorption	: 1000-1100 mg/g
	Ash	: 0.1% max.
	pH	: 9.0-10.5
	Apparent bulk density	: 100-120 kg/m^3

Storage

AkzoNobel recommends to store *Ketjenblack* EC-600JD in a dry place away from direct sunlight. The packaging can be damaged if exposed to direct sunlight for more than 30 minutes.

When stored under these recommended storage conditions, *Ketjenblack* EC-600JD will remain within the AkzoNobel specifications for a period of at least 12 months after delivery.

Packaging and transport

The standard packaging is 8 kg net in a vented PE bag. The vent consists of a small plastic valve which contains HDPE, NBR and cellulosic parts, which are not readily dispersed during compounding. Due to this we strongly advice not to put the *Ketjenblack* EC-600JD including the bag into the mixing system. A full pallet carries 320 kg net.

Both packaging and transport meet the international regulations. For the availability of other packed quantities contact your AkzoNobel representative.

Ketjenblack EC-600JD is classified as a non-hazardous good according to national and international transport regulations.

Safety and handling

Please refer to the Safety Data Sheet (SDS) for further information on the safe storage, use and handling of *Ketjenblack* EC-600JD. This information should be thoroughly reviewed prior to acceptance of this product.
The SDS is available at www.akzonobel.com/polymer.

Applications

Ketjenblack EC-600JD is a very pure carbon black extremely suitable for antistatic and electroconductive applications. Due to its unique morphology and the extremely high surface area of approx. 1400 m^2/g (BET), only one sixth the amount of *Ketjenblack* EC600-JD is needed compared to conventional electroconductive blacks in order to achieve the same conductivity. The extreme low loading of *Ketjenblack* EC600-JD allows easier processing for those compounds sensitive to filler addition, thus minimizing loss in mechanical and rheological properties.

Ketjenblack EC-600JD when thoroughly dispersed with the polymer significantly increases the conductivity of the resulting compound.

Ketjenblack EC-600JD can be used in all types of polymers, thermoset, thermoplastic as well as elastomers. Due to its unique morphology and structure with very low amounts of *Ketjenblack* EC-600JD excellent conductive material can be made. The loading needed to obtain a certain conductivity can vary significantly per type of polymer. More detailed information is available in the special *Ketjenblack* EC Technical Bulletin.

Ketjenblack EC-600JD has a low ash content, which in addition with the extreme low loading level, makes it an excellent product for semicon applications in cable shielding. The low grit content provides very smooth surface during extrusion.

Ketjenblack EC-600JD can also be used to produce conductive coatings and primers. Also here already at very low loading levels optimal electroconductive performance is obtained, which even more minimizes loss in mechanical and rheological properties compared to *Ketjenblack* EC-300J. With *Ketjenblack* EC-300J about double the amount is needed to obtain the same conductivity

Some other applications are batteries, packaging for IC parts, tubing, flooring, carpet backing, automotive parts, cell phones and many more.

Ketjenblack is a registered trademark of Akzo Nobel Chemicals B.V. or affiliates in one or more territories.

AkzoNobel Polymer Chemistry
Arnhem, The Netherlands
T +31 88 969 2727
E polymerchemistry.nl@akzonobel.com

AkzoNobel Polymer Chemistry
Chicago, U.S.A.
T +1 312 544 7000
T +1 800 828 7929 (Toll free US only)
F +1 312 544 7188
E polymerchemistry.na@akzonobel.com

Akzo Nobel (Asia) Co., Ltd.
Shanghai, PR China
T +86 21 2220 5000
F +86 21 2220 5558
E polymerchemistry.ap@akzonobel.com

www.akzonobel.com/polymer

G2: C-Energy Super C65

IMERYS
Graphite & Carbon

Mobile Energy

HIGH PURITY CARBON BLACKS

C-NERGY™
TIMCAL Carbon Black

C-NERGY™ CARBON BLACKS MEET THE SEVEREST PURITY REQUIREMENTS

Imerys Graphite & Carbon C-NERGY™ carbon blacks match the severest purity requirements for low metallic impurities and grit. The primary purpose of use of these extremely clean carbon blacks is to give electrical conductivity to lithium-ion battery electrodes at low to very low loadings.

KEY FEATURES

Imerys Graphite and Carbon proprietary production process generates the controlled production of extremely clean carbon blacks. Imerys Graphite & Carbon's commitment to continuously improve the purity of its carbon blacks results in a significant reduction of metallic impurities and grit in every new product launched. Reducing contamination and oversize contributes to the reduction of the OCV (open circuit voltage) rejection rate.

Table 1. Properties of Imerys Graphite & Carbon high purity carbon blacks

PROPERTIES	NORMS	UNITS	SUPER PLi	C-NERGY™ SUPER C65	C-NERGY™ SUPER C45
Absorption stiffness value	Int. method 01	ml/5g	32	32	36
BET surface area	ASTM D3037	m^2/g	62	62	45
Ash content	ASTM D1506	%	0.05 max	0.025 max	0.025 max
Grit 45 µm / 325mesh	ASTM D1514	ppm	<2	<2	<2
Grit 20 µm / 625mesh	ASTM D1514	ppm	<15	<10	<10
Metallic (magnetic) impurities	Int. method SEM-EDX	particles in 1 g	0.70 100%	0.12 17%	0.12 17%
Metallic impurities	Int. method XRF	particles in 1 g	0.60	0.30	0.30
Iron	Int. method 20 ICP	ppm	5	1	5
Nickel	Int. method 20 ICP	ppm	<1	<1	<1
Cobalt	Int. method 20 ICP	ppm	<1	<1	<1

Imerys Graphite & Carbon's production process delivers carbon blacks with a unique combination of high structure and low surface area, which guarantees very good dispersion in electrode slurries. Thanks to their lower surface area, C-NERGY™ products exhibit lower moisture pick-up than higher surface area carbon blacks.

In addition, Imerys Graphite & Carbon's production process delivers very graphitic carbon blacks, with a lower number of oxygenated groups on their surface than furnace carbon blacks with the same surface area, making them more hydrophobic and ensuring excellent system stability.

Table 2. Metallic impurities detected by XRF in 150 g of Super PLi and Super C65 (examples).

SPECIES	SUPER PLi	C-NERGY™ SUPER C65
Fe	46	12
FeZn	0	0
FeCu	0	0
FeCuZn	0	0
FeCr	4	0
FeCrNi	0	0
Fe + a (Mn, Co..)	32	23
Cu	0	1
Zn	0	6
Zn + a (Mn, Co..)	10	1
CuZn	2	2
Ti	0	0
Mn	0	0
Co	0	0
MnCoNi	0	0
others	6	12
Total impurity	**100**	**57**

Imerys Graphite & Carbon high purity carbon blacks show the same percolation behaviour in powder mixtures (Fig. 1a) and in electrodes (Fig. 1b), thus they are interchangeable in LIB electrode formulations.

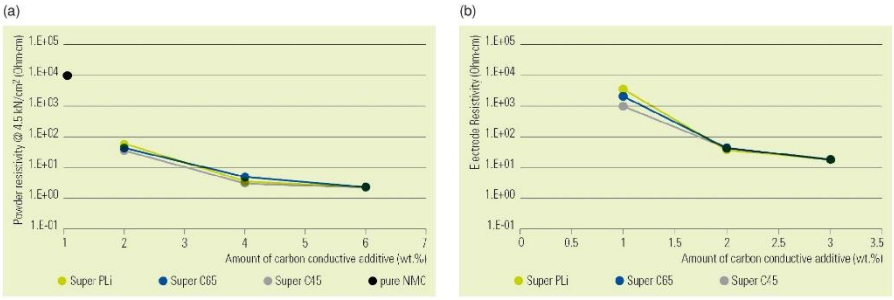

Figure 1. Resistivity of powder mixtures containing NMC active material blended with different amounts of Imerys Graphite & Carbon high purity carbon black (a) and resistivity of NMC based electrodes containing different amounts of Imerys Graphite & Carbon high purity carbon black (b).

Group Head Office • Via Maito 8 • 6804 Bironico • Switzerland
Tel: +41 91 873 20 10 • Fax: +41 91 873 20 19 • graphiteandcarbon.ch@imerys.com
www.imerys-graphite-and-carbon.com

G3: Nanocyl NC7000

nanocyl

THE CARBON NANOTUBE SPECIALIST

Technical Data Sheet: NC7000™| 12th July 2016 | V08

NC7000™

Multiwall carbon nanotubes

General Information

Description

NANOCYL® NC7000™ series, thin multiwall carbon nanotubes, are produced via the Catalytic Chemical Vapor Deposition (CCVD) process.

Key Applications

A primary interest is in applications requiring low electrical percolation threshold such as high-performance electrostatic dissipative plastics or coatings.

Industrial NC7000™ carbon nanotubes are used in various applications in different markets:

- Transportation (Automotive, Aeronautic, Boats)
- Electronics (Electronic packaging, EMI-shielding, sensors)
- Energy (Lithium-ion)
- Industrial applications (Oil&Gas, dynamic rubber parts, coatings, heating elements)
- Sport goods

Benefits

- High electrical conductivity
- Good processability
- Retention of key mechanical properties
- Best cost in use ratio
- High recyclability in thermoplastics
- Cleanliness
- Flame retardancy (synergy in combination with other flame retardants)
- Thermal dissipation
- UV resistance
- Black tinting

1/4

Nanocyl SA

Technical Data

Main Characteristics

NANOCYL® NC7000™ series (Figure 1), thin multi-wall carbon nanotubes, are produced via the Catalytic Chemical Vapor Deposition (CCVD) process.

NC7000™ carbon nanotubes are tube-shaped materials, exclusively composed of carbon atoms, having a nanometric diameter. The graphite layer can be visualized somewhat like a rolled-up chicken wire with a continuous unbroken hexagonal mesh and carbon atoms at the apexes of the hexagons. With action of van der Waals forces, NC7000™ carbon nanotubes have a tendency to cluster into bundles or agglomerates. Consequently, NC7000™ carbon nanotubes look like a black powder. At nanoscale, they have a spaghetti-like structure.

Figure 1. NC7000™ multiwall carbon nanotubes – scale: 100 nm - TEM.

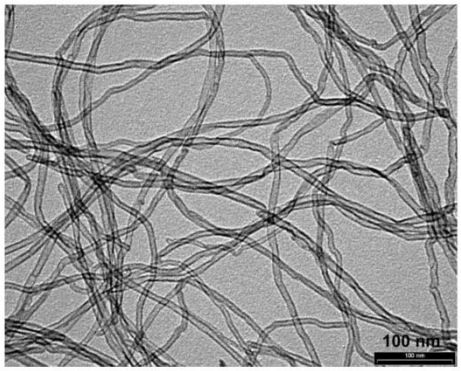

Specific characterization of NC7000™

PROPERTIES	UNIT	VALUE	METHOD OF MEASUREMENT
Average diameter	10^{-9} m	9.5	Transmission Electron Microscopy (TEM)
Average length	µm	1.5	Transmission Electron Microscopy (TEM)
Carbon purity	%	90	Thermogravimetric analysis (TGA)
Transition Metal oxide	%	< 1%	Inductively Coupled Plasma Mass Spectrometry (ICP-MS)
Amorphous carbon	-	*	High resolution Transmission Electron Microscopy (HRTEM)
Surface Area	m^2/g	250-300	BET surface area analysis
Volume resistivity	Ω.cm	10^{-4}	Internal test method (resistivity on powder)

**Pyrolytically deposited carbon on the surface of the NC7000*

Electrical percolation curves for volume and surface resistivity

In thermoplastics, NC7000™ carbon nanotubes bring electrical conductivity with a low percolation threshold between 0.5 wt.% and 4.5 wt.%.

IMPORTANT NOTE: The loading of NC7000™ to achieve a targeted electrical conductivity depends on the dispersion process, the type of polymer (PC, PA, PP, HDPE, etc.) and also of the grade of polymer (viscosity, molecular weight, and so on.)

In general, CNTs are more easily dispersed in polar thermoplastics.

For example, surface resistivity reaches 10^6 [*ohm.sq*] with a 1.5 wt.% of NC7000™ in a specific polycarbonate (Figure 2).

Figure 2. Electrical percolation curve EXAMPLE: polycarbonate (PC) – NC7000™ concentrate. Electrical resistivity measurement in accordance with Nanocyl standard method based on standard injection molded IZOD specimens.

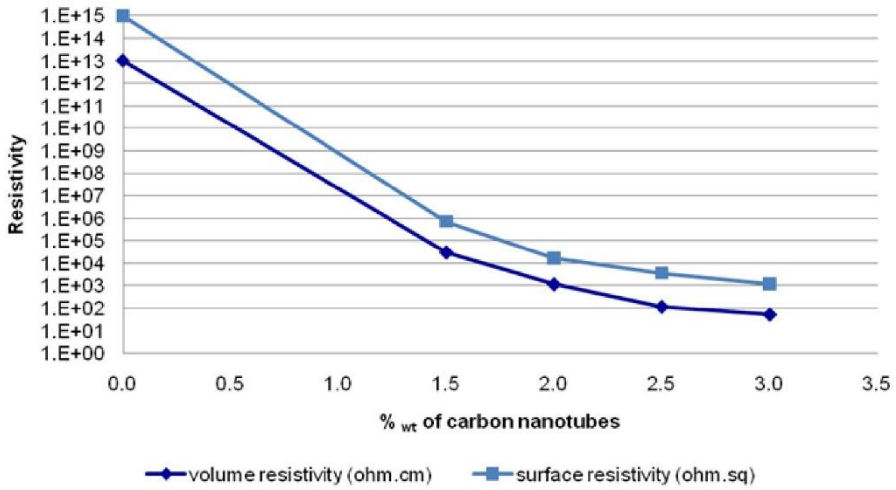

The main advantage of NC7000™ is that they affect less the mechanical properties (e.g. elongation at break) than other conductive fillers such as carbon blacks (CB) or graphite. This is due to the high aspect ratio of NC7000™ resulting in a very low amount of NC7000™ needed to reach a specific conductivity.

NC7000™ increase more the viscosity than CB at equal loading, but the much lower quantities of NC7000™ required render the processing better in most cases or comparable. NC7000™ concentration below 1 wt.% in thermoplastics improves elongation at break and impact resistance without affecting tensile strength and keeping the thermoplastics electrically insulating. NC7000™ in thermoplastics offer additional improvement in cleanliness, thermal dissipation, recyclability, flame retardancy, black tinting and UV resistance.

Commercial/Safety Information

Packaging

NC7000™ carbon nanotubes are available in powder form and are provided in industrial standard 2.5 kg cardboard.
Standard pallet maximum quantity is 90 kg. Standard 40'' container maximum quantity is 1800 kg.

Pre-dispersed forms are also available in various matrices:

- Thermoplastics: PLASTICYL™,
- Epoxy resin: EPOCYL™
- Water dispersion: AQUACYL™
- Elastomers: ELASTOCYL™
- NMP: ORGACYL™.

Minimum Order of Quantity

Nanocyl's minimum order of quantity for NC7000™ is 2.5 kg.

IMPORTANT NOTE: For first technical developments and ease of use in laboratory, 500 g of NC7000™ in a bottle with double caps can be ordered. A fixed price is applied due to additional re-packaging costs of those small quantities (close to the price for 2.5 kg of NC7000™).

Health and Safety

A Material Safety Data Sheets (MSDS) is available to provide both workers and emergency personnel with the proper procedures for handling or working with the NC7000™. This MSDS includes information such as physical data (form and color, melting point, etc.), handling and storage recommendations, first aid measures and ecological information. The Safety Data Sheet is provided with any order and should be observed.

Disclaimer

www.nanocyl.com
info@nanocyl.com
+32 (0)71 75 03 80

Nanocyl SA
Rue de l'Essor N°4
B-5060 Sambreville
Belgium

H: Datasheet of separator (Celgard 2400)

CELGARD

Celgard® High Performance Battery Separators

Celgard is a recognized leader among lithium battery material suppliers, with:

- Unparalleled Product Availability
  Broadest Portfolio in the Separator Industry
- Proven Performance and Reliability
  Over 30 Years of Experience in Separator Design, Manufacturing and Distribution
- Technical Leadership & Expertise
  R&D Teams with Experience in Lithium Battery and Battery Separator Technology
- Strong Global Presence
  Manufacturing Facilities in China, Korea, and the USA;
  Sales and Technical Service Staff throughout Asia, Europe, and North America

Commercial Trilayer Products

Comparison of Typical Properties

Product	2340	2325	C500	C480	2320	C300	C250	C200	C212	M825	M824
Thickness; µm	38	25	25	21.5	20	20	18	17	16	16	12
JIS Gurley; seconds	780	620	515	320	530	560	500	450	435	460	425
Porosity	45%	39%	35%	50%	39%	36%	35%	35%	35%	39%	38%
PP Pore Size; µm	0.035	0.028	0.041	0.038	0.027	0.032	0.032	0.032	0.032	0.026	0.026
TD Shrinkage @ 90° C / 1 hour	0.0%	0.0%	0.0%	0.0%	0.0%	0.0%	0.0%	0.0%	0.0%	0.0%	0.0%
MD Shrinkage @ 90° C / 1 hour	<7.0%	<5.0%	<5.0%	<5.0%	<5.0%	<4.0%	<5.0%	<5.0%	<2.5%	<1.0%	<1.5%
Puncture Strength; grams	>550	>380	>320	>400	>360	>300	>300	>245	>220	>300	>225
TD Tensile Strength; kgf/cm²	165	150	170	140	165	185	175	190	180	150	155
MD Tensile Strength; kgf/cm²	1630	1700	1680	2195	2050	1800	1800	1900	2085	2100	2200

(Continued on Back)

CELGARD

Commercial Monolayer & Specialty Products

Comparison of Typical Properties

	Monolayer PP			Coated PP		Laminated to PP Nonwoven Fabric		Laminated & Coated
Product	2400	2500	A273	3400/ 3401	3500/ 3501	4550 PP/PE/PP	4560 PP	5550 PP
Thickness; laminated film; µm	-	-	-	-	-	110	110	110
Thickness; base film; µm	25	25	16	25	25	38	25	25
JIS Gurley; seconds	620	200	345	620	200	780	200	200
Porosity	41%	55%	40%	41%	55%	45%	55%	55%
PP Pore Size; µm	0.043	0.064	0.039	0.043	0.064	0.035	0.064	0.064
TD Shrinkage @ 90° C / 1 hour	0.0%	0.0%	0.0%	0.0%	0.0%	0.0%	0.0%	0.0%
MD Shrinkage @ 90° C / 1 hour	<5.0%	<5.0%	<3.0%	<5.0%	<5.0%	<7.0%	<5.0%	<5.0%
Puncture Strength; grams	>450	>335	>300	>450	>335	>550	>335	>335
TD Tensile Strength; kgf/cm²	140	135	130	140	135	165	135	135
MD Tensile Strength; kgf/cm²	1420	1055	1600	1420	1055	1630	1055	1055

CONTACT INFORMATION www.Celgard.com

Headquarters
Celgard, LLC
13800 South Lakes Drive
Charlotte, North Carolina
28273 United States
Toll Free (US):
1-800-235-4273
Phone: +1 704-588-5310
Fax: +1 704-587-8585

France
Celgard Sales Office
Daramic SAS
BP 90149
25 Rue de Westrich
Sélestat Cedex
67603 France
Phone: +33 3 89 86 61 02
Fax: +33 3 55 03 59 03

China
Celgard, LLC
Ming Wah Centre
Room #1706
No. 8 Gui Shan Road
Shenzhen
518067 China
Phone: +86 755-2688-7796
Fax: +86 755-2688-7797

Korea
Celgard Korea, Inc.
806-3 Yangcheong-Ri,
Ochang-Eup,
Cheongwon-Gun,
Chungbuk
363-883 Korea
Phone: +82 43-219-2940
Fax: +82 43-219-2605

Japan
Celgard KK
Shinjuku Mitsui Bldg.
27F, 1-1,
Nishishinjuku 2-chome
Shinjuku-ku, Tokyo
163-0427 Japan
Phone: +81 3-5324-3361
Fax: +81 3-5324-3369

A POLYPORE Company

ISO 9001 Certified.
ISO 14001 Certified.

CELGARD products meet the requirements of the EU RoHS directives.

I: Calculation methods

The specific discharge/charge capacities were calculated according to the following equation:

$$Q_{tot} = \frac{i \cdot \Delta t}{m} \quad (1)$$

where Q_{tot} is the specific discharge/charge capacity, in mAh g^{-1}, i is the current imposed, in mA, Δt is the discharge/charge period, in hours, and m is the mass of sulfur, in grams.

The sulfur utilization $S\%$, in percentage, was calculated using the formula below:

$$S\% = \frac{Q_{tot}}{Q_{th,m\ sulfur}} \cdot 100 \quad (2)$$

where $Q_{th,m\ sulfur}$ is the theoretical specific capacity, 1675 mAh g^{-1}.

For the quantification of the upper and lower plateaus discharge capacities, the potential profile at discharge was analyzed. As observed in Figure 1, the point of transition between the upper and lower plateaus is identified by a corner. To find the instant where the transition occurs, the potential derivative in function of time dV/dt was calculated, with the following equation:

$$\frac{dV}{dt} = \frac{V_{t+1} - V_t}{t_{t+1} - t_t} \quad (3)$$

where V_{t+1} and V_t are the potential at the instant $(t+1)$ and (t), in volts, while t_{t+1} and t_t are the instants.

The instant where dV/dt is zero corresponds to the transition between the upper plateau and the lower plateau, which also corresponds to the discharge time of the upper plateau. Knowing this value, it is possible to calculate the upper plateau discharge capacity, with Eq. 1.

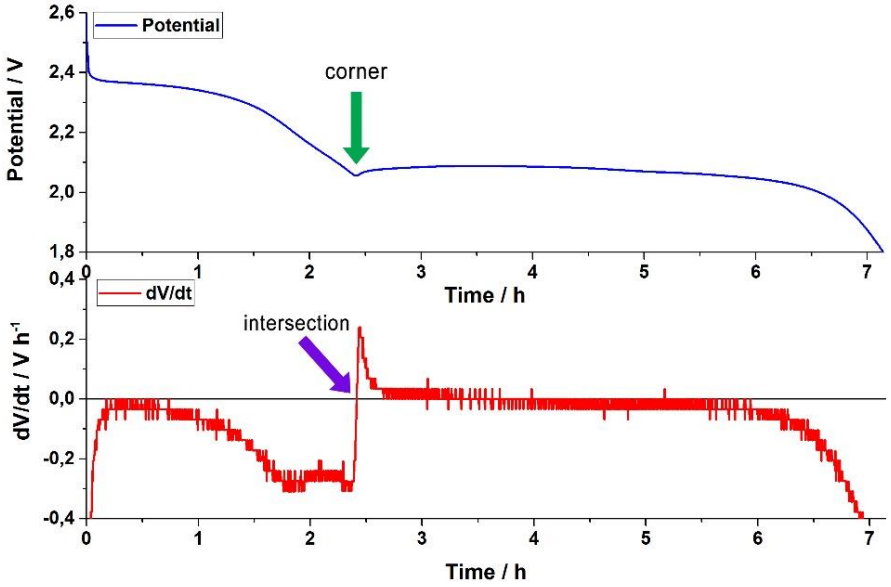

Figure 1 – Potential profile, at discharge, of a Li-S cell, and corresponding potential derivative. The green arrow points to the corner, the transition point between the upper and lower plateau, and the purple arrow shows the intersection point.

Since the sum of the upper and lower capacities equals the total capacity, it is possible to calculate the lower plateau discharge capacity with the following formula:

$$Q_L = Q_{tot} - Q_H \quad (4)$$

The upper plateau contribution was calculated according to the equation below:

$$Q_{H,contribution} = \frac{Q_H}{Q_{H\ th,m}} \cdot 100 \quad (5)$$

where $Q_{H\ th,m}$ is the theoretical discharge capacity of the upper plateau, 419 mAh g^{-1}.

The lower plateau contribution was calculated with the following formula:

$$Q_{L,contribution} = \frac{Q_L}{Q_{L\ th,m}} \cdot 100 \quad (6)$$

where $Q_{L\ th,m}$ corresponds to the theoretical discharge capacity of the lower plateau, 1256 mAh g^{-1}.

J: Detailed experimental protocol for production of Langmuir-Blodgett Carbon Films, using the Langmuir-Blodgett Scooping method

Langmuir-Blodgett Carbon Films

Brief introduction

Herein will be presented two methods to produce carbon-coated separators. The first method was developed by Kim *et al.* [1], where the injection of the suspension on the water's surface is performed manually, while in the second method the suspension's injection is performed with a syringe pump, which produces a constant flow rate. The materials and equipment are listed below.

Section		Material	Equipment
Preparation of the **substrate**	1.1	Glass plate Kapton tape Separator (Celgard 2400)	Tweezers Stainless steel template
Preparation of the **suspensions**	1.2	Ketjenblack EC-600 JD (Akzonobel) Super C65 (Imerys Graphite & Carbon) Nanocyl NC 7000 (Nanocyl) Pure ethanol (Chemsolute®, 99,9%)	Glass flasks Ultrasonic bath (Bandelin Sonorex) Ultra-Turrax (T 10 basic Ultra-Turrax)
Cleaning of the **container**	1.3	Acetone Detergent Ultra-pure de-ionized water (5,5 μS m^{-1})	Sponge Crystal dish (Ø ext: 140 mm; Heigh: 75 mm; Capacity: 900 mL; VWR 216-0074)
Preparation of the sample before deposition of carbon **layer**	1.4	Isopropanol Deionized water	Plastic tweezer
Carbon layer **deposition**	2.1.1	Manual: Suspension prepared in section 1.2	Pasteur pipette
	2.1.2	Automatic: Suspension prepared in section 1.2	Syringe pump (Duratec, Nano Pump-Mini)
Drying **step**	2.2		Hot plate
Further **coating**	2.3	Same as 1.3, 1.4, 2.1 and 2.2	
Storage of carbon coated separator	3	Plastic bag	Tweezers Scissor

1. Preliminary preparation steps

In the following sections will be described the necessary steps to prepare the substrate, the requirements to make a proper suspension to produce LB carbon films, the techniques necessary to disperse the carbon nanoparticles and the wetting stage of the separator to make the carbon film to adhere. It is important to always use disposable gloves, a face mask, safety glasses and lab coat. Work always inside the fume hood when proceeding with the carbon coatings.

1.1. Preparation of the substrate

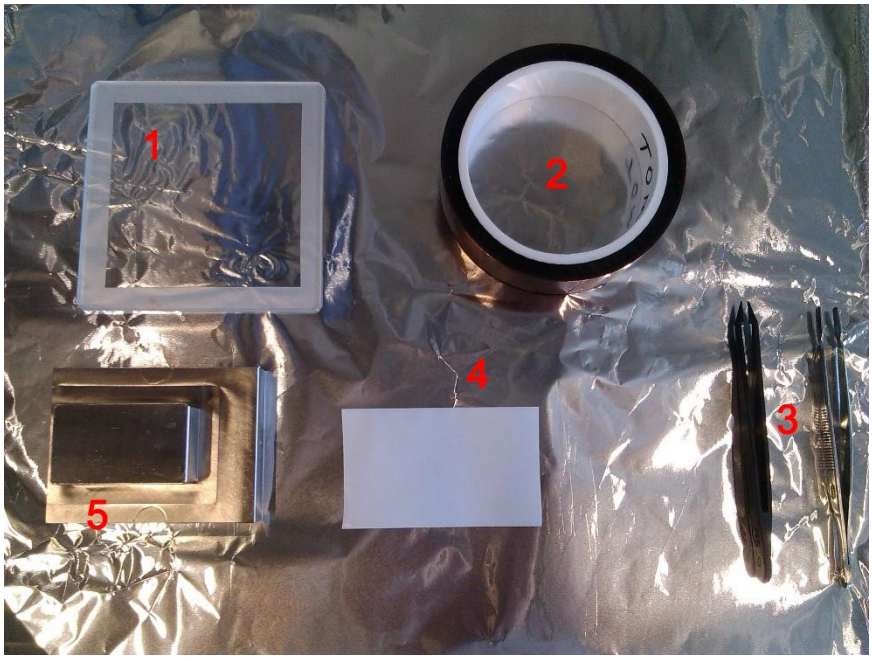

Figure 1 – Materials necessary for the preparation of the substrate: (1) glass plate, (2) Kapton tape, (3) tweezers, (4) separator and (5) stainless steel template.

Before starting, it is essential to wash the glass plate, the tweezers and the stainless steel template, to make sure that no impurities or substances are on the surface. Wash the glass plate and the stainless steel template with a sponge and detergent, and afterwards rinse the surfaces with acetone. To clean the tweezers, rinse ethanol and afterwards clean with clean paper towel. While drying, prepare a clean working place by placing multiple paper towels on a flat surface.

Figure 2 – Position of the separator on the glass plate.

Cut a separator in a piece of approximately 5.0×7.5 cm^2 and place it on the glass plate. Save some space between the ends of the glass plate and the separator to be able to tape, as shown in Figure 2.

It was found that if free spaces are between the separator and the glass plate, solvents can fill those spaces and can corrupt the LB film formation process on the surface of the water. To make sure that no free spaces are between the separator and the glass plate, put a stainless steel template, or any object with a flat surface, on top of the separator. Then, cut four pieces of Kapton tape and with the tweezers, carefully place them on the corners of the separator, as shown in Figure 3.

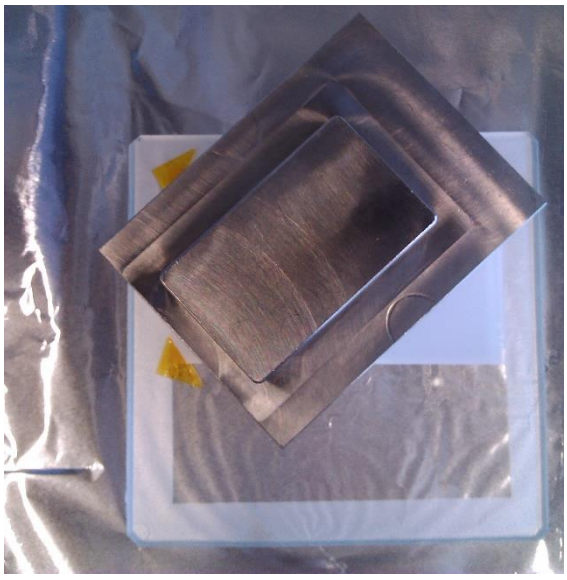

Figure 3 - Taping the corners of the separator with Kapton tape.

Figure 4 – Prepared substrate.

The substrate should look like in Figure 4.

1.2. Preparation of the suspensions

The suspensions used to produce LB carbon films are a mix of pure ethanol and carbon nanoparticles. In Table 1 are listed the ideal carbon content of each carbon nanoparticle, necessary to produce proper suspensions to create LB carbon films. In Table 2 are listed the mass of carbon nanoparticles and volume of pure ethanol necessary to produce an ideal suspension of carbon nanoparticles. The mass of carbon nanoparticles was calculated according to Eq. (4.1) in the Appendixes.

Table 1 – Ideal carbon content necessary to produce proper suspensions for LB carbon films.

Carbon	**wt. %**
Ketjenblack EC-600 JD (Akzonobel)	0.1
Super C65 (Imerys Graphite & Carbon)	0.35
Nanocyl NC 7000 (Nanocyl)	0.1

Transfer a glass flask into the fume hood and pour the carbon nanoparticles inside it. Some carbons which come aggregated in pellets, such as Ketjenblack, need to be gently grinded with a mortar and a pebble before added to the glass flask. Afterwards, add pure ethanol into the flask with a graduated pipette.

Figure 5 – Bath sonicator with immersed flask.

The next step is the ultrasonication of the mixture. Place the flask in a disposition which the water level of the oscillating tank matches the level of the mixture inside the flask, as shown in Figure 5. Turn on the bath sonicator and let the mixture sonicate for 15 minutes.

From experimental results, it was confirmed that after ultrasonication the carbon nanoparticles tend to agglomerate. Therefore, to pull agglomerates apart, another dispersing mechanical method is used, which induces high-shear mixing, such has Ultra-Turrax. The high acceleration acting on the material produces extremely strong shear forces, managing to decrease the size of the agglomerates.

Figure 6 - Mixing device used to produce high-shear mixing of the suspension.

Figure 7 - High-shear mixing of the suspension with Ultra-Turrax.

Before mixing the suspension, wash the moveable parts of the Ultra-Turrax with isopropanol and let them dry on a paper towel. Afterwards, assemble the dispersing tool. Start by connecting the main plug, immerse the shaft inside the glass flask, 10 mm from the flask bottom and 20 mm in the suspension to prevent splashing, and adjust the wheel scale to magnitude 4. Switch on the device and let mix for 30 seconds. After finishing, close the flask and proceed with the cleaning of the moveable parts of the mixing device. Switch off the device, disconnect from the main plug, disassemble the moveable parts, wash them with isopropanol and store them in clean paper towel.

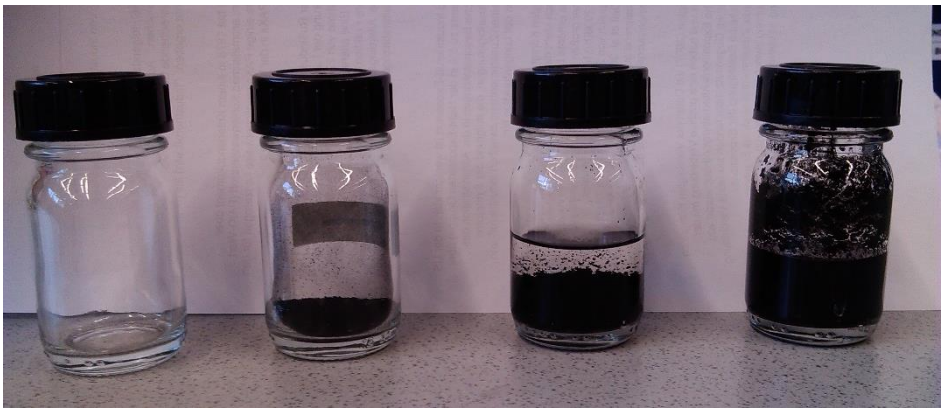

Figure 8 – Empty flask, flask with carbon nanoparticles, flask with mixture of carbon nanoparticles and pure ethanol and flask with mixture after bath sonication and high-shear mixing with Ultra-Turrax (from right to left).

1.3. Cleaning of the container

Vigorously wash the crystallizing dish with a sponge and detergent, and remove the foam with abundant water. Afterwards rinse the surface with acetone and pass plenty of water. Then, fill the container with ultra-pure de-ionized water until the water level reaches the near end, as shown in Figure 11, and transfer to the fume hood where the coating process will be performed.

Figure 9 – Material necessary for cleaning the crystallizing dish: (1) detergent, (2) acetone and (3) crystallizing dish.

Figure 10 – Washing steps of the crystallizing dish: (1) wash the inner surface of the crystallizing dish with detergent and sponge, (2) rinse the inner surface of the crystallizing dish with acetone and (3) take the acetone with de-ionized water.

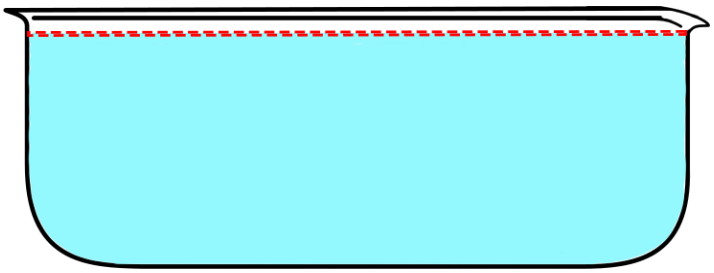

Figure 11 - Water level (marked on red) on crystallizing dish for proper production of LB carbon film.

1.4. Preparation of the sample before deposition of carbon layer

Wash the substrate produced in section 1.1 with de-ionized water to flush impurities and afterwards rinse it with isopropanol, to make the LB carbon film adhere the separator. Then, take the excess of isopropanol with abundant water. If this last step is not well performed, the remaining isopropanol on the substrate can lead to the corruption of the LB carbon film while

being formed on the surface of the water. Afterwards, transfer the wet substrate to the crystallizing dish, as shown in Figure 15.

Figure 12 – Material necessary for the preparation of the sample before deposition of carbon layer: (1) plastic tweezer, (2) isopropanol and (3) substrate prepared in section 1.1.

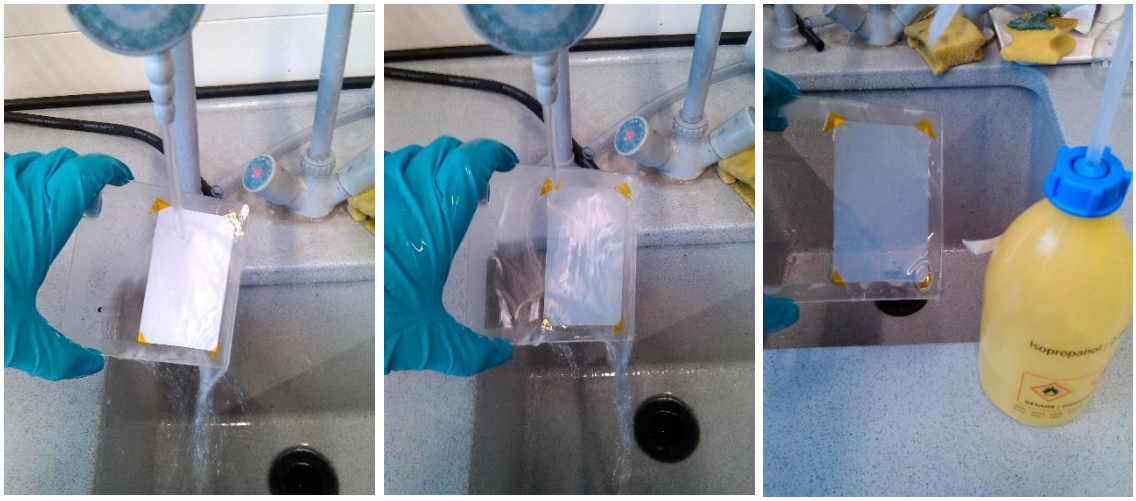

Figure 13 – Washing and wetting of the substrate before coating: (1) washing with de-ionized water, (2) wetting with isopropanol and (3) taking the excess of isopropanol with abundant water.

Figure 14 – Prepared substrate before the coating step.

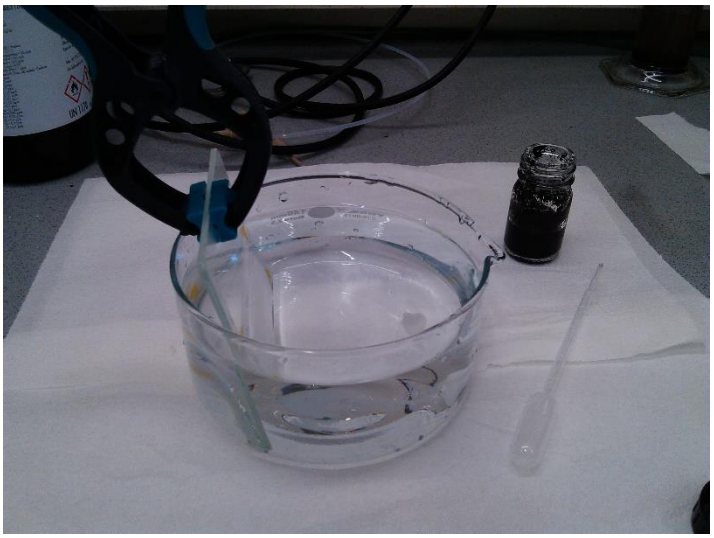

Figure 15 – Filled crystallizing dish with ultra-pure de-ionized water and prepared substrate for coating.

2. Layer-by-layer assembly

2.1. Carbon layer deposition

Two approaches were used for the injection of the suspension - manual injection, by using Pasteur pipette, and automatic injection aimed by a syringe pump. In the first one, the injection of the suspension is controlled manually, which could lead to defective LB carbon layers. The second method produces a constant injection of the suspension, leading to stable and homogeneous LB films. In Figure 16 are displayed two carbon coated separators with the two injection approaches.

Figure 16 – Super C65 (0,35 wt. %) coatings on separator using a syringe pump (left) and Pasteur pipette (right).

2.1.1. Manual injection

Fill the Pasteur pipette with the suspension and lean the tip of the pipette on the inner wall of the crystallizing dish, near the water's surface. Then, inject constantly the suspension, until 2/3 of the

surface is saturated with nanomaterial. Slowly rise the substrate and at the same time move the substrate in the opposite direction of the dispersion of the nanomaterial. While pulling up the substrate, constantly inject the suspension, to maintain the nanoparticles closely packed. This explanation is schematized in Figure 18.

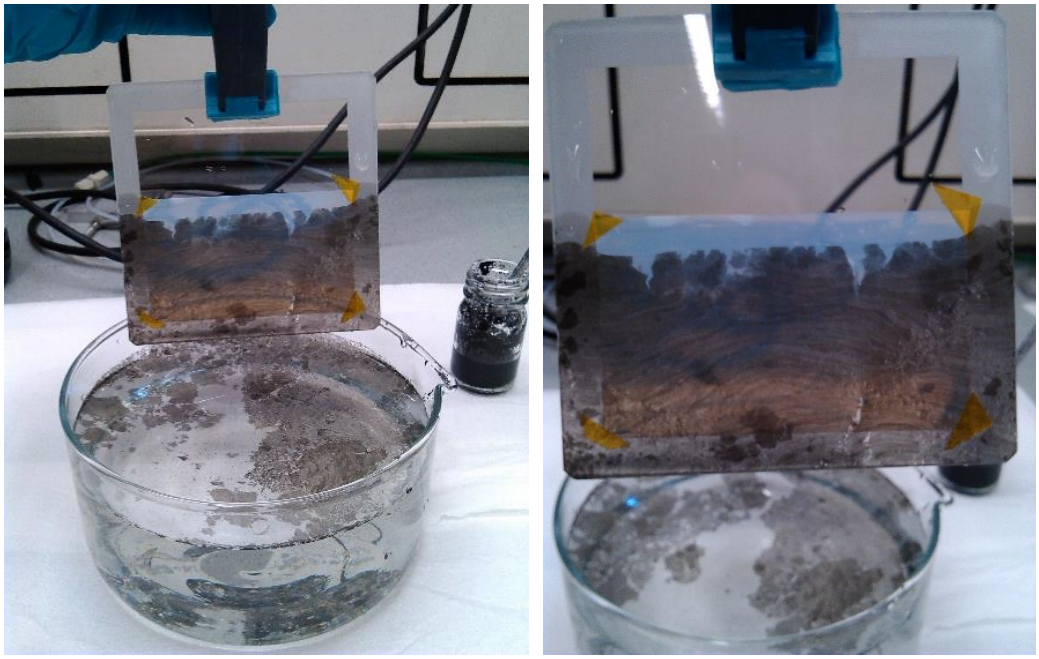

Figure 17 – Substrate after coating process

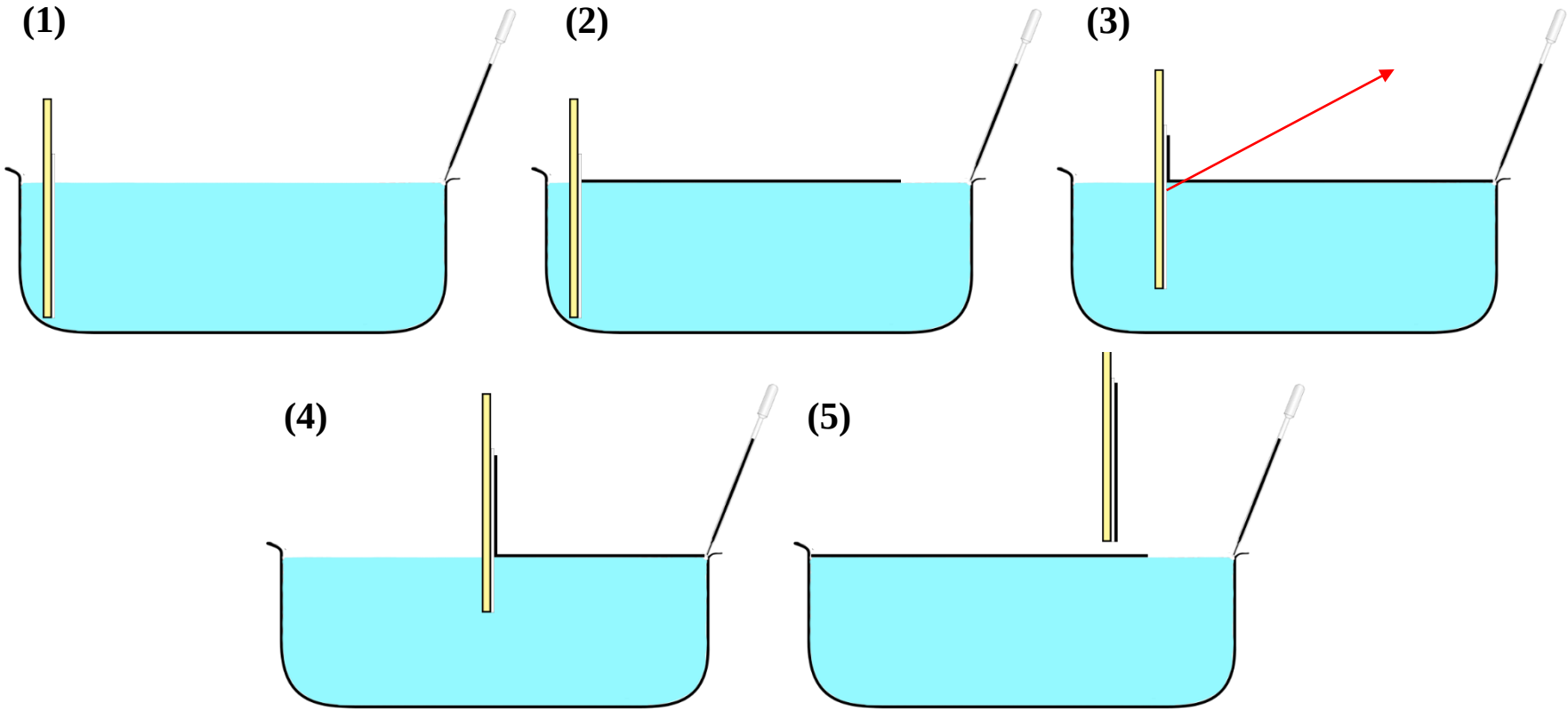

Figure 18 – Carbon coating procedure: (1) fill the Pasteur pipette with the suspension and lean the tip of the pipette on the inner wall of the crystallizing dish, near the water's surface; (2) inject constantly the suspension, until 2/3 of the surface is saturated with nanomaterial; (3), (4) & (5) Slowly pull up the substrate and move the substrate against the direction of the dispersion of the nanomaterial, as shown by the red arrow. While rising the substrate, constantly inject the suspension, to maintain the nanoparticles closely packed.

2.1.2. Automatic injection

Check if the power-switch is in the "Off" position and then plug-in the power cord. Connect the Bluetooth adapter to the I/O-Port, switch on the adapter and turn on the mobile interface. If necessary, charge the mobile device. Mount the fill tubing at the Y-manifold (inlet) and the dispense tubing at the Y-manifold (outlet) and fix the tubes with a support. To initialize the pump, turn the power-switch in the "On" position, set the toggle switch to upper position "Init", and wait until the syringes have moved. Then set the toggle switch to the lower position "Prime" and wait until the syringe drives has done about 3/4 of their way down. Then switch to the intermediate position to stop. Unpack the 250 µl syringes and wet the plungers with ethanol. Insert the plunger into the syringe. Twist the Luer connecter of the syringe into the valve and pull the plunger out and fix to the thumbscrew. Put the end of the inlet fill tubing into a cup with ethanol and the outlet dispense tubing into an empty cup. Set the toggle switch to the lower position "Prime" to let the ethanol flow through the tubbing system into the empty cup, to clean the tubes. After 5 minutes, take the fill tubing out of the cup with ethanol and wait until all the solvent gets out of the tubbing system. Then, put the inlet fill tubing inside the flask with the suspension and set the toggle switch to the intermediate position right after the suspension fills all the tubing system. Lean the tip of the outlet dispense tubing on the inner wall of the crystallizing dish, near the water surface, and immerse the substrate (Figure 19), as prepared in section 1.4. Then, select on the mobile interface the flow rate 1000 µl min^{-1}, and press "start" to inject the suspension. After 2/3 of the water surface is saturated with the nanomaterial, slowly rise the substrate and at the same time move the substrate in the opposite way of the dispersion of the nanomaterial, as described in Figure 18. When the substrate gets coated, press "pause" to stop the injection.

Figure 19 - Carbon coating process with automatic injection.

2.2. Drying step

After coating the substrate, transfer it to a hot plate and let it dry for 1 minute at 70 ºC, as shown in Figure 20. You will notice that the separator is drying when the uncoated area gets whiter. Afterwards, place the substrate on a paper towel and let it cool down.

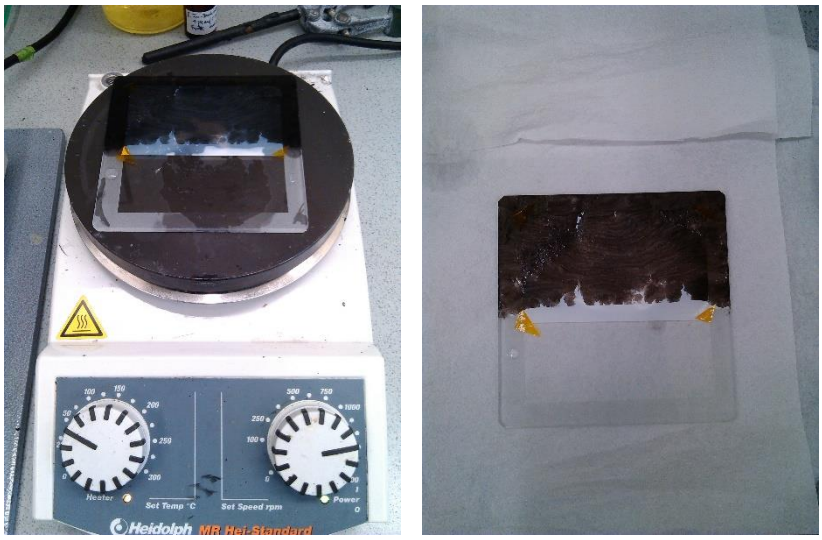

Figure 20 – Drying step of substrate after coating.

2.3. Further coating

To coat multiple layers with Pasteur pipette, repeat the steps in sections 1.3, 1.4, 2.1.1 and 2.2.

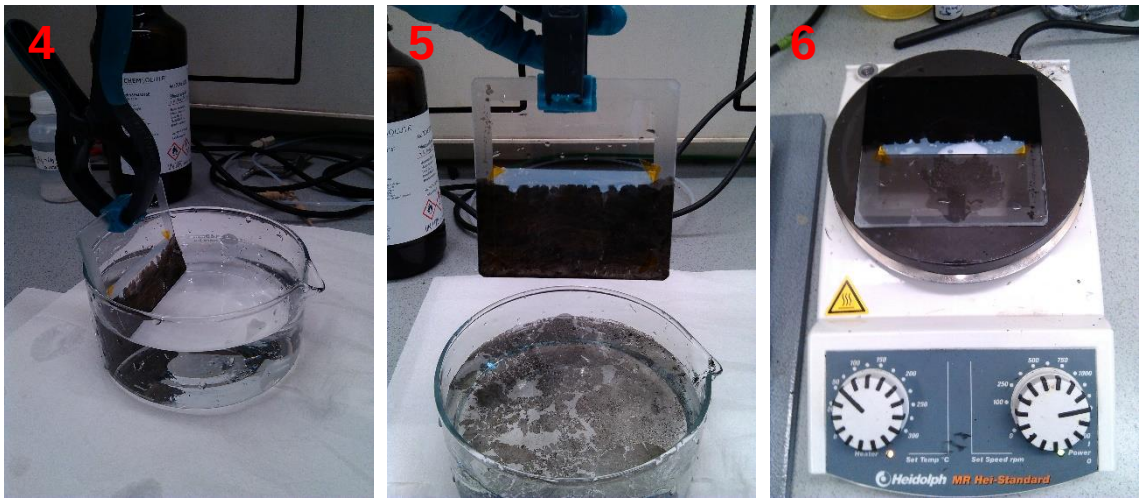

Figure 21 – Layer-by-layer coating with manual injection: (1) washing the previously coated separator with de-ionized water, (2) wetting with isopropanol and (3) taking the excess of isopropanol with abundant water. (4) Immersed wet carbon-coated separator in filled crystallizing dish with ultra-pure de-ionized water, (5) two layer coated separator and (6) drying step of the carbon-coated separator.

Figure 22 – Two layer carbon-coated separator.

If the coating is done with the syringe pump, repeat the steps in sections 1.3, 1.4, 2.1.2 and 2.2. In this case, since the syringe pump is filled with the suspension, put the tip of the outlet dispense tubing on the inner wall of the crystallizing dish, near the water's surface and immerse the prepared carbon coated substrate. Press "Continue" on the mobile interface, to proceed with the injection.

After finishing the coatings using the syringe pump, it is necessary to clean the tubbing system. Close the glass flask with the suspension, and replace it with a cup filled with ethanol. Press "Stop" on the mobile interface and set the toggle switch to the lower position "Prime" and let the ethanol flow through the tubing system until the effluent is colorless. Then, take the inlet fill tubing out of the cup and let all the ethanol flow out of the device. Set the toggle switch to the intermedium position, turn off the device and disconnect from the plug. Clean all the surfaces of the device with a paper towel soaked in ethanol.

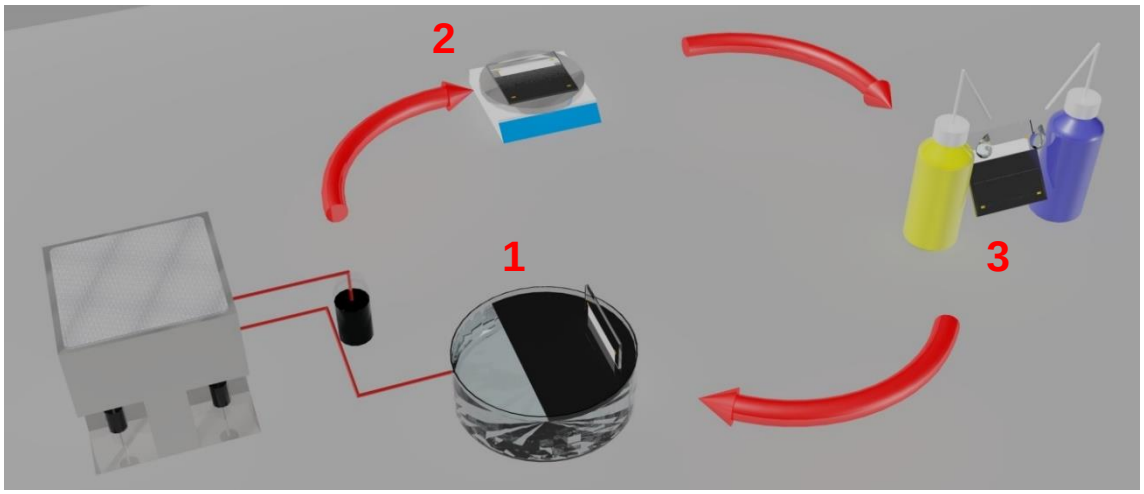

Figure 23 – Schematic illustration of the layer-by-layer carbon coating process with automatic injection: (1) LB carbon film assembling, (2) drying step and (3) wetting/washing of carbon coated separator.

3. Storage of carbon coated separator

After the desirable number of carbon coatings is achieved, it is necessary to store the coated separator. Place the finished substrate on a flat surface and with the tweezers de-attach the separator from the glass plate (Figure 25). Then, with a scissor cut the parts with the tape and transfer the carbon coated separator into a plastic bag using a tweezer. Write on the plastic bag the carbon used to coat, the number of layers and the date which the separator was coated (Figure 26).

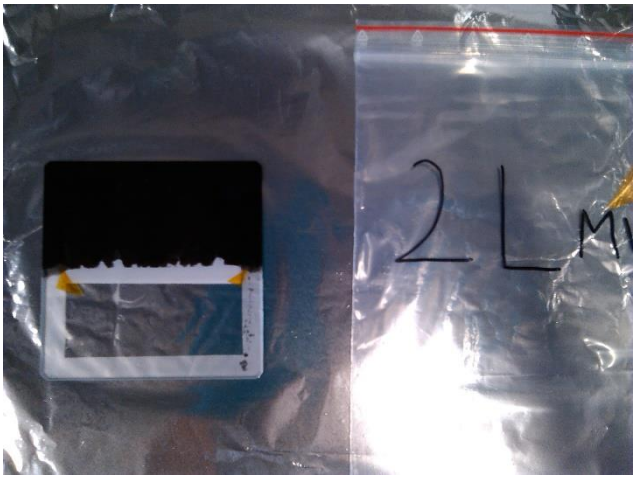

Figure 24 – Finished carbon coated separator with 2 layers.

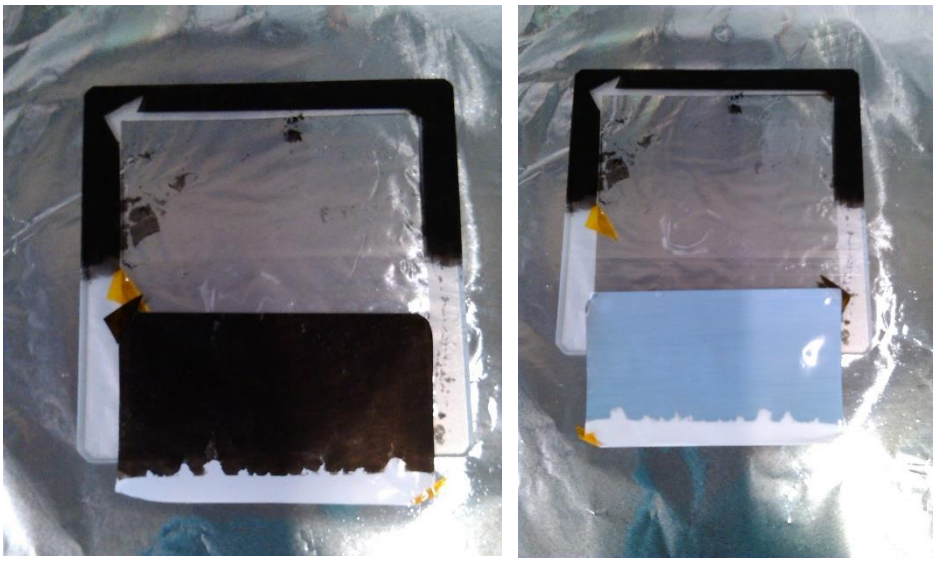

Figure 25 – De-attaching the separator from the glass plate.

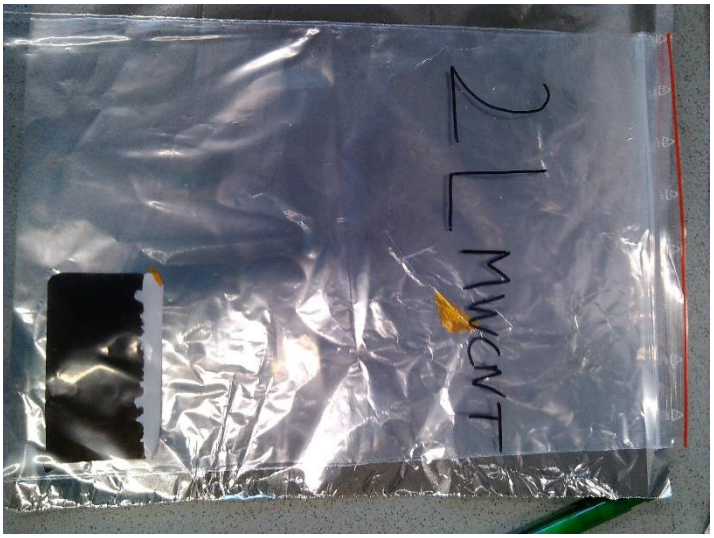

Figure 26 – Stored 2 layer carbon-coated separator.

After finishing, wash and clean all the materials and equipment. Paper towel used in the course of the coatings must be stored in a specific plastic bag. The flasks which contained the suspensions should be washed with ethanol, and the resulting mixture poured in a design bottle.

References

[1] M. S. Kim, L. Ma, S. Choudhury, S. S. Moganty, S. Wei e L. A. Archer, "Fabricating multifunctional nanoparticle membranes by a fast layer-by-layer Langmuir–Blodgett process: application in lithium–sulfur batteries," *Journal of Materials Chemistry A,* pp. 14709-14719, 2016.

Appendixes

Table 2 – Mass of carbon nanoparticles, in mg, necessary to produce a suspension with a carbon content of 0.1 and 0.35 wt. %.

	Carbon nanoparticle wt. %	
Volume of pure ethanol / ml	0.1	0.35
10	7.898	27.712
15	11.847	41.568
20	15.796	55.424
25	19.745	69.280
30	23.694	83.136
50	30.489	138.560

List of abbreviations

V_{EtOH}	Volume of pure ethanol in milliliters
V_X	Volume of component X in milliliters
m_C	Mass of carbon nanoparticles in milligrams
m_{EtOH}	Mass of pure ethanol in milligrams
m_X	Mass of the component X in milligrams
m_{sus}	Mass of the suspension in milligrams
m_{tot}	Total mass of the system in milligrams
ρ_{EtOH}	Volumetric density of pure ethanol in milligrams per milliliter
ρ_X	Volumetric density of component X in milligrams per milliliter

$wt_C.\%$	Mass fraction of carbon nanoparticles in percentage
$wt_X.\%$	Mass fraction of component X in percentage

The total mass of the system is given by Eq. (1)

$$m_{tot} = \sum m_X \tag{1}$$

where m_{tot} is the total mass of the system and m_X is the mass of the component X, both in mg.

In order to describe our system, Eq. (1) will be written as

$$m_{sus} = m_{EtOH} + m_C \tag{1.1}$$

with m_{sus} as the mass of the suspension in mg, m_{EtOH} as the mass of pure ethanol in mg and m_C as the mass of carbon nanoparticles in mg.

The volumetric density is given by Eq. (2)

$$\rho_X = \frac{m_X}{V_X} \tag{2}$$

where ρ_X is the volumetric density of the component X in mg mL^{-1}, m_X is the mass of the component X in mg, and V_X is the volume of the component X in mL.

The volumetric density of the pure ethanol can be written as

$$\rho_{EtOH} = \frac{m_{EtOH}}{V_{EtOH}} \tag{2.1}$$

Rewriting Eq. (2.1) in order of m_{EtOH}, it gives

$$m_{EtOH} = V_{EtOH} \cdot \rho_{EtOH} \tag{2.2}$$

The mass fraction is given by Eq. (3)

$$wt_X.\% = \frac{m_X}{m_{tot}} \cdot 100 \tag{3}$$

where $wt_X.\%$ is the mass fraction in percentage, m_X is the mass of the component X in mg and m_{tot} is the total mass of the system.

For the given system, the mass fraction of carbon nanoparticles is

$$wt_C.\% = \frac{m_C}{m_{sus}} \cdot 100 \tag{3.1}$$

where $wt_C.\%$ is the mass fraction of carbon nanoparticles in percentage, m_C is the mass of carbon nanoparticles in mg and m_{sus} is the mass of the suspension.

Rewriting Eq. (3.1) in order of m_{sus}, it gives

$$m_{sus} = \frac{m_C}{wt_C.\%} \cdot 100 \tag{3.2}$$

Rewriting Eq. (1.1) in order of m_{EtOH}, it gives

$$m_{EtOH} = m_{sus} - m_C \tag{1.2}$$

Substituting Eq. (2.2) and Eq. (3.2) in Eq. (1.2), it gives

$$V_{EtOH} \cdot \rho_{EtOH} = \left(\frac{m_C}{wt_C.\%} \cdot 100\right) - m_C \quad (4)$$

Rewriting Eq. (4) in order of m_C, it gives

$$m_C = \frac{V_{EtOH} \cdot \rho_{EtOH} \cdot wt_C.\%}{100 - wt_C.\%} \quad (4.1)$$

Example: You want to produce a LB carbon film of Ketjenblack. To do so, it is necessary to prepare a suspension with a volume of ethanol of 25 ml, with a carbon content of 0.1%.

V_{EtOH} = 25 ml, ρ_{EtOH} = 789 mg ml^{-1}, $wt_C.\%$ = 0.1.

$$m_C = \frac{25 \cdot 789 \cdot 0.1}{100 - 0.1} = 19.745 \text{ mg}$$

K: Detailed experimental protocol for production of solvent-free Li_2S cathodes

Solvent-free Li_2S Cathodes

Brief introduction

Here is presented the method to produce solvent-free Li_2S cathodes. The materials and equipment are listed below.

Section		Material	Equipment
Preparation of the stainless steel template	1.1	Isopropanol Acetone Paper towel	Stainless steel template Spatula
Punching	1.2	Heat-resistant foil Carbon-coated aluminum foil	Cutting table Punching equipment Tweezers
Cathode powders	1.3	Carbon-coated Li_2S (Chemetall Gmbh) Pristine Li_2S (Albermale, 99.9%) Ketjenblack EC-600 JD (Akzonobel) PVP (Sigma-Aldrich) PEO (Sigma-Aldrich)	Glass flask Funnel Tweezers Spatula Paint-brush Mortar and Pestle Aluminum disposable dish
Cathode fabrication	2.1	Punched heat-resistant polymer Punched carbon-coated aluminum Cathode powder	Paint-brush Aluminum disposable dish Stainless steel template
PEEK foil pocket	2.2	PEEK foil Stainless steel template	Vacuum sealer
Thermal hydraulic press	2.3	PEEK pocket (with vacuumed stainless steel template)	Thermal hydraulic press Gloves
Cathode storage	2.4	PEEK pocket (with vacuumed, heat-pressed stainless steel template)	Scissor Tweezers Plastic box

1. Preliminary preparation steps

In the following sections will be described the steps to prepare the stainless steel template, the punching of the heat-resistant polymer and carbon-coated aluminum, and the cathode powders. It is important to always use disposable gloves, safety glasses and a lab coat. Due to the characteristic smell of H_2S, a face mask could also be used, although it is not mandatory. Work always inside the argon filled glove box. Since fine particles easily disperse, try to be as clean as possible while working in the glove box. Get equipment which will be used solely for your experiments, such as the tweezers, the paint-brushes, funnel, spatula and stainless steel template, and always clean the equipment after each experiment.

1.1. Preparation of the stainless steel template

Take the stainless steel template to a sink and open the template. Pour ethanol on the inner part of the template and clean vigorously the corners. If necessary, put paper soaked in isopropanol on the tip of a spatula and scratch on the corners. Then, squirt acetone and let the lower part of the template dry. The same cleaning procedure should be used on the upper part of the template. Afterwards, let the template dry, and then transport it inside the argon filled glove box.

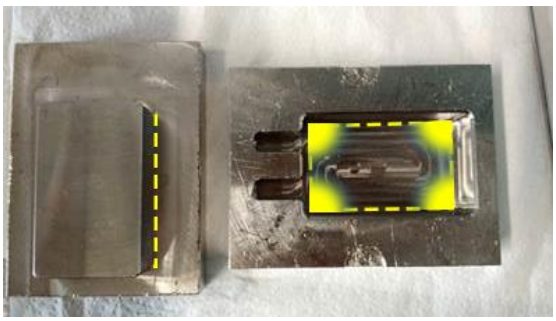

Figure 1 – Stainless steel template. On the left is shown the upper part of the template, and on the right is the lower part. The yellow zones show the difficult areas to clean.

1.2. Punching

Some of the materials used on the cathode assembly come in rolls, such as the carbon-coated aluminum, used as the current collector, and the heat-resistant polymer, to protect against the adhesion of the cathode powder with the walls of the stainless steel template. Thus, it is necessary to use a punching equipment. Unfold the roll and cut a piece of the material with a cutting table. Afterwards, take the sheet and carefully put in the punching equipment, and cut 15-20 current collectors and heat-resistant layers.

Figure 2 - Punching equipment. In yellow is represented the sheet disposition.

Figure 3 - Carbon-coated aluminum, with the carbon-coated side on the left, and the aluminum on the right (left). Layer of heat-resistant polymer (right).

Then, store the punched heat-resistant polymer and current collector layers inside a clean plastic box, and transport inside the argon filled glove box.

1.3. Cathode powders

Start by cleaning a glass flask. Pour ethanol inside the flask, and clean with paper towel. Afterwards, transport the glass flask into an oven and let it dry. Then, take the glass flask inside the argon filled glove box. A total of 1 g of cathode powder is produced. The weight percentage is 60% of active material, 30% of carbon additive and 10% of binder. Measure 0.6 g of Li_2S or carbon-coated Li_2S powders, 0.3 g of Ketjenblack and 0.1 g of binder, PEO or PVP, depending on the formulation adopted. Put the different powders inside a mortar and with a pestle start mixing and grinding. When the mixture is homogeneous, put a funnel inside the glass flask and carefully pour the cathode powder. If any powder remains on the funnel, use a paint-brush to transfer the particles inside the flask.

Table 1 – Composition of a mixture used in the production of a solvent-free Li_2S cathode.

	Material	wt. %
Active material	Pristine Li_2S/Carbon-coated Li_2S	60
Carbon additive	Ketjenblack EC-600 JD	30
Binder	PVP/PEO	10

2. Solvent-free Li_2S cathode production

The following sections describe how to produce a solvent-free cathode, through the deposition of a cathode powder in a template, followed by vacuum sealing of the template with PEEK foil and finally the heat-pressing of the template in a thermal hydraulic press.

2.1. Cathode fabrication

With a tweezer, put a punched heat-resistant polymer layer inside the template. Then, measure 150 mg of the cathode powder, in an aluminum disposable dish, and pour inside the template. With a paint-brush, transport the remaining cathode powder from the aluminum disposable dish, inside the template. With a spatula, disperse the powder, and then take a distribution tool and spread the cathode powder homogenously on the surface of the heat-resistant polymer layer. When it is smoothly distributed, place the punched carbon-coated aluminum on top of the cathode layer, with the carbon side facing the cathode powder. Then, slowly place the contact blocks inside the template and close it. The last two steps require precision and carefulness, otherwise the fine particles of the cathode powder would disperse all over the template, thus it would be necessary to repeat the cathode fabrication.

Figure 4 - Distribution tool (left) and contact blocks (right).

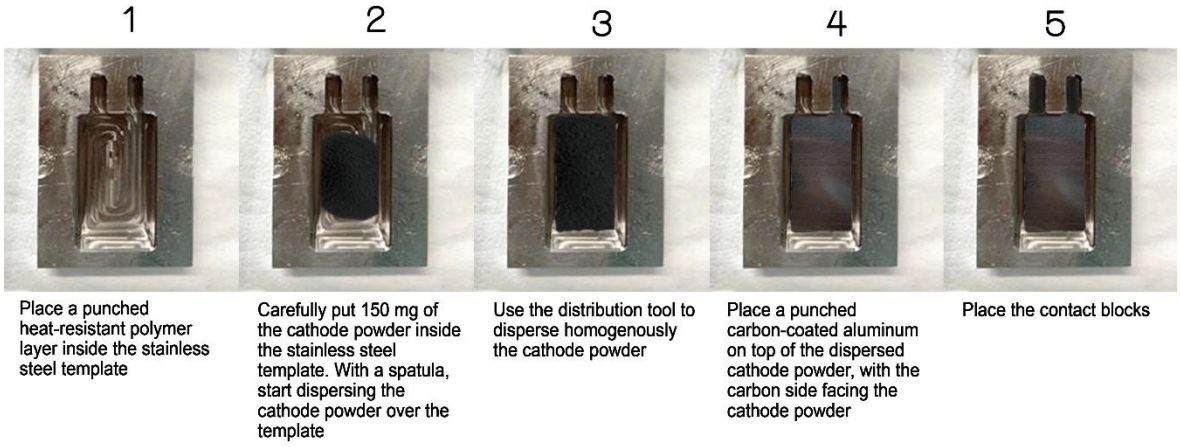

Figure 5 – Cathode fabrication procedure.

2.2. PEEK foil pocket

In a vacuum sealer place a PEEK foil, the and on top put the closed stainless steel template. Pre-define the sealing temperature and time to 70°C and 90 seconds, respectively. Place on top of the template another foil of PEEK and close the vacuum sealer. When the sealing is done, take the PEEK foil pocket and investigate if it is vacuumed. If the pocket is not fully sealed, change the sealing temperature and time, or include more layers of PEEK foil. It is important that no air gets inside the pocket, or else the Li_2S present in the cathode will react with the water and oxygen. When this step is finished, take the sealed template from the argon filled glove box.

2.3. Thermal hydraulic press

Place the sealed template in a thermal hydraulic press and make the plates of the press contact the surface of the template. Select a temperature of 155 °C, and let the template heat up for 15 minutes. Afterwards, stablish a pressure of 2 kbar, and wait another 15 minutes. When this procedure is finished, take the sealed template and let it cool down. Then, transfer the sealed template inside the argon filled glove box.

2.4. Cathode storage

Cut the PEEK pocket and take the template outside. Open the template, take the contact blocks and retrieve the prepared cathode. Store the cathode inside a plastic box, write the cathode formulation, and the date when was produced.

3. Cleaning

Repeat the procedure in 1.1.